2 Input/Output Microfibres SNAP Experiment — Fabrication and Characterization

SHEN LI
Master of Science (by Research)

SNAP Photonics Group
Aston Institute of Photonic Technologies
Aston University
September 2018

Contents

Abstract

This work described the application of two microfibers for the first time to experimentally investigate tunneling phenomena in SNAP.

The axial WGM distribution along a SNAP fiber is governed by 1D time-independent Schrödinger equation. The transmission spectrum of microfiber orthogonally coupled with SNAP fiber were measured with $1\mu m$ incremental step microfiber scanning along SNAP fiber.

The microfibers were fabricated with sapphire tube and CO_2 laser heat-and-pull setup. Uniform SNAP fibers prepared with hot sulphuric/nitric acid stripping shows the general trend of exponential decay. However, the problem of deep cracks prevented the accurate determination of tunneling time. Symmetric SNAP double resonators with nano-engineered radius variations along uniform SNAP fibers were fabricated using CO_2 laser annealing technique. The observed energy level splitting due to the effect of resonant tunnelling between equal energy levels demonstrates the ultra-precise-tuning of height, shape and separation of the double resonators.

The transmission surface plots for both S_{11} and S_{12} closely matches the theoretical SNAP model based on Levenberg-Marquardt least squares fitting algorithm and bare Green's function construction method.

The reviewed tunneling time literature is intended as a self-contained framework for further SNAP tunneling time research.

Keywords: Microfiber, Coupling, WGM, SNAP, Annealing, Schrodinger equation, Tunnelling time.

Acknowledgement

Words of thanks

With the submission of my masters dissertation, I would like to express my sincere gratitude:

In the course of my dissertation design, I received careful guidance from Prof. Misha Sumetsky in all aspects of my dissertation, from topic selection, conception, structure to finalization, which enabled me to be proud of the final design and writing of my graduation dissertation. I'm very fortunate to be an internationally renowned academic authority, Prof. Misha's student. My supervior, Professor Misha possess many outstanding qualities, such as rigorous in academic research, profound in knowledge, keen in academic thinking, diligent in paying attention to efficiency. Under his excellent guidance and supervision, I mastered a relatively solid foundation in systematic theory and specialised knowledge; obtained the scientific research ability to undertake preliminary research work and practical skills to independently conduct research experiment. Prof. Misha will be my lifelong mentor and model to whom I am eternally grateful!

My dissertation was written, from beginning to end, under the guidance of my teacher, Dr. Yang Yong. Dr. Yang had been assiduous in passing on his personal experience and skills in thesis writing; he took a great deal of effort in helping me to collect references and choosing writing materials; in particular, Dr. Yang put in a lot of valuable time and energy to supervise me on carrying out theoretical analysis and mathematical reasoning on my experimental results, which enabled my writing process to go smoothly. Dr. Yang's noble teaching ethic, personal excellence, meticulous academic attitude, strict discipline and approachable personality deeply touched me. I would like to express my heartfelt gratitude to Dr. Yang!

Special thanks to Dr. Nikita Toropov for selflessly teaching me his knowledge and expertise on the fabrication of "SNAP resonators" , which I benefited greatly and obtained a lot of inspiration.

Thanks to Gabriella Gardosi and Sajid Zaki, I will not forget their warm-hearted help during my writing process!

And finally thanks to all members of SNAP team for the kind help and continued support!

Acronyms

CL	—	CO_2 Laser
CSS	—	CO_2 Laser and sapphire tube setup
FSR	—	Free Spectrum Range
FWHM	—	Full width at half maximum
IL	—	Insertion loss
LHS	—	Left-hand-side
MF	—	Micro-fibre
MNF	—	Micro/Nano-fibre
OFR	—	Optical Frequency Range
RHS	—	Right-hand-side
SF	—	SNAP fibre
SNAP	—	Surface Nano-scale Axial Photonics
ST	—	Sapphire tube
USF	—	Uniform SNAP fibre
WG	—	Waveguide
WGM	—	Whispering Gallery Mode

Symbols

λ	—	Wavelength
λ_{res}	—	Resonance wavelength
G	—	Bare Green's Function
$\overline{G}$	—	Renormalized Green's Function

List of Figures

List of Tables

Chapter 1

Introduction

1.1 Background

Previous research and development of photonic integrated circuits in the last 20 years have been devoted to the establishment of a platform with microscopic size, wide-applicability and control needed to facilitate scientific breakthroughs in photonics research. [114, 103, 63, 4] The platform must provide a technological system to manipulate, guide and store light. It is difficult to build a high quality factor trap for photons; the microscopic version of conventional optical resonators cannot be built simply because natural reflective materials such as metals are highly absorbable. Similarly, a simple analogy between electrons and quantum mechanics cannot be used to construct a photon quantum well. In fact, this will would total internal reflection of light at the boundary around the trap, which is a significant challenge. [62] The Surface Nanoscale Axial Photonics (SNAP) is an highly precise and sensitive photonic platform that resolves this challenge and in particular SNAP technological system plays an important role in the simulation and study of various quantum mechanical phenomena.

1.1.1 Introduction to SNAP

SNAP Device Definition

A basic SNAP device is composed of a special optical fiber called SNAP fiber (SF) with nanoscale radius variations along it and a transverse input/output waveguide coupled to the SF. The input/output waveguide made from tapered optical fibers with a micrometer waist diameter is often referred as microfiber (MF). SNAP makes use of whispering gallery modes (WGMs) that circulates near the SF surface and propagates slowly along the SF axis. WGM is typically excited by input microfiber.[89]

Whispering Gallery Mode

In the famous whispering gallery at St Paul's Cathedral in London, two people speak sideways to the wall could very clearly hear each other from a large distance away. In the $19th$ century, Lord Rayleigh first carried out a systematic research of this interesting phenomenon.

Figure 1.1: From the Whispering Gallery

The principle is that sound waves can propagate with little loss along the smooth and curved inner-wall-surface by constant grazing-angle reflections, thus it can be sustained over a long distance along the wall. This phenomenon is called Whispering Gallery Mode (WGM).

Similar to the reflection of sound waves by the wall, when light is incident from dense to sparse medium and the incident angle is larger than critical angle, the total internal reflection can also occur at the media interface. Thus there exist optical WGM at the curved interface of high-refractive-index medium. Within the boundary of the closed cavity, the light can always be trapped in the cavity to maintain a stable travelling wave transmission mode.

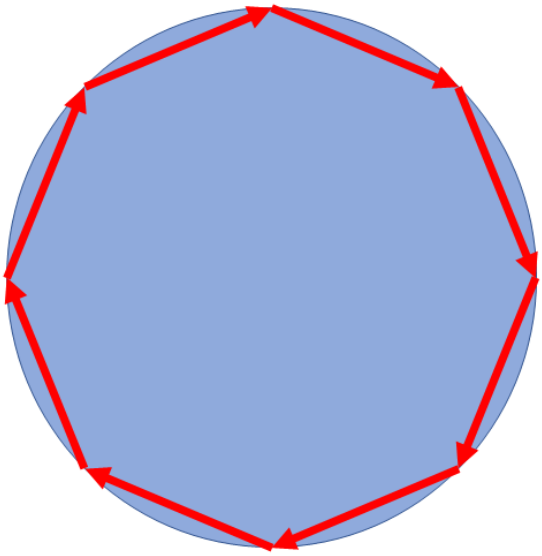

Figure 1.2: WGM inside a SNAP cavity sustained by total internal reflection

Representation of WGMs

Fig. 1.2 shows the geometric representation of WGM within a rotationally symmetric cavity sustained by total internal reflection. Explanations of WGMs from the viewpoint of geometric ray optics can help to understand the underlining principle of mode generation mechanism in general resonators: rays being continuously reflected by the curved side wall of the cavity at near-grazing angles It then completes a full round trip along the inner cavity surface and returns to its starting point in phase with the incident coherent source.

Fig. 1.3 shows 4 general eigenmode profiles representation of a SNAP fiber cross-section, which is a circular resonating cavity with in this example, azimuthal modes number, $m = 15$. The first profile from the left is commonly refereed as the fundamental or first order mode, it corresponds radial mode number, $p = 1$. The next 3 eigenmode profiles have $p = 2,3,4$ respective are called higher order modes.

Figure 1.3: Illustration taken from Gomilšek [31]: Whispering gallery modes inside cylindrical cavity

One of the main characteristics of WGMs is highly localized mode volume, V near the edge of the resonator. The localization of the mode increases with increasing m. More localized modes also have lower loss (higher Q factor). Higher order modes with $m \gg 1, p > 1$ have a less confined mode volume closer towards the center of the cavity.

Early Development of WGM micro-cavities

SNAP fiber is a type of cylindrical WGM micro-cavity. In this subsection, literatures from the 19th century on the early developmental history of WGM cavities has been summarised and shown on a time-line in order to establish a clear developmental perspective:

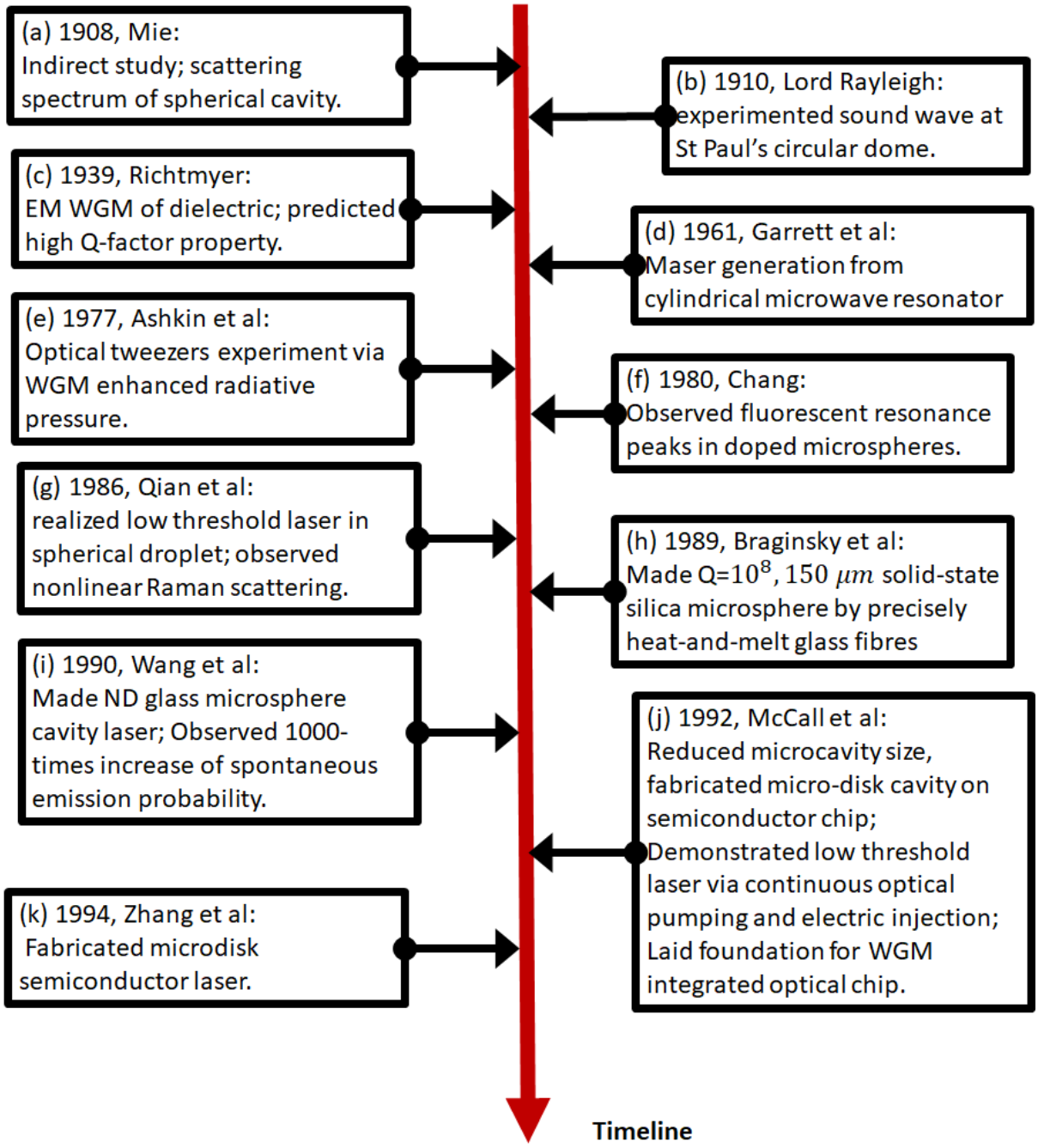

Figure 1.4: Early Development of WGM micro-cavities [55, 76, 79, 28, 3, 7, 73, 15, 53]

Attributes of SNAP Technological System

SNAP technology displays a number of advantageous attributes: [94]

- Due to the drawing process and high refractive index contrast of optical fiber, the main advantage of SNAP is low surface roughness and low optical loss;
- Periodic light and slow light, without periodic index modulation (e.g. photonic crystals): Periodicity is introduced automatically by each rotation trip around the surface of SF. The main feature of slow WGMs is azimuthal propagation, axial propagation naturally has the characteristics of slow light;
- SNAP is described by one-dimensional Schrödinger equation: the axial propagation of slow WGMs can be used to study quantum phenomena such as the localisation and tunneling of light for various barrier potentials;
- Precisely engineer the of the nanoscale variation of the effective fiber radius to accurately control WGM light;
- Surface WGMS is completely stopped under the action of point light source;
- Microscale dimensions: Since the characteristic axial wavelength of slow WGMs have large axial wavelength ($\approx 10\mu m$), the fabrication difficulty of SNAP devices is greatly simplified as a result. Instead of increasing the diameter in the case of low contrast photonic circuits, the microscale dimension is retained by only increasing the size of SF along its fiber axis.

The SNAP technology can be used to fabricate optical resonating cavities that store light in the from of WGMs. Due to the excellent frequency selectivity, SNAP cavities can be used as optical filters, delay lines and modulators. In addition, the ability to limit light energy to a small mode volume greatly enhances the interaction between light and matter and can lead to strong non-linear effects and optomechanical effects.

1.1.2 Microfibers

Application and Laser Fabrication of Microfibers

In the 21st century, with the development of optical fiber communication in the direction of ultra-high speed, super-capacity and super-long distance, as well as the development of device design theory and fabrication technology, the requirements for the performance and integration of devices have been improved. The miniaturization of devices has become one of the important trends in the research and application of science and technology. Among them, the micro/nano optical waveguide is an important foundation for studying the phenomenon of micro-nano photonics and constructing micro-nano photonic devices, and it is one of the hotspots in the field of nano-photonics. Compared with other kinds of micro/nano optical waveguides (such as silicon-based planar waveguides, metal surface plasma waveguides), micro/nano-wires have extremely low coupling losses, extremely low roughness, and is able highly confined light fields due to its high refractive index contrast, large evanescent field coupling efficiency, light mass and so on. These properties make micro-nano fiber have many potential applications in fiber optics, near-field optics, non-linear optics and quantum optics, as well as micro/nano-scale optical transmission, coupling, modulation, resonance amplification and sensing.

The laser fabrication for microfibers is a time consuming process takes about 3 hours to achieve, it requires a lot of practical experience to do well; the main difficulty posed is that microfibers have a very thin diameter thus very easily broken, further precise alignment of synchronous translation stages by cameras is not easily achieved. I spent a significant amount of time improving the success rate and

efficiency of taper-drawing and experimental storage system; fabricated 100s of microfibers; success rate is improved from about 20% to over 80%. In particular, a paper on a specific application of microfibers, Martinez et al. [50], is published during my involvement of another research project.

Evanescent field coupling with microfibers

Evanescent field, also called evanescent wave, is usually a kind of electromagnetic wave, it is produced on the boundary surface of two different media due to total reflection. In some sense evanescent wave is a kind of surface wave: its amplitude attenuates exponentially with increased separation perpendicular to surface boundary while its phase changes along the tangential direction. Evanescent waves are extensively used in the field of photonics. For example, detection of the degree of amplitude decay using the principle of frustrated total internal reflection, can determine the average distance between two surfaces. This is particularly the case in contactless coupling, changing the MF/SF air gap distance, can change the strength of light coupling. When MF have a micron scale waist, evanescent field attenuates over a larger region and thus is able to penetrates deeper into the SF. However, the analysis frequency spectrum in this case would become more complex due to the presence higher order modes.

1.2 Organisation of the Dissertation

The content organisation of this work is outlines in Table 1.1. The dissertation is organised into six chapters. The second chapter introduces how to make SNAP devices. In chapter three describes the theory and fabrication of microfibers. The next two chapters report how to measure the transmission spectrum of single/double well SNAPs with single/double input/output tapered microfiber configuration. Through numerical method, the experimental data is fitted against theoretical SNAP results. In particular, two microfiber scan is used for the first time to measure tunneling in photonics. The last chapter summarises the results obtained from the previous chapters and furthermore discussed the possibility of studying photonic tunnelling in uniform SF with two microfibers and gives preliminary experimental results.

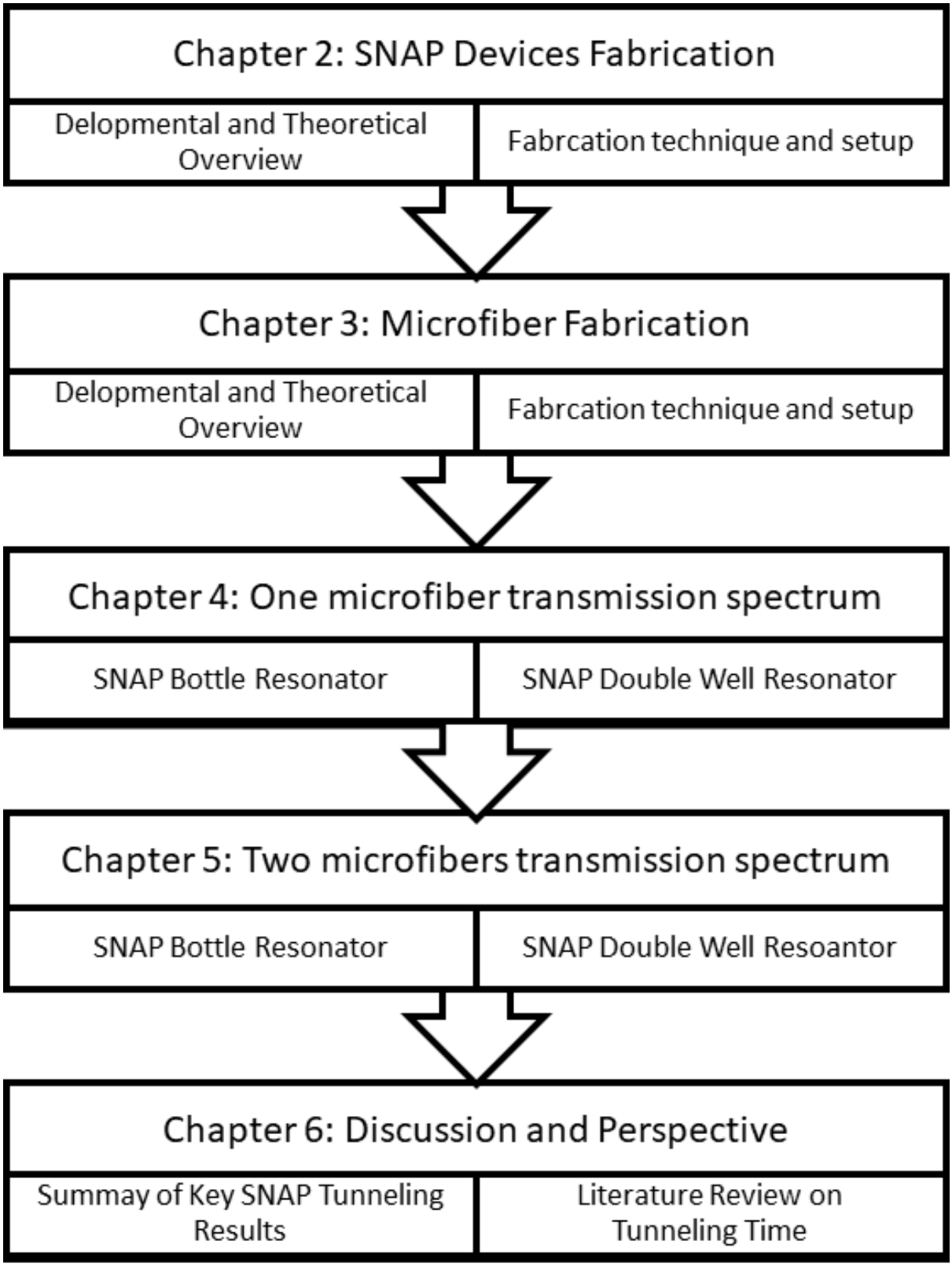

Table 1.1: Content Organisation

Chapter 2

Concept of SNAP and Fabrication Method

2.1 Fundamentals of SNAP Technology

2.1.1 Basic building blocks of SNAP device

SNAP device consists of the following three fundamental components:

a) **WGM Bottle Microresonator**: this corresponds to a 'quasi-quantum-well' and the results in a series of discrete wavelength states between two turning points (corresponding to resonances in the transmitted amplitude). The resonant transmission amplitude is related to the MF position. In particular, if the MF is placed on a node of the WGM, the SF/MF coupling disappears.

b) **Concave Fiber Waist**: in this case, the wavelength below the barrier region is governed by exponential attenuation of amplitude away from the MF position. Or otherwise, above the barrier region, the excited WGM is delocalized. In particular, the semi-classical theory is used to give a simple explanation for the localization of light in a uniform cylindrical microresonator;

c) **Monotonously Increasing Diameter**: WGMs excited by the MF coupled near a turning point along one direction interferes with the waves emitted along the opposite direction and reflected at the turning point. When the waves interference conditions are satisfied, the distribution of light can exhibit localization of states and halting of light.

Fig. 2.1 illustrates the basic elements of a SNAP device:

These basic components can be coupled together to create a series of dense integrated photonic devices. They can also be coupled to one or more transverse MFs to manipulate multiple inputs and outputs. SNAP technological system enables the precise design of such integrated devices to control the field distribution, transmission spectrum, group delay and dispersion transmitted through MFs.

Figure 2.1: SNAP device basic elements [94]

2.1.2 Typical sizes of SNAP Devices

In the following paragraph, the sizes of microfiber and SNAP fiber fabricated during the experiments is specified respectively. In particular, depending on control of annealing laser beam, the variations of SNAP fiber surface along the axial and radial directions can be precisely engineered.

Microfiber

- Original diameter: $125\mu m$
- Waist diameter: $\approx 1\mu m$
- Waist length: $\approx 30mm$
- Taper transition length: $\approx 15mm$

SNAP fiber

- Diameter: $30 \longrightarrow 50\mu m$
- Variations along axial direction parallel to SNAP fiber surface: $\approx 200\mu m$
- Variations in radial direction perpendicular to SNAP fiber surface: $\approx 3nm$

2.1.3 Basic SNAP Resonator

The most basic SNAP resonator consists of a cylindrical cavity with uniform cross-section along its axial direction.

Fig 2.2 shows SNAP resonator in cylindrical coordinates (z, ρ, ϕ):

The modes for an SNAP resonator must satisfy the phase condition in order to be sustained : i.e. the total phase change must be an integer multiple of 2π after a complete resonator round trip. Thus SNAP resonant modes can only exist on the specific resonant frequencies.

SNAP cavity modes can be labelled by using three indices:

- Axial mode number, l: governs the mode distribution along the z-axis;
- Azimuthal mode number, m: mode rotational symmetry;
- And, radial number, p: the radial profile.

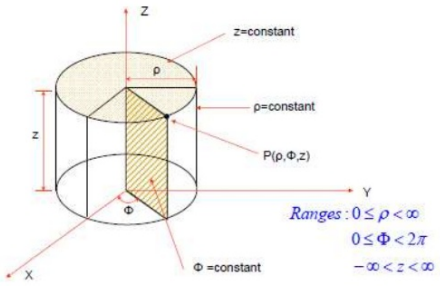

Figure 2.2: Cylindrical Coordinate System

2.2 SNAP device Theory

Fig. 2.3 shows an example of the first order WGM distribution for a SNAP fiber cross-section in this case $m = 12,\ p = 1$. For the purpose of modelling SNAP devices and analysing data obtained from SNAP experiments, the 'SNAP device theory' which is used to describe the distribution and transmission of WGMs along SNAP cavities with simple geometries have been developed. [94]

It was derived from SNAP theory the difficult problem of inter-modal coupling and inter-modal transition is absent for a SNAP fiber, this is because: firstly it has an ultra-smooth, high quality factor surface resulted from the fiber drawing process; and second SNAP resonators is able to fully confine light in the case of nano-scale diameter variations, thus the effective radius change, Δr and refractive index change, $\Delta\lambda$ introduced by CO_2 laser or UV exposure on the surface of SNAP fiber needs only to be tiny and continuous.

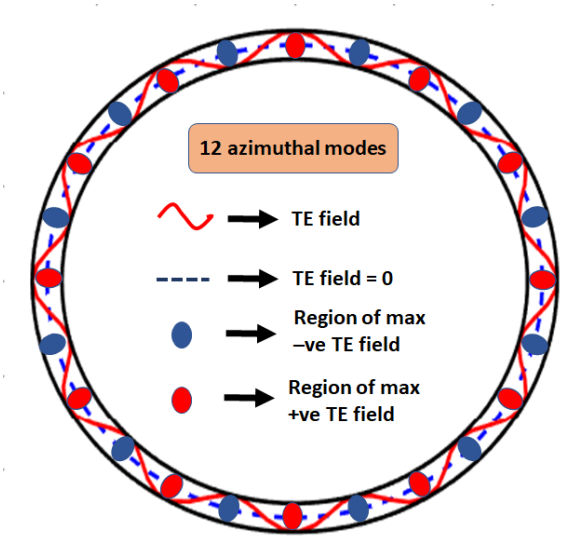

Figure 2.3: Azimuthal modes

As a consequence, in the vicinity of WGMs resonance wavelength, λ_{res}, the distribution of WGMs field along a SNAP fiber corresponds to adiabatic and continuous boundary conditions and its maths expression becomes decoupled into a product of radial, axial and azimuthal components, thus without the microfiber the fields distribution can be written as:

$$U_{m,p,q}(\mathbf{r}) = \Psi_{m,p,q}(z) \cdot R_{m,p}(\rho) \cdot e^{im\phi} \tag{2.1}$$

The equation above is in cylindrical coordinates, (z, ρ, ϕ). q, p, m are the mode numbers for the axial, radial and azimuthal directions respectively.

As shown in figure 2.8, when microfiber touches SNAP fiber at right angles, the guided evanescent mode surrounding the microfiber is coupled into the whispering gallery modes of SNAP fiber.

Microfiber is used as a waveguide to launch light into SNAP fiber as well as a sensor to measure the insertion loss transmission for broadband light. A microfiber with small optical loss and straight-line transmission spectrum is a good indication of its adiabatic taper transition and surface smoothness. Uniform SNAP fiber is a kind of cylindrical WGM resonator. It has an ultra smooth surface and a quality factor of $\approx 10^6$ because it is made from drawn silica.

The uniform SNAP fiber is the most basic optical component in SNAP. Small radius variations can be introduced along a uniform SNAP fiber by CO_2 laser annealing method.

The small perturbation along the radial and axial direction changes the propagation constant β according to the equation:

$$\beta^2 = 2\left(\frac{2\pi n_f}{\lambda_{res}}\right)^2 \left[\frac{\triangle r}{\lambda_{res}} + \frac{\triangle n_f}{n_{f0}} - \frac{\triangle \lambda}{\lambda_{res}}\right] \tag{2.2}$$

Substituting the propagation constant into the approximation of resonant wavelength by semi-classical approximation:

$$\lambda_{mp}^{(0),\pm} \approx \lambda_m^{(0),\pm}\left[1 + \frac{\zeta_p}{2^{1/3}m^{2/3}} + \frac{n_0}{m(n_f^2 - n_0^2)^{1/2}} \cdot \left(\frac{n_f}{n_0}\right)^{\pm 1}\right]$$

Yields the time-independent one-dimensional Schrödinger equation can be expressed as:

$$\frac{d^2\Psi}{dz^2} + \beta^2\Psi = 0, \quad \beta^2(\lambda, z) = E(\lambda) - V(z) \tag{2.3}$$

It is shown from theory that the stationary one-dimensional Schrödinger equation is the fundamental equation which characterises the axial distribution of WGMs excited via a microfiber along a cylindrical SNAP fiber.

The effective radius variation of a SNAP fiber, $\Delta r_{eff}(z)$ depends on physical radius variation, $\Delta r = r(z) - r_0$ and refractive index variation, $\Delta n_f(z) = n_f(z) - n_{f_0}$, it is expressed as:

$$\Delta r_{eff}(z) = \Delta r(z) + r_0 \cdot \frac{\Delta n_f(z)}{n_{f_0}} \tag{2.4}$$

The propagation constant in the direction tangential to the circumference of SNAP fiber cross-section is $k(\lambda_{res}) = \frac{2\pi n_{f_0}}{\lambda_{res}}$.

The energy of coupled light depends on the wavelength, in quantum tunnelling it corresponds to the energy of the tunnelling particle:

$$E(\lambda) = -2k^2(\lambda_{res})\frac{\lambda - \lambda_{res} - i\gamma_{res}}{\lambda_{res}} \tag{2.5}$$

The potential $V(z)$ depends on the effective radius variation, in quantum tunnelling it corresponds to the height of barrier potential. SNAP theory make use of the principle that extremely small variations of SNAP fiber radius, $\Delta r(z)$, and refractive index, $\Delta n_f(z)$, near the resonance wavelength, λ_{res} is enough to strongly confine and guide light in the form of WGMs. In SNAP, variations in $\Delta r(z)$ and $\Delta n_f(z)$ is so small and smooth that the coupled wave equations become decoupled and the dependence of the WGM field on the axial coordinate, A(z), is defined by a single differential equation.

2.3 Setup and Fabrication

2.3.1 Main techniques in SNAP fabrication

This section examines the literature regarding the two main techniques of SNAP fabrication: acid-striping and CO_2 laser annealing.

Acid Stripping

In SNAP experiments, it is generally required to first remove the polymer coating around bare optical fibre. [51, 101, 35] The "extraordinary surface smoothness of drawn silica" [96] renders it a good candidate material for making SNAP samples.

Comparison between stripping methods In order to obtain satisfactory SNAP samples, it is most important to achieve the result of smooth fiber surface and uniform diameter. Arguably the most comprehensive study of fibre stripping method of this technique has been provided in the work of Matthewson et al. [51].

Matthewson et al. [51] described the problem with two stripping techniques: i.e. mechanical strippers technique might lead to mechanical damage of fibre surface and solvent swelling technique may leave difficult to remove residues. These two problems would have detrimental effect on SNAP fiber quality because SNAP micro-devices have a high requirement for surface smoothness: i.e. the behaviour of

WGM light is confined by radius variation of $\sim 1pm$;[97] furthermore the degree of surface smoothness plays an important role in reducing attenuation of light propagation along optical fibre surface. [94]

Stripping by hot, concentrated sulphuric acid is the commonly preferred technique in the fabrication of uniform SNAP fiberToropov and Sumetsky [101], Hamidfar et al. [35] because it is able remove the coating without degrading the fibre strength or leaving surface residues. [51]

Fiber Surface Damage It is possible to avoid the surface damage caused by the stripping process through careful operation, post-selection and processing. However, according to Matthewson et al. [51], there is a kind of unavoidable damage which happens naturally due to prolonged ageing and attack from environmental moisture that lead to surface roughing, micro-cracks and strength degradation; moreover the hermetic polymer coating cannot prevent the diffusion of moisture. Thus SNAP fibre should be stored in a moisture-free environment and its reliability should be constantly monitored.

CO_2 laser annealing

CO_2 laser annealing is the main technique for making SNAP micro-cavities, its underlining principle is "local saturation of tension caused by relaxation of the frozen-in tension introduced by the pulling force in fibre drawing process"[96, 97].

Frozen-in tension

Laser annealing is resulted from the release of frozen-in tension. Some SNAP samples are usable for making micro-resonators due to a lack of frozen-in tension; tests by Matthewson et al. [51] have demonstrated that "that stripping the acrylate polymer coating from a fused silica optical fibre by briefly dipping in $200^{\circ}C$ concentrated sulphuric acid does not degrade fibre strength", which implies that hot acid stripping procedure most probably have no reduction effect on the original frozen-in tension, therefore the lack of frozen-in tension leakage is most likely caused by quality degradation of original fibre material due to moisture, unintentional damage or prolonged ageing.

2.3.2 Fabrication Procedure

Fabrication of Uniform SNAP

Fig. 2.4 shows the fabrication process for making uniform SNAP sample. There are two main procedures involved, namely acid stripping and sample making.

Acid Stripping Procedure

The acid stripping procedure involves the removal of polymer coating to obtain the $39\mu m$ diameter single mode uniform fiber, called the SNAP fiber. The following should be noted for this step:

1. The preliminary preparation of acid solution is completed inside a fume cupboard; measure and pour $150ml$ of 95% sulphuric acid solution, followed by 50ml of 68% nitric acid solution into a $250ml$ glass beaker with a magnetic stir bar inside. The beaker is placed on top of a magnetic hotplate stirrer with the hotplate temperature set to $\approx 200\,^{\circ}$C. The beaker is covered with a glass lid to encourage heat convection. Sufficient time was given for the hot acid solution to reach its final temperature, which in this case is $\approx 190\,^{\circ}$C and the waiting time is about 2 hours;

2. A ≈ 20 *cm* section of unstripped SNAP fiber cut from the fiber spool is bend into a "U" shape and fixed with Epoxy onto a support structure at two positions. The width and fixing positions must be carefully adjusted so that the radius of curvature at the bend is large while not touching the side of beaker and air current inside fume chamber should not cause excessive fiber movement; a large radius of curvature ensures minimum bending tension along the fiber;
3. The support structure is positioned with clamps and retort stand so that the bottom part ≈ 8 *cm* of the "U" shaped fiber is immersed inside the hot acid solution for 15 seconds;
4. The rinsing step removes any acid molecules attached to the SNAP fiber. The fiber is dipped for 10 seconds each inside water and acetone. The rinsing is accompanied with small undulating up-and-down hand movement;
5. The SNAP fiber is sealed inside a air-tight clean container immediately after the rinsing step in order to minimise dust contamination.

Sample making procedure

The sample making procedure involves the transfer and attachment of the acid stripped SNAP fiber onto a sample holder for the purpose of convenient measurement and storage. The following points should be noted during this step:

- The entire procedure is performed in a controlled environment inside a experiment chamber, free of dust particles and air current;
- The SNAP fiber is usually not straight when hanging by its own weight; thus it is necessary to attach a light mass such as a small ball of rolled-up sticky tape at the bottom end to straighten up the fiber;
- The orientation of the clamped sample holder was checked with a spirit level to ensure two grooves are aligned vertically;
- Once the SNAP fiber is carefully positioned, the application of epoxy is achieved by gently "brush" with the tip of a small wooden stick.

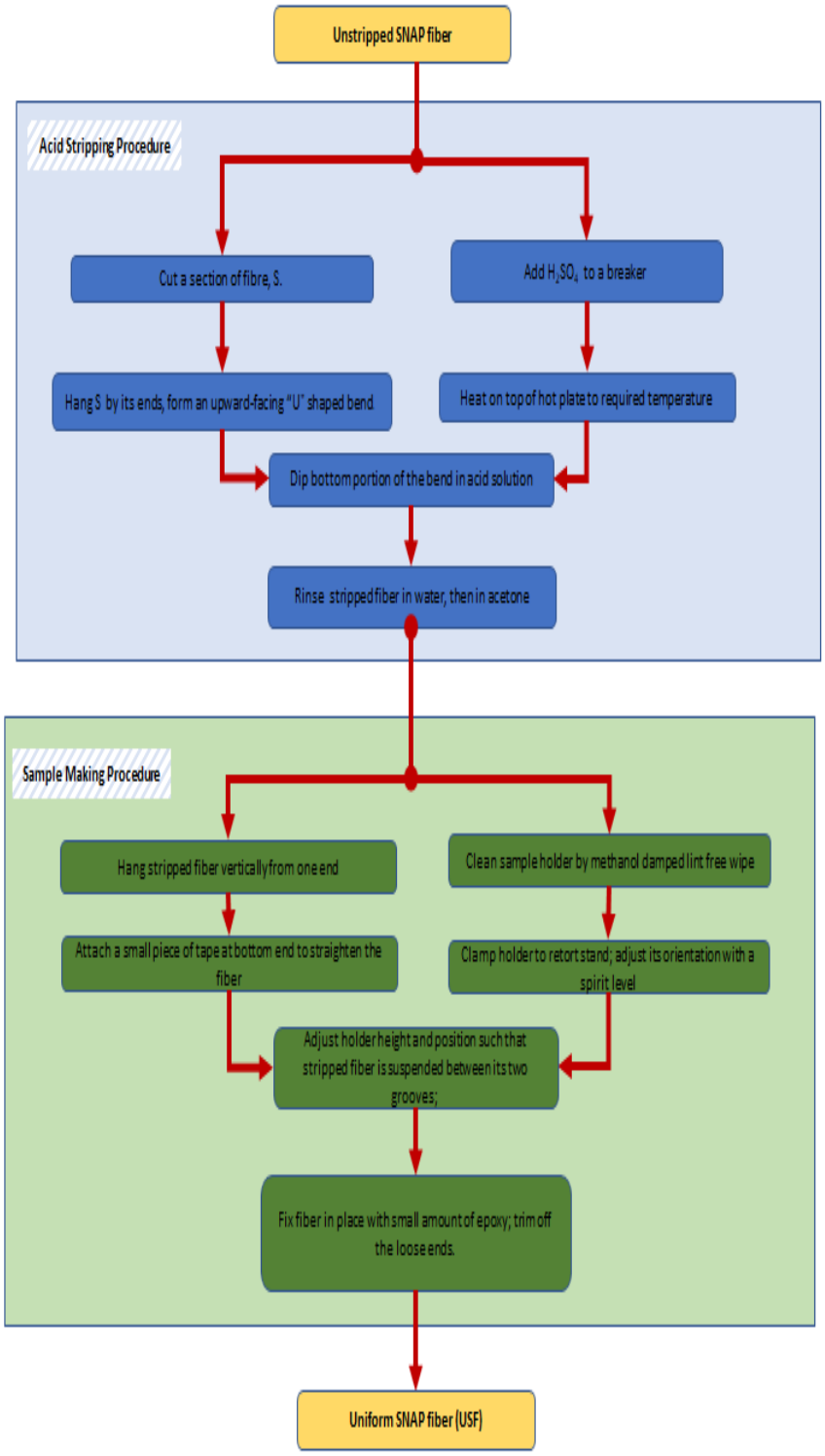

Figure 2.4: Flow Chart of Uniform SNAP Fabrication Procedure

Fabrication of SNAP Micro-resonator

The fabrication of SNAP resonator is realised by the CO_2 laser annealing technique. Fig. 2.5 shows the general procedure for fabricating SNAP resonator.

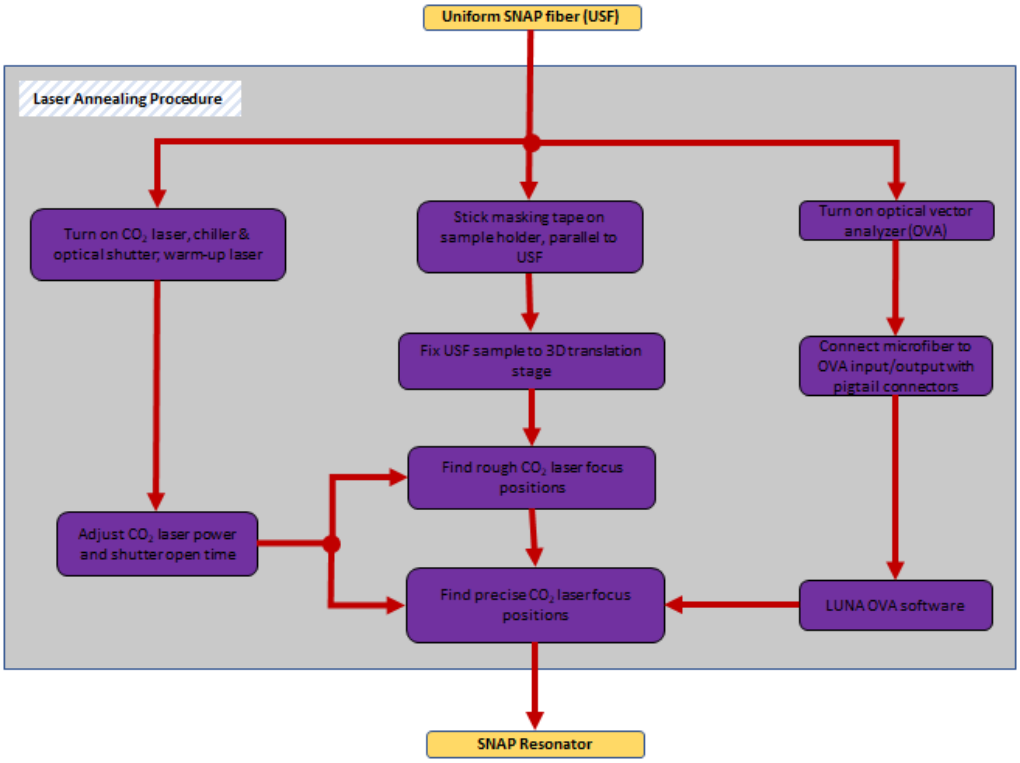

Figure 2.5: Flow chart of fabrication procedure of SNAP resonator

The profile of SNAP resonator resulted from annealing depends on the hot-zone exposed to CO_2 laser beam.

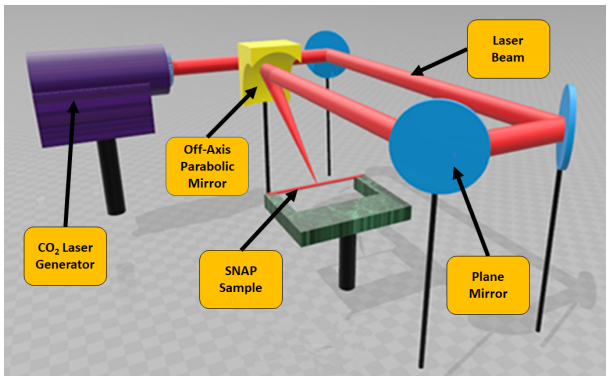

(a) Annealing Rig Illustration

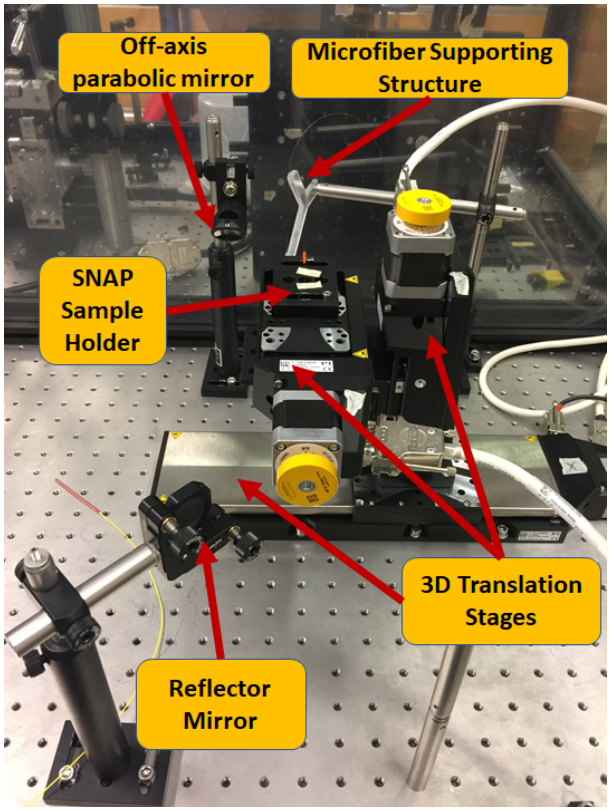

(b) Annealing Rig

As seen in Fig. 2.6a, the beam from CO_2 laser source is first directed by reflector mirrors onto the an off-axis parabolic mirror. With a low-power visible laser diode and a set of post-mounted irises, the optical path of the laser beam is adjusted by changing the tilting angles of the mirrors. The parabolic mirror then focuses the beam to a narrow $\approx 3mm$ line-segment The width of SNAP resonator is determined by the off-axis parabolic mirror. It is necessary to carefully adjust the angle of parabolic mirror so that the focused laser beam line-segment is 90° to the SNAP fiber. In particular, the optimal annealing power for SNAP fiber with $39\mu m$ diameters and 300 ms laser exposure time was found to be between $7.5W$ (30%) and $10W$ (45%).

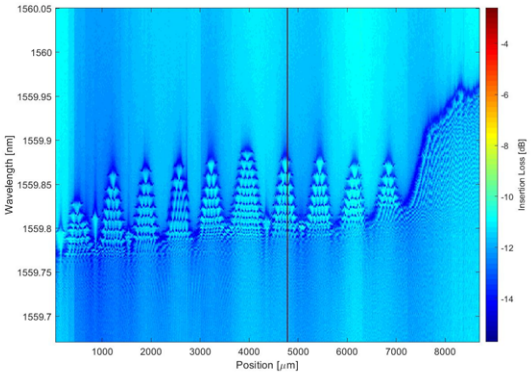

Figure 2.7: Experimental trial on testing optical annealing power

Alignment of Laser Focus Position This is an iterative trial and error process performed in order to determine the focus of the CO_2 laser beam reflected by the off-axis parabolic mirror; the shape of the beam focus resembles a thin strip with length $\approx 3mm$ and width $\approx 300\mu m$.

A two step alignment procedure was used:

1. **Rough focus alignment**
   a white coloured masking tape is attached to the sample holder, the sample holder is then fixed onto a 3D translation stage. The approximate vertical stage position can be determined by comparing the burn marks on the masking tape for different stage height positions resulted from $\approx 100ms$ duration laser exposures controlled by laser shutter, the off-focused beam will have a broader width and lighter colour.
2. **Determine precise focal position**

As seen in Fig. 2.7, the optimal annealing power was found by making a series of annealing points at different positions along the uniform SNAP fiber separated by a distance of at least $\approx 500\mu m$; a constant exposure time of 1 second was used; The laser power variation ranged from $5W$ to $12.5W$.

2.4 Discussion and Perspective

Effective radius variation along SNAP fiber

In practice, microfiber is used to accurately measure the effective radius of SNAP fiber. The transmission spectrum of single microfiber scan along SNAP fiber shows the wavelength variation of whispering gallery modes at successive positions along SNAP fiber. The effective radius variation is then given by the simple relationship:

$$\Delta R = R_0 \cdot \frac{\Delta\lambda}{\lambda_0}$$

Where:

- R_0 and λ_0 are the original effective radius and original resonant wavelength for whispering gallery mode respectively;
- If R represents the new effective radius, then $\triangle R := abs|R - R_0|$ is the change in effective radius;
- If λ represents the new resonant WGM wavelength, then $\triangle\lambda := abs|\lambda - \lambda_0|$ is the change in wavelength.

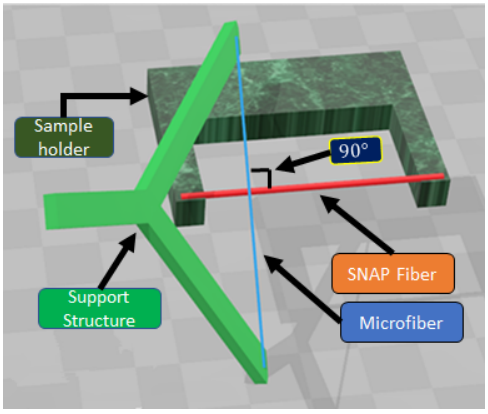

Figure 2.8: Contact coupling between microfiber and SNAP fiber

Choice of Laser Power and exposure time

The choice of laser power and exposure time are two important parameters in the laser annealing the CO_2 laser annealing method because the power used is directly proportional to the heat generated by the SNAP fiber at the laser exposure region.

There exist frozen-in tension inside the SNAP fiber during its manufacturing process. When CO_2 laser with appropriate power is directed onto the surface of an uniform SNAP fiber, the frozen-in tension is released and results in an local increase of effective radius variation along the SNAP fiber.

Exposure time of CO_2 laser
it is typically chosen in the range of 100 ms to 1000 ms. The exposure time is controlled by simply opening or closing the optical shutter with minimum exposure time of $10ms$. A repeating open and close sequence of exposure times is also useful for fine tuning the effective radius of SNAP bottle resonators.

Thus the CO_2 laser power and exposure time together determines the accumulated power/heat received by the exposed SNAP fiber. Before making SNAP bottle resonators, it is important to first determine the power threshold for which the frozen in tension can be released, P_t. As seen in Fig. 2.9a, below this threshold there will be no annealing effect, instead the laser exposure resulted in an indent on uniform SNAP fiber. For $P \gg P_t$, the SNAP resonator "sinks" below the uniform level surface, as shown in 2.9b.

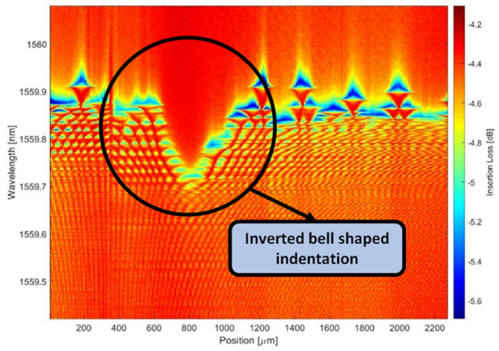

(a) Insufficient laser power

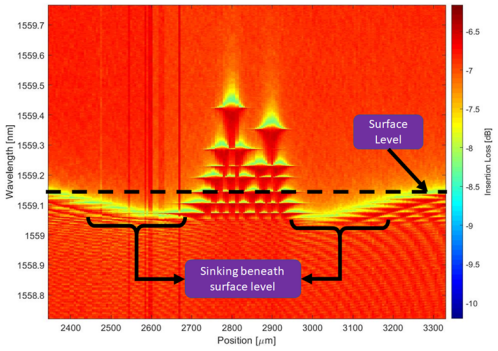

(b) Too much laser power

Symmetric SNAP Double Well Micro-resonator

The fabrication procedure for SNAP double well resonator is essentially involves making two closely separated SNAP bottle resonators with the same . The precise nano-engineering of the shape and separation is an important technique of SNAP technological system that requires a significant amount of practical experience.

Chapter 3

Microfiber Fabrication and Coupling

3.1 Literature Review: Micro/nano-fiber

As early as 1880s, British scientist Boys [13] tried to produce glass filaments from high temperature molten ores, and studied their mechanical properties and applications. Because of the limitation of condition and technology, no rigorous research could be conducted at that time. It was not until a century later, when the theory of optical waveguides was fully established, that researchers began to study the optical applications of MNFs made from glass fibers. Due to the amorphous and viscous properties of glass materials, it is possible to obtain optical fibers with micron order diameter by using flame or laser heating to draw glass fibers. In a typical MNF drawing system, an ordinary bare fiber is heated with a flame that can be moved back and forth. When the central part of the fiber is heated to softening temperature, a certain amount of tension is applied at both ends of the fiber to make the fiber stretch to both sides. MNF can be obtained in the middle of the fiber by accurately controlling the temperature and stretching speed of the heating source. The MNF fiber fabricated by this method has the advantages of high surface smoothness, good diameter uniformity, long length and convenient for subsequent operation. In order to obtain MNF with smaller diameters, the flame heating two-step stretching method was put forward[100] . The MNF with micron diameter were used as raw materials, which were confined by heated sapphire fiber cones and stabilized in high temperature tensile region. MNF as small as 50nm were prepared by further stretching, and good diameter uniformity was maintained. In order to improve the repeatability and reduce the optical transmission loss Brambilla et al. [16] ultra-low loss micro-nano fiber has been prepared with high repeatability by improving the heating source of the commercial fiber coupler. Sumetsky [87] and Ward et al. [104] used CO_2 laser heating source.

Classification of heat-and-pull microfiber fabrication

MNF fabrication techniques can be divided into top-down and bottom-up. [12] Top-down method makes MNF by gradually reducing the size of a macro-scale preform while bottom-up method grows MNF from a seed preform of only a few nanometers. [29, 12] According to above definitions, the heat-and-pull taper drawing method belongs to the top-down category. Tong and Sumetsky [100] Basic heat-and-pull setup for tapering MNF consist of: a heat source, a pulling system, and a transmission spectrum measuring device; since temperature fluctuations can have detrimental effect on the success rate and quality of MNFs the purpose heating control is to maintain the optimal softening state as the fiber diameter gets thinner the control of heating is of particular importance: Common heating methods can be classified into direct and indirect heating. Direct heating is the direct contact between heat source and optical fiber. The indirect heating method involves heating through a micro-furnace, in comparison this method have many advantages which will be discussed in the following paragraphs. The conventional heat sources

includes: gas flame, CO_2 laser and electric heater. [11, 14, 104, 100] In the following pages, I will narrow down our attention to the CO_2 laser approach and discuss the advantage of using CO_2 laser in combination with sapphire tube.

CO_2 laser heating method

CO_2 laser as heat source for drawing fibre have a history of almost half a century: CL "Melt-drawing" method had been a widely-used procedure for coupler fabrication: As early as 1974, Paek [66] already applied cw CO_2 setup to heat a glass rod preform pulled by a reel. In 1997, Yokota et al. [117] applied pulley-weight system into his CL fibre-drawing setup.

Advantages of CO_2 laser heating Unlike OH gas flame, CO_2 laser heating is free of OH absorption peak, contamination of chemicals and it is not easily disturbed by the environment such as air convection.[100, 14] Furthermore, the CO_2 laser method can that offer consistent performance and easy heat control: Tong and Sumetsky [100, pg. 32] mentioned CO_2 laser was chosen because its power is absorbed strongly and readily converted into heat for glass and many types of photonic crystals. Indeed, the heat generated is proportional to the power of CO_2 laser beam fibre-glass absorbs. [14] So the heating temperature can be reliably controlled by adjusting the laser output power or by focusing/defocusing the laser beam with a lens. [95, 27]

Problems with direct CO_2 laser heating

- **"Self-regulating" limitation**
  Due to the "Self-regulating" limitation of direct laser heating cannot to obtain very thin microfibre using direct laser heating. [95]. This is because the taper drawing process requires the heated fibre glass to reach a degree of viscosity such that: it is soft enough to be pulled without breaking or creating surface cracks, and at the same time not too soft to bend downwards under its own weight: the heat supplied through laser absorption depend on fibre glass volume, while heat dissipation depends on surface area; thus as taper waist diameter, d, is tapered thinner, the heat supply decrease according to d^2; the heat escape from fibre glass surface decrease according to d; so eventually when there is insufficient heat to sustain the softened state, breaking occurs.
- **Uniform Heating**
  One major problem with direct heating of a fixed spot laser is uneven heat distribution along the axial direction and around the cross-section of the optical fiber heated under such a hot-zone. [104, 80, 27] The most frequently adopted method to improve uniform heating along the axial direction is high frequency"Mirror scanners". [64, 21, 52, 6, 104, 67, 44, 105] and axially symmetric heating set-up can be used to counteract the problem of cross-sectional temperature gradient. [64, 65] However, the above solutions considerably increases the design complexity and alignment difficulty of the fabrication rigs.

Advantages of CO_2 laser and sapphire tube approach

The theoretical basis of CSS method was established by T. Birks and Y. Li. According to their 1992 paper [11], MF shape can be determined by change in hot-zone length, L, during heat drawing process. The portion of fiber glass inside L must be equally heated, and there must be zero heating outside it; under this assumption, if appropriate heating and tension is applied, the heated fibre section have uniform viscosity; therefore it will be "uniformly stretched" and maintains a cylindrical shape. Controlled Variations of L during heating process can produce a collection of microfibre shapes.

In 2004, a indirect heating method was first presented bySumetsky et al. [95], which used sapphire tube together with CO_2 laser to generate heat. The sapphire tube is used as a micro-furnace with standard

single mode optical fiber placed inside it; The sapphire tube is then heated with CO_2 laser, NMFs with sub-micron diameter was achieved.[95]

In the following 15 years, this configuration have been applied and discussed by many researchers:

- Ward et al. [104] stated that this method is capable of achieving fiber diameters of below 100nm and mentioned that compared with direct laser heating, the requirements for beam focusing and taper alignment are less strict.
- Huang et al. [38] used this setup for CDLHPG fiber growth and demonstrated that with sapphire tube, the uniformity of fiber core is increased, and the vertical temperature gradient is minimised; they also pointed out with the aid of the sapphire tube as a heat capacitor, heat fluctuation is minimised and the propagation loss was also improved.
- Xu [115] observed that the size of the beam along the sapphire tube can be flexibly controlled by changing the lens focus, he further added that the tapering motion can be automated by computer and the final profile can be tailored to a given desired shape. Xu [115] also described this method as: "very fast and provides very short nano-wires tapers ".
- Ginu Rajan [29]explained that the CO_2 laser method/sapphire tube has more flexibility than the original flame brush method, and can be used to prepare MNFS with lower OH content.
- Takizawa et al. [99] demonstrated the fabrication of H-LPFG obtained with sapphire tube (used as a miniature oven), the fiber inside can be heated uniformly and the softening temperature of the fiber was easily obtained by adjusting the power of the CO_2 laser.
- Mullaney [61] mentioned directly heating the sapphire tube by scanning its outer surface with CO_2 laser can produce in sub-micron diameter tapered waist because that the sapphire tubes increases the temperature of fiber encapsulated inside. These nano-tapers can effectively couple light and high-Q micro-cavities.
- Gai et al. [27] reported that sapphire tube can exhibit good thermal conductivity under the laser radiation when the fiber inside the tube is gradually heated to a melting state. The heating temperature can be easily controlled by adjusting the output power of the CO_2 laser and the distance between the laser and sapphire tube. This setup have high reliability and reproducibility.

CSS setup share all the advantages of the CO_2 laser method; the addition of sapphire tube provided significantly improved heating stability and efficiency:

Stable and efficient heating

Firstly, heating fiber indirectly via sapphire tube overcomes the self-regulating limitation by increasing the heating efficiency of CO_2 laser allowing thinner MNFs to be fabricated. Secondly, the hot-zone inside the sapphire tube provide constant, stable heating since the sapphire tube has much a much greater mass and volume than the fiber inside it, a large amount of stable heating is generated and the reduction of fiber diameter during the fiber drawing process has no effect on the inside temperature of the sapphire tube.Bozeat et al. [14], Huang et al. [38], Sumetsky et al. [95], Sumetsky [90].

Modified pulling technique

Pulling technique is important for making high standard micrfibers with adiabatic profile, long taper transition and high surface smoothness. Non-adiabatic taper profile typically directly result in high transmission loss of several decibels and is likely to be detrimental when coupling to the fundamental mode of a micro-resonators.[11, 115] CO_2 laser can either be moving [99, 67] or stay staionary [95]

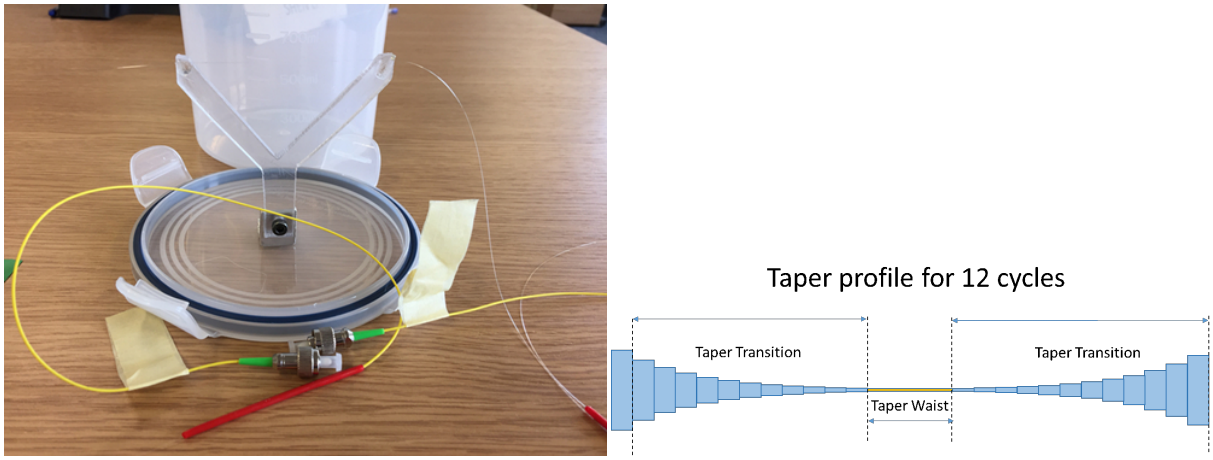

(a) Microfiber Photo (b) Microfiber Illustration

during the tapering process.[14] The most used pulling technique involves gradually stretching the fiber under heating in opposite directions. [29] The modification made on pulling technique of CSS have greatly improved the transmission, it is described byBirks and Li [11] requires“a point-like heat source” which oscillates back-and-forth, at a speed much greater than taper elongation speed in order to create an “time-average hot-zone”. Taper profile depend only on the hot-zone length.[11] CO_2 laser is a good option because it closely matches the assumption of a point-like heat source: at any given time, most of its power is confined to only heat a very small section of the sapphire tube. The time-averaged hot-zone is created by the periodic, back-and-forth periodic drawing movement of two linear translation stages.[90, 61]

3.2 Fabrication Procedure of microfibers with CSS Configuration

The structure of tapered fiber is shown in Fig. 6.6:

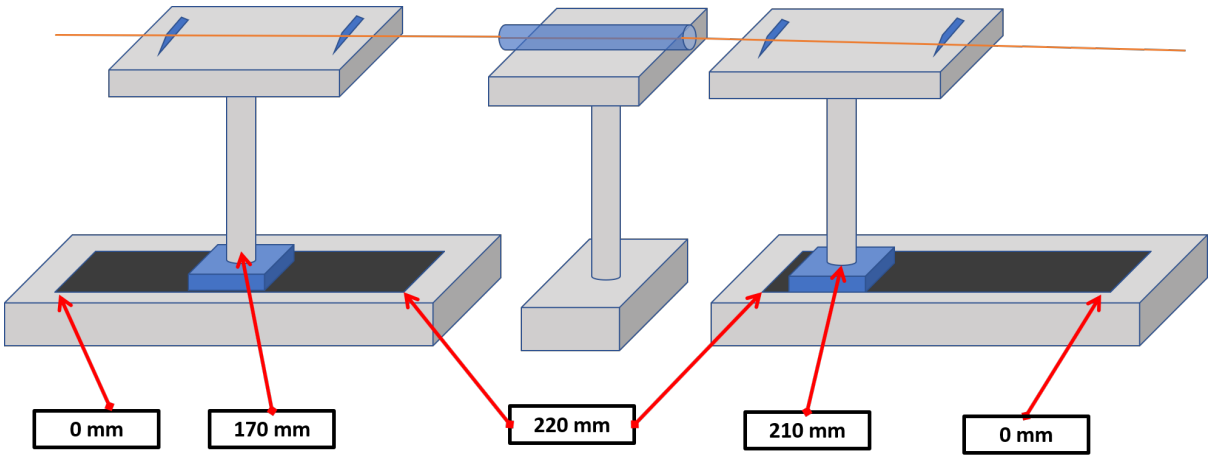

Figure 3.2: Heat-and-pull rig

The main microfiber fabrication procedure are shown in the following tables :

Procedure	What?	How?	Why?	Additional Info
1. Set	Translation stage start position	Stage control software	Ensure enough room for pulling	Stage travel range = 230 mm LHS stage position = 170 RHS stage position = 210
2. Warm-up	CL	Switch on water cool and CL; Set to required power level; Wait 30-35 minutes.	Laser power stability is a crucial factor to MF fabrication success rate; therefore, it is important to wait sufficient time to let CL to reach stability.	Particularly important when operating power is > 50%
3. Clean	ST	Blow inner surface with compressed air can.	Avoid MF contamination	Heat ST during warming up can also burn off dust on the inner surface of ST.

Table 3.1: MF Fabrication Table 1

4. Align	5. Prepare	6. Insert
Centre of CL beam with centre of ST	125 µm Single-mode Optical Fibre	OF_A through ST
Set laser to 8%; Place light coloured cardboard ST; Determine alignment by comparing burn mark colours produced by laser passing by the top and bottom edge of ST onto cardboard; Adjusting reflector mirror accordingly.	Obtain two strands $\approx$ 1 m long optical fibre, OF_A and OF_B	Leave about half of OF_A on either side of ST
Ensure ST receive equal heating	Needed for subsequent steps	The closed loop with LUNA detector need to go through sapphire tube.
	Simple trick: unroll approximately 1 m of fibre from its spool; form a bight with the fibre close to spool side; make a tennis ball sized loop by twisting the bight 180°; slowly pulling the tag end while loosely pinching the crossing point with fingers to reduce the size of this loop continuously until the loop splits in half due to excess tangential stress.	Special care must be taken not to accidently touch SF during this step, doing so could alter its alignment.

Table 3.2: MF Fabrication Table 2

7. Strip	Fibre Buffer & Jacket	Use mechanical fibre stripper	Expose 125 μm fibre cladding ready for tapering procedure	A firm constant pressure applied at the stripper handles is necessary to achieve clean and even stripping result.
8. Wipe	Stripped fibre	Squeeze the wash bottle to apply small amount of methanol onto low-lint tissue; use the wetted area to wipe any remaining residue off fibre cladding surface.	Unclean surface if heated cause MF to contain impurities and shorten the lifetime of ST.	Because there's often a sharp discontinuity at the striped and unstriped fibre intersection, wiping in the general direction: from unstriped to can minimise the possibility of fine fibre hairs caught at this position.
9. Cleave	Stripped fibre	Fibre cleaver	Fibre cleaving is a preparation step for splicing, its purpose is to create flat end-face.	Leave 13mm of unstriped length; waste fibre ends are very sharp, disposed into waste bin using tweezers
10. Spice	Cleaved fibre	Fiber Splicer	Form light path; measure insertion loss with OVA	LHS of OF_A is spliced to pigtail connected to OVA input; RHS of OF_A is spliced to OF_B; RHS of OF_B is spliced to OVA output.
11. Align	Fibre inside ST	Use camera to check fibre and ST adjust alignment level repeatedly, position fibre along rotational axis of ST	Heat unstripped fibre inside sapphire tube	The splicing part should be

Table 3.3: MF Fabrication Table 3

12. Clamp	Clamp 1st and 3rd quarter of OF_A and OF_B	Clamp fibre onto translation stages	To control fibre during heat-and-pull process	Apply about $\frac{1}{2}$N of Initial tension; 2 sets of clamps used to increase stability.
13. Set	LUNA OVA software	Set central wavelength to 1550nm and wavelength range to 10nm	Measure IL	Leave LUNA OVA to continuous scan mode
14. Run	Taper drawing LabVIEW Program	Enter cycles number inside LabVIEW program; Open laser shutter; Start LabVIEW once ST reach maximum brightness.	Sapphire tube takes about 7-8 seconds to soften fibre inside.	
15. Monitor	Camera and IL spectrum		Fibre height inside sapphire tube indicates amount of tension;	
16. Decrease	Laser Power	Decrease if fibre is about to touch side of ST	Prevent overheating. Increased fibre tension, avoid fibre touching the side of ST	Normally decrease by 0.5% each time.

Table 3.4: MF Fabrication Table 4

17. Close	18. Run	19. Apply	20. Store	21. Splice
Laser shutter	Synchronous Translation LabVIEW program	Epoxy	Inside air-tight storage container	MF and pigtail connectors
Once LabVIEW programme progress reaches 100%	Enter moving length and speed	Clean support structure with methanol wipe; Use mechanical stage to position support structure;	Clean storage container	
Fabrication process completed	Move MF out of sapphire tube			
	Normally 60mm for 15 pulling cycles			

Table 3.5: MF Fabrication Table 5

3.3 Microfiber Theory

3.3.1 Microfiber Coupling Theory

In this subsection, the theoretical knowledge of microfiber coupling is introduced. The MF used have a waist diameter of $\approx 1\mu m$ and a low insertion loss (usually less than 2%). The fact that MF allows the efficient and controllable excitation of WGMs inside high Q SNAP cavity is an important basis for the following theory.

MF/SF Evanescent Field Coupling

Mode coupling theory views coupling of two optical elements as the mode field matching between them. There is no coupling between ordinary $125\mu m$ single mode optical fiber because of the mode field mismatch. Tapered microfiber have high coupling efficiency due to its micron-scale diameter and adiabatic shape of tapered microfiber.

Function of Microfiber

The evanescent field around the waist of a narrow tapered microfiber can launch light tangentially into the circular cross-section of SNAP cavity and produce optical resonances in form of WGMs. [10] Close to the inner surface of SNAP fiber, the WGM is sustained by repeated internal reflections at near-grazing angles. Microfiber that touches SNAP fiber at right-angles performs two primary functions: firstly, if the microfiber is connected with a light source, it is used as an active optical excitation component to launch WGM around the SNAP fiber; secondly if it is connected to a photodetector, then it can be used as a passive sensing component to detect axial mode distribution along SNAP fiber. In SNAP, the leakage of light in the vicinity of the resonance wavelength λ_{res} is very small; the experimentally measured Q-factor at the corresponding cut-off frequency is: $Q = \frac{f_{res}}{FWHM} \approx 10^6$.

Coupling Efficiency In order to ensure efficient evanescent field coupling, the polymer coating of both SNAP fiber and microfiber is removed to expose the fibre core and cladding which are both made from silica with the same refractive index prior to the coupling procedure. However not all wavelengths can be coupled into a SNAP fiber — only the ones that can interfere constructively after it makes a round-trip; the discrete set of wavelengths which can be coupled into the fiber depends on its diameter. Indeed it can be seen from insertion loss spectrum that:

1. The resonance modes have multiple narrow Lorentzian shaped transmission dips spaced at regular intervals;
2. The dips correspond to higher order modes appears to have shorter spacings.

In fact the diameter can be found from the FSR of the coupling dips seen on the transmission spectrum. The diameter measurement resolution depends on the FWHM of the dips, thus for a given resonance, higher Q-factor would give sharper resolution. Provided the wavelength range of the broadband light source is wide enough, the effective radius variation change can be directly measured from the shift of resonance dips of the insertion loss spectrum. If only one resonance mode is considered, as the diameter of the SNAP fiber gradually increases along the positive axial direction z, the centre of resonance dip will be shifted in the diffraction of increasing wavelength.

Coupling Losses

For a high Q-factor resonating cavity the two main causes of transmission loss is coupling loss and inter-modal transition loss. The coupling loss due to scattering can be reduced by choosing the under-coupling or critical-coupling regime instead of the over-coupling regime. The scattering loss causes the based-line insertion loss of the microfiber transmission spectrum. Another factor that can increase

the coupling efficiency is let the microfiber shape satisfy the adiabatic criterion, for instance a long and smooth taper transition.

3.3.2 Microfiber Measurement Theory

The Jones Matrix and Optical System modelling

The transmission spectrum through microfiber was measured by LUNA OVA 5000 optical vector analyser. The OVA uses the Jones matrix approach to characterizing optical fiber components. In general, input from light source into an optic fiber may contain two orthogonal polarisation modes M_1 and M_2. Subsequently, depending on the particular configuration of the optic system, the amplitude and phase of light will be changed for output modes O_1 and O_2 in the same polarisation directions. Jone matrix, $J(\omega)$, is used by R. C. Jones in 1941 to represent the effect of an optical component on the polarization state of light. Thus with the Jones matrix representation the optic system above can be expressed as:

$$\begin{pmatrix} O_1 \\ O_2 \end{pmatrix} = \begin{pmatrix} J_{11}(\omega) & J_{12}(\omega) \\ J_{21}(\omega) & J_{22}(\omega) \end{pmatrix} \begin{pmatrix} M_1 \\ M_2 \end{pmatrix} \tag{3.1}$$

where J_{11}, J_{12}, J_{21} and J_{22} are scalar functions of optical frequency ω. If an composite optical device D, is made up of N basic optical components $D_1, D_2, \cdots, D_N$ then the resulting Jones matrix for D is then the matrix product $J_D = J_{D_1} J_{D_2} \cdots J_{D_N}$. In SNAP experiments: microfiber and SNAP fiber are the most basic optical components.

In order to make reliable insertion loss measurements, the axial direction of SNAP fiber must be carefully adjusted such that it is perpendicular to the evanescent field line direction of the microfiber, this is because at off-perpendicular angles the light coupled into the SNAP fiber will trace an elliptical or helical path instead of a circular path. Jones matrix can be used to calculate all other transmission parameters.

High-Resolution Measurement of SF Diameter Using WGMs

In SNAP experiment, the microfiber is used as a sensor fiber, it used to determine the diameter variation of along SNAP fiber.

The transmission spectrum through a MF was measured using LUNA optical spectrum analyser when the MF and SF were coupled (placed in contact at right angles). The coupling causes small external scattering loss in the transmission spectrum, which was used to detect when the fibers touched. Fig. 3.3 shows the transmission spectra of a $1\mu m$ diameter sensor fiber coupled with a $38\mu m$ SNAP fiber, measured using the broadband light source of LUNA OVA 5000. The transmission spectrum have resonance dips at wavelengths where light was coupled into a WGM in the target SF. Only first order WGMs can be seen from the spectrum since the coupling strength had been carefully controlled to eliminate any higher orders of WGMs.

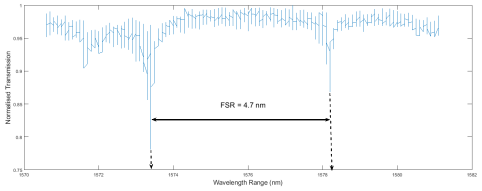

Figure 3.3: Coupled SF/MF Transmission Spectrum

The FSR calculated from formula is close to measurement:

$$\Delta\lambda_{FSR} = \frac{\lambda_{res}^2}{\pi \cdot D \cdot n} = \frac{(1578.2nm)^2}{\pi \cdot (125\mu m) \cdot 1.41} \approx 4.5nm \tag{3.2}$$

3.4 Discussion and Perspective

3.4.1 Taper waist diameter estimation based on volume conservation

For practical applications, it is very useful to predict the final diameter of taper waist. Both right and left translation stage have travel range: $220mm$. N_L and N_R from the table represents the positions of the right and left stages respectively.

i	N_L	N_S
0	170	210
$\frac{1}{2}$	173	196
1	169	199
$\frac{3}{2}$	172	195
2	168	198
...	...	...

Table 3.6: Stage Pulling Positions

At any instant during tapering, both translation stages always move in synchronisation and in the same direction; The stage that moves away from the sapphire tube, referred as the "**leading stage**", moves at ?$0.8mm/s$ a slightly faster speed than stage which moves towards towards the tube, referred as the **"catching-up stage"** with speed $0.05mm/s$; More precisely, the stages completes a $\frac{1}{2}-cycle$ movement means the leading stage achieves $4mm$ of travel length while the catch-up stage simultaneous travels by $3mm$; This results in $1mm$ of pulling length.

At the start of subsequent $(i+\frac{1}{2})th-cycle$: both stages begin to reverse direction; the roles of both stages are reversed so that the leading stage becomes catch-up stage and verse versa. The laser source directed at the sapphire tube is intended to mimic a point heating source; In practice it has a beam diameter of $\approx 3mm$. The cycle number, i indicates the particular time-event during tapering process, when both translation stages stops moving and start to turn back, accelerate and move in the opposite direction. In brief, there had been differing judgements over what value to set for this "instant stoppage time"; however according to practical experience, it was chosen to be $150ms$. Suppose the initial fibre diameter $= d_0$; the heat-zone length $= L$; pulling length after each $\frac{1}{2}-cycle = \delta L$. Apply the law of volume conservation: After first $\frac{1}{2}$-cycle is:

$$\pi \cdot (\frac{1}{2}d_0)^2 \cdot L = \pi \cdot (\frac{1}{2}d_{\frac{1}{2}})^2 \cdot (L+\delta L) \tag{3.3}$$

So,

$$d_0 = d_{\frac{1}{2}} \cdot \sqrt{\frac{L}{L+\delta L}} \tag{3.4}$$

After second $\frac{1}{2}$-cycle is:

$$\pi \cdot (\frac{1}{2}d_{\frac{1}{2}})^2 \cdot L = \pi \cdot (\frac{1}{2}d_1)^2 \cdot (L+\delta L) \tag{3.5}$$

So,

$$d_{\frac{1}{2}} = d_1 \cdot \sqrt{\frac{L}{L+\delta L}} \tag{3.6}$$

Therefore, the fibre waist diameter after ith-cycle is:

$$d_i = d_0 \cdot \left[\sqrt{\frac{L}{L+\delta L}}\right]^i \tag{3.7}$$

Chapter 4

Transmission spectrum of SNAPs with Single input/output Configuration

In this chapter, we present one microfiber scan as the evanescent light field is send by microfiber into SNAP fiber is strongly confined by the sharp refractive index discontinuity at the glass/air media boundary.

4.1 Theory for measuring SNAP fiber with microfiber

4.1.1 Foundamental Parameters

We study the WGM mode distribution through the formulations of 4 key parameters used especially to express the evanescent field strength being coupled into SNAP fiber. These parameters can either be directly quantified or precisely adjusted in experimental setting. The following outline briefly explains their practical significance:

- **Wavelength, λ**
  From Equation 2.5, wavelengths gives the energy of the tunable $\lambda_{res} \pm 2\ nm$ laser diode of LUNA. The general observation from experiment agrees with basic SNAP theory that only certain wavelengths separated by the free spectral range can be coupled into the SNAP fiber. These wavelengths must all satisfy the total reflective boundary condition of the SNAP cavity. Due to the high Q-factor thermal-drawing-process of preform silica fiber; the resonance bandwidth (FWHM) is very narrow, typically within a central range of $\pm 2nm$.

- **Axial coupling position along SF, z**
  The coupling position of microfiber along SF is represented by z. In SNAP experiments, the movement of 2D linear translation stages with a maximum travel range of $15/;mm$ is precisely controlled and recorded as numerical data for z. The z with step size $< 5\mu m$ is then plotted against MF transmission amplitude on spectrum-grams showing resonant wavelengths/effective radius variations at adjacent positions along a SNAP fiber.

- **Coupling Parameter, C_1**
  C_1 models the coupling strength, viz. the amount of light coupled into SNAP cavity from the microfiber. In practice, we want to control the degree of coupling or mode matching to only excite the fundamental mode with a single resonance peak. This is achieved by controlling the microfiber translation stage along the direction of its adiabatically tapered profile. The regime of

under-coupling is generally prefer to over-coupling because of its two advantages namely reduced scattering loss and simplification subsequent data analysis.

- **Imaginary Parameter,D_1**
  Parameter D_1 is represented by an imaginary quantity, its real and imaginary parts have separate meanings. The observation of shift in resonance peaks which reflect changes in effective SF radius variation is indicated by a corresponding change in the real part.

4.1.2 Green's function and renormalised Green's function

Sumetsky [89] in the a series of publications introduced and described: "SNAP is a record accurate and low loss platform for fabrication of complex miniature photonic circuits. SNAP device consists of an optical fibre with specially introduced nanometre-scale radius variation, called the SNAP fibre (SF), and transverse input/output wave-guide (SF) coupled to SF"

Sumetsky [89] in 2012, defined SNAP device as follows: "A SNAP device consists of an optical fibre with introduced nano-scale effective radius variation, which is coupled to transverse input/output WG. The input WG excite whispering gallery modes circulating near the fibre surface and slowly propagating along the fibre axis."

$\overline{G}(z,z')$ from the equations above is the renormalised Green's function. It is derived from the bare Green's function, $G(z,z')$ of the cylindrical cavity of SNAP fiber by assuming there is no coupling effect from microfiber. The renormalised $\overline{G}$ takes care of the SF/MF coupling loss.

In the case of one microfiber, if the Green's function, $G(\lambda,z,z')$, is the particular solution to the inhomogeneous time independent Schrödinger equation:

$$\frac{d^2G(z,z')}{dz^2}+\beta^2G(z,z')=\delta(z-z') \tag{4.1}$$

Then the renormalised Green's function satisfies the equation:

$$\frac{d^2\overline{G}(z,z')}{dz^2}+\left[\beta^2(\lambda,z)+D_1\delta(z-z_1)\right]\overline{G}(z,z')=\delta(z-z') \tag{4.2}$$

In the case of SNAP fiber, because of a cylindrical cavity shape, the relationship between the bare Green's function and renormalised Green's function for such a cavity shape can be determined analytically.

When radiation wavelength is close to the resonance λ_{res}, the propagation constant, β, is small which means WGMs light have a slow axial propagation speed.

Since the waist diameter of microfiber is $\approx 1\mu m$ which is much smaller than the axial wavelength of SNAP fiber, $\lambda_\beta := \frac{2\pi}{\lambda_{eff}} \approx 38\mu m$, the coupling of microfiber is modelled as delta potentials:

$$D_n\delta(z-z_n) \tag{4.3}$$

Where D_n is an imaginary number which represents the coupling between SNAP fiber and the nth microfiber; its real part represents coupling phase shift and its imaginary part represents coupling loss due to coupling to the nth microfiber. The amplitude of transmission through a microfiber is coupled into SNAP fiber. SNAP fiber typically have a smooth cylindrical shaped cavity. The distribution of WGMs along SNAP fiber satisfies the one-dimensional Schrödinger equation therefore it can be used to simulate phenomenon in quantum mechanics.

4.1.3 SNAP fiber coupled to a single microfiber

If SNAP fiber is coupled only to a single microfiber, the transmission amplitude for the single microfiber is written as:

$$S_{11}(\lambda) = S_{11}^{(0)} - i|C_1|^2\overline{G}(\lambda, z, z') \tag{4.4}$$

In this case, the renormalised Green's function in 4.2 is related to the bare Green's function through the following expression:

$$\overline{G}(\lambda, z_1, z_2) = \frac{G(\lambda, z_1, z_2)}{1 + D_1 G(\lambda, z_1, z_1)} \tag{4.5}$$

Therefore, S_{11} can be written in terms of the bare Green's function

$$S_{11}(\lambda) = S_{11}^{(0)} - \frac{i|C_1|^2 G(\lambda, z_1, z_1)}{1 + D_1 G(\lambda, z_1, z_1)} \tag{4.6}$$

The lossless resonant transmission is a theoretical construct of the coupling situation between the SNAP cavity and microfiber by making the following two assumptions:

- The microfiber have no transmission loss;
- There is no scattering loss between the microfiber and SNAP fiber.

In practice, the first assumption is comparable to a microfiber with adiabatic shape and the second assumption corresponds to the situation of non-contact coupling or weak coupling.

$$S_{11}(\lambda) = \frac{1 + (ReD_1 - \frac{i}{2}|C_1|^2)G(\lambda, z_1, z_1)}{1 + (ReD_1 + \frac{i}{2}|C_1|^2)G(\lambda, z_1, z_1)} \tag{4.7}$$

Because there is no scattering loss, $|S_{11}^{(0)}| = 1$, $|S_{1n}^{(0)}| = 0$ and $ImD_1 = \frac{1}{2}|C_1|^2$ In comparison with lossy coupling, $|S_{11}| < 1$ and $|S_{11}^{(0)}| < 1$, the values of $S_{11}^{(0)}$, C_1, and D_1 are restricted by the inequality:

$$Im(D_1) > |C_1|^2 \frac{1 - Re(S_{11}^{(0)})}{1 - |S_{11}^{(0)}|^2} \tag{4.8}$$

These inequalities are useful conditions for the numerical simulation of experimental data.

The Green's function of a SNAP bottle resonator near energy eigenvalue E_n is written as:

$$G(\lambda, z, z') = \frac{\Psi_n(z)\Psi_n(z')}{E(\lambda) - E_n + i\Gamma_0} \tag{4.9}$$

The loss in SNAP fiber, γ_{res}, determines the resonance width, $\Gamma_0 = (8\pi^2 n_{f_0}^2/\lambda_{res}^3)\gamma_{res}$

Thus transmission amplitude obtained from 4.6 corresponds to the Fano formula:

$$S_{11}(\lambda) = S_{11}^{(0)} - \frac{i\Lambda_n}{(E(\lambda) - E_n - \Delta_n) + i(\Gamma_0 + \Sigma_n)} \tag{4.10}$$

$$\Gamma_n = |C_1|^2\Psi_n^2(z), \quad \Delta_n = -Re(D_1)\Psi_n^2(z), \quad \Sigma_n = Im(D_1)\Psi_n^2(z_1) \tag{4.11}$$

The self-energy term , Σ_n, have a strong dependence on the intensity of WGM, $\Psi_n(z)$ and losses due to leakage into SNAP resonator, $Im(D_1)$. At the nodes of axial distribution of WGMs, $\Lambda_n = \Sigma_n = 0$ Coupling also shifts the resonance position by Δ_n, which is a function of phase shift, $Re(D_1)$. On the other hand, the largest coupling is at the axial WGMs antinodes.

For lossless scenario,

$$S_{11}(\lambda) = \frac{(E(\lambda) - E_n - \Delta_n) + i(\Gamma_0 - \frac{1}{2}\Lambda_n)}{(E(\lambda) - E_n - \Delta_n) + i(\Gamma_0 + \frac{1}{2}\Lambda_n)} \tag{4.12}$$

4.1.4 Bare Greens Function Construction Method

The bare Green's function of uniform SNAP fiber can be found analytically, in most other cases the bare Green's function has to be determined by numerical method. In the following section, we present the construction method for finding the bare Green's function:

Green's function based on δ-function can be applied to solve ODEs. For a general, inhomogeneous, second-order differential operation, L ODE defined on interval $[a,b]$:

$$L\Psi(z) = \alpha(z)\frac{d^2}{dz^2}\Psi + \beta(z)\frac{d}{dz}\Psi + \gamma(z)\Psi = f(z) \tag{4.13}$$

where α, β, γ are continuous functions on $[a,b]$, and $\alpha \neq 0$ (except at a finite number of points). The forcing term $f(z)$ is finitely bounded over the interval $[a,b]$. Then the Green's function, $G(z,z')$ for differential operator L can be defined as:

$$LG = \delta(z-z') \tag{4.14}$$

In addition, the homogeneous boundary conditions must be satisfied by $G(a,z) = G(b,z) = 0$. The usefulness of Green's function is that if $G(z,z')$ is the solution to equation 4.14, then the general problem $L\Psi(z) = f(z)$ can be solved by writing

$$\Psi(z) = \int_a^b G(z,z')f(z')dz' \tag{4.15}$$

Thus,

$$L\psi(z) = L\left[\int_a^b G(z,z')f(z')dz'\right] = \int_a^b [LG(z,z')]f(z')dz = \int_a^b \delta(z-z')f(z')dz = f(z) \tag{4.16}$$

Since Green's function is the only term depending on z, the constructed $\Psi(z)$ also satisfies the boundary conditions $\Psi(a) = \Psi(b) = 0$. G depends on L, not on the forcing term $f(z)$. Thus G is related to the characteristic of a system, it is the solution of $Ly = f$ for arbitrary forcing term $f(z)$. In other words, $\Psi(z) = L^{-1}f(z)$, where according to equation4.15, the inverse differential operator, L^{-1} corresponds to integration with the Green's function as the integral kernel.

Construction of Green's function The constructive means for finding the Green's function is based on the fact that $z \neq z', LG = 0$. For $z < z'$ and $z > z'$, G can be expressed in terms of the homogeneous equation. Let Ψ_1, Ψ_2 be a basis of linearly independent solutions to the second-order homogeneous problem $L\psi = 0$ on interval $[a,b]$. The basis are defined such that $\Psi_1(a) = \Psi_2(b) = 0$, i.e. each of $\Psi_{1,2}$ satisfies one the the boundary conditions. On $[a,z')$ the Green's function obeys $\mathrm{L}G = 0$ and $G(a,z') = 0$. Any homogeneous solution to $\mathrm{L}\Psi = 0$ obeying $\Psi(a) = 0$ must be proportional to $\Psi_1(z)$, with a proportionality constant that is independent with z. Thus, set

$$G(z,z') = A(z')\Psi_1(z) \quad for \quad z \in [a,z') \tag{4.17}$$

Similarly, on $(z',b]$, the Green's function must be proportional to $\Psi_2(z)$, so set

$$G(z,z') = B(z')\Psi_1(z) \quad for \quad z \in (z',b] \tag{4.18}$$

The coefficient functions $A(z')$ and $B(z')$ must be independent of z.

This construction have been defined for families of Green's function for $z \in [a,b] - \{z'\}$, in terms of functions of A and B . Now join the above two solutions together at the point z = z'. Suppose first that $G(z,z')$ is discontinuous at $z = z'$, with the discontinuouty given as a step function. Then $\partial_z G \propto \delta(z-z')$ and $\partial_z^2 G \propto \delta'(z-z')$. However, the form of equation 4.14 shows that $\mathrm{L}G$ involves no generalised

functions other than $\delta(z-z')$, and in particular contains no derivative of δ-functions. Thus $G(z,z')$ must be continuous throughout $[a,b]$ and especially at $z=z'$.

However, integration over an infinitesimal neighbourhood of $z=z'$ yields:

$$\int_{z'-\varepsilon}^{z'+\varepsilon}\left[\alpha(z)\frac{\partial^2 G}{\partial z^2}+\beta(z)\frac{\partial G}{\partial z}+\gamma(z)G\right]dz=\int_{z'-\varepsilon}^{z'+\varepsilon}\delta(z-z')dz=1 \tag{4.19}$$

Since $G(z,z')$ is continuous and the coefficient functions α,β,γ are bounded, so $\gamma(z)$ is zero as the integration region becomes infinitesimally thin. Also, since G is continuous, $\partial_z G$ must be bounded so the term $\beta\partial_z G$ also cannot contribute as the integration region shrinks to zero size. For the remaining term,

$$\lim_{\varepsilon\to 0^+}\int_{z'-\varepsilon}^{z'+\varepsilon}\alpha(z)\frac{\partial^2 G}{\partial z^2}dz=\alpha(z')\left[\frac{\partial G}{\partial z}|_{z=z'^+}-\frac{\partial G}{\partial z}|_{z=z'^-}\right] \tag{4.20}$$

According to the following two conditions:

Continuity condition:

$$G(z,z')|_{z=z^-}=G(z,z')|_{z=z^+} \tag{4.21}$$

Derivative condition:

$$\frac{\partial G}{\partial z}|_{z=z'^+}-\frac{\partial G}{\partial z}|_{z=z'^-}=\frac{1}{\alpha(z)} \tag{4.22}$$

The conditions 4.17 and condition 4.18 becomes:

$$A(z')\Psi_1(z')=B(z')\Psi_2(z') \quad and \quad A(z')\Psi_1'(z')-B(z')\Psi_2'(z')=\frac{1}{\alpha(z)} \tag{4.23}$$

From the equations above, the two linear equations for A and B are determined to be:

$$A(z)=\frac{\Psi_2(z')}{\alpha(z')W(z')} \quad and \quad B(z)=\frac{\Psi_1(z')}{\alpha(z')W(z')} \tag{4.24}$$

Where $W(z)\equiv\Psi_1\Psi_2'-\Psi_2\Psi_1'$ is the Wronskian of Ψ_1 and Ψ_2.

To summarise, the solution $G(z,z')$ of $\mathrm{L}G=\delta(z-z')$ obeying the homogeneous boundary conditions $G(a,z')=G(b,z')=0$ is given by:

$$G(z,z')=\begin{cases}\frac{\Psi_1(z)\Psi_2(z')}{\alpha(z')W(z')} & \text{if } a\le z<z'\\ \frac{\Psi_2(z)\Psi_1(z')}{\alpha(z')W(z')} & \text{if } z'<z\le b\end{cases} \tag{4.25}$$

The flowchart below shows the code that Matlab determines the bare Green's function.

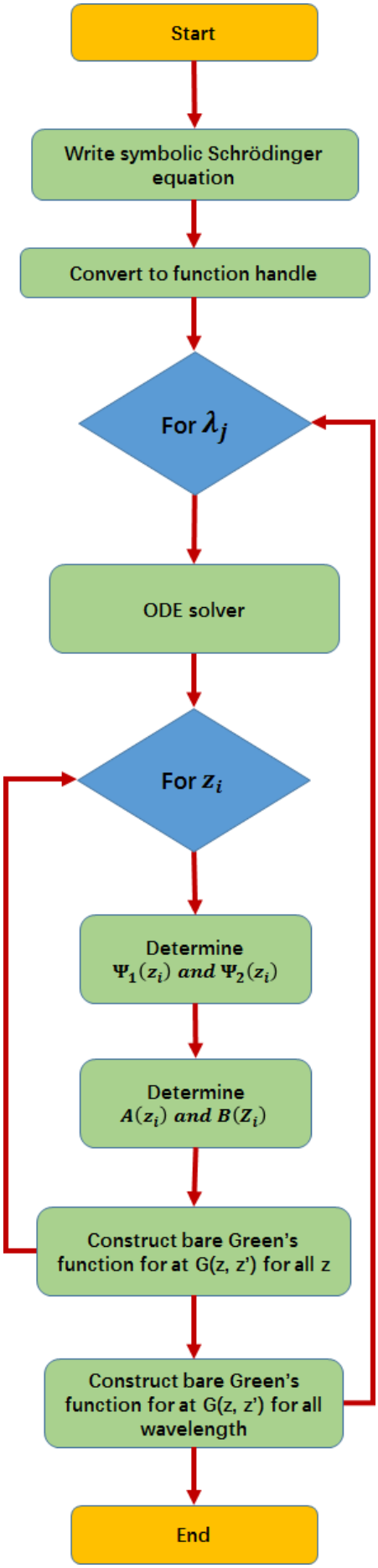

Figure 4.1: Code for bare Green's function

4.1.5 Simulation Algorithm

The MATLAB code for determining the bare Green's function for any potential V(z) is as follows:

```
function [G0] = bareGreensFunction(m1,m2,V1,xstep,D,L0,wavelengthsStart,waveleng
%UNTITLED Calculation of bare Green's function
%   This function takes simulation parameters for calculation of bare
%   Green's function which is scaled using coupling parameters to calculate
%   theoretical spectrogram given an effective radius variation profile.

% Supress warning message of badly scaled matrix
warning('off','MATLAB:nearlySingularMatrix')

%% Set symbolic equations for theoretical model

% Set up 1D Schrodinger equation with appropriate boundary conditions and
% define potential function

% Implement 1D Schrodinger equation with additional parameters
syms Psi1(x) Psi2(x) E V(x)
eqs = [diff(Psi1(x),x) == (E + V(x))*Psi2(x),...
       diff(Psi2(x),x) == Psi1(x)];
vars = [Psi1(x), Psi2(x)];

% Convert symbolic equation to function handle
[~, F] = massMatrixForm(eqs, vars);
F = odeFunction(F, vars, E, V(x));

% Create mirrored potential function
V2 = @(x) V1(-x);

%% The grand loop

% Timing calculation setup
n1 = 10;
n2 = 61;
nDiff = n2-n1-1;

nStart = 100;
nRemaining = 101;
nEnd = 102;
nPeriod = 100;

%Essential parameters for main loop
x00 = -D;
M = m2-m1+1;
N = wavelengthsEnd-wavelengthsStart+1;

magicScalingFactor = 1e6;
G0 = zeros(N,M);
tStart = datetime('now');
```

```
% Bare Green's Function Solver
for n = 1:N
    % Calculate expected end time
        if n==n1
            t1 = clock;
        elseif n==n2
            t2 = clock;
            tDiff = etime(t2,t1);
            tRemainingSecs = (N-n+1)/nDiff * tDiff;
            tRemainingHrs = duration([0,0,tRemainingSecs],'Format','h');

            tCurrent = datetime('now');
            tEnd = tCurrent + tRemainingHrs;
            n1 = n1+nPeriod;
            n2 = n2+nPeriod;
        end

    % Print useful information to matlab command window
    if n == N
        continue;
    elseif n == nStart
        fprintf('\nSimulation start time: %s \n\n',tStart)
        nStart = nStart + nPeriod;
    elseif n == nRemaining
        fprintf('Estimated time remaining: %s \n\n',tRemainingHrs)
        nRemaining = nRemaining + nPeriod;
    elseif n == nEnd
        fprintf('Estimated completion time: %s \n\n',tEnd)
        nEnd = nEnd+nPeriod;
    else
        fprintf('Wavelength calculation: %d of %d. Simulation progress: %.2f%% c
    end

    E_lambda = L0+dL0*(n-1);
    y0 = [1; sqrt(abs(E_lambda))];          % Set boundary conditions

    Psi_test1 = @(x, Y) F(x, Y, E_lambda, V1(x));
    Psi_test2 = @(x, Y) F(x, Y, E_lambda, V2(x));

    q1 = ode45(Psi_test1, [-D D], y0);
    q2 = ode45(Psi_test2, [-D D], y0);

    B10(1,1) = 1;
    B10(2,1) = (-1i*(1-sign(E_lambda)) + (1+sign(E_lambda)))*sqrt(abs(E_lambda))

    % B20 = [1; -B10(2,1)];

    S10(1,1) = deval(q1,-D,2);
    S10(1,2) = deval(q2,D,2);
    S10(2,1) = (deval(q1,-D+1e-6,2)-deval(q1,-D,2))*magicScalingFactor;
    S10(2,2) = (deval(q2,D-1e-6,2)-deval(q2,D,2))*magicScalingFactor;
```

```
    S20(1,1) = S10(1,2);
    S20(1,2) = S10(1,1);
    S20(2,1) = -S10(2,2);
    S20(2,2) = -S10(2,1);

    A10 = S10\B10;
    A20 = [A10(2,1);A10(1,1)];

    qc01 = A10(1,1)*deval(q1,0.1,2)+A10(2,1)*deval(q2,-0.1,2);
    qc02 = A20(1,1)*deval(q1,0.1,2)+A20(2,1)*deval(q2,-0.1,2);

    qc011 = A10(1,1)*deval(q1,0.1+1e-6,2)+A10(2,1)*deval(q2,-0.1-1e-6,2);
    qc021 = A20(1,1)*deval(q1,0.1+1e-6,2)+A20(2,1)*deval(q2,-0.1-1e-6,2);

   W = (qc02*(qc011-qc01)-qc01*(qc021-qc02))*magicScalingFactor;

    for m = m1:m2
        Q01 = A10(1,1)*deval(q1,x00+(m-1)*xstep,2)+A10(2,1)*deval(q2,-x00-(m-1)*
        Q02 = A20(1,1)*deval(q1,x00+(m-1)*xstep,2)+A20(2,1)*deval(q2,-x00-(m-1)*

        G0(n,m-m1+1) = Q01*Q02/W;
    end
end



fprintf('\nSimulation completed at: %s \n\n',datetime('now'))

% Re-enable warning message of badly scaled matrix
warning('on','MATLAB:nearlySingularMatrix')

end
```

The following points should be noted from the code:

1. ODE45 MATLAB solver

ode45 is a tool for solving initial value problems of ODEs. In order to apply ode45, the Schrödinger equation is first written as a group of two first order ODEs. Then the ode45 ODE solver takes the first initial conditions on the left hand side, $\Psi_1(a) = \sqrt{E}$ and works out $\Psi_1(z)$ for $z \in [a, z')$ then the mirror potential function is applied to the second initial condition on the right hand side, $\Psi_1(a) = \sqrt{E}$, which $\Psi_2(z)$ for $z \in (z', b]$, such that $\Psi_1(z)$ and $\Psi_2(z)$ are mutually linearly independent solutions. From the previously described Green's function construction method, the boundary conditions at $z = z'$ thus determines the coefficient functions $A(z')$ and $B(z')$.

2. The boundary conditions

The potential V(x) must be chosen so that the axial mode of SNAP cavity exhibit bounded states, in this situation light field is confined between two turning points of the SNAP cavity. The boundaries a and b are chosen to be away from the turning point positions outside of SNAP cavity, where the the behaviour of wave function $\Psi(z)$ outside the turning points is exponentially decaying field. Alternative the boundary condition can also take $\Psi(z) = 0$ as initial condition far away from the turning points.

3. Determine the Wronskian derivative

Evaluating Wronskian is the most important step for constructing the bare Green's function, while obtaining the is a difficult procedure because at the boundary there is a jump at the z = z' therefore the approach of numerical differential must be used instead. At the two symmetric positions very close to z': $z' - \varepsilon$ and $z' + \varepsilon$, the numerical derivative of ψ is $\frac{\Psi(z'-\varepsilon)-\Psi(z'+\varepsilon)}{\varepsilon}$. In the MATLAB code defines the magicscalingfactor to be 10^6. Because this code constructs Green's function directly, for each wavelength the ode34 solver have to calculate twice, this method is very time assuming, for large resonators the scan can take up to a few hours depending on CUP speed of computation.

The field distribution of WGM adiabatically propagating along the axial direction of an SF with nano-scale smooth radius variation (or equivalently refractive index variation) in the absence of input/output WG is defined as: axial, radial and tangential mode distribution is decoupled and their collective field distribution.

The axial distribution of the WGM and satisfies the time-independent one-dimensional Schrödinger equation:

$$\frac{d^2\Psi}{dz^2} + [E(\lambda) - V(z)]\,\Psi = 0$$

Coupling to WG WG_n is modelled with zero-range potentials: $D_n \cdot \delta(z - z_n)$ which is justified if the wave-guide width is much smaller than the WGM axial wavelength. The latter assumption is in agreement with the experiment, where, typically, the microfibre diameter is $\sim 1\mu m$ and the axial wavelength is greater than $10\mu m$.

SF surface variation confine WGM As was mentioned in chapter 2, nano-scale radius variations along SF can be fabricated with CO_2 laser annealing technique; light has been shown to be confined and reflected by such small variations In SNAP, because the WGM have very small propagation constant, therefore is sensitive to dramatically small nano-scale variation of the fibre radius and similar variation of the refractive index. The effective radius variation of a SF and all of the transmission amplitude parameters can be accurately determined from the experiment. "The performance of SNAP devices depends only on the effective radius variation of SF, which includes variations of physical radius and refractive index. For nano-scale variations, these variation usually have the same order of magnitude. This enables fabrication of complex SNAP circuits (consisting, e.g., of long series of coupled micro-resonators) with record high accuracy and record small optical losses.

4.2 Experimental Procedure

4.2.1 Experimental Setup and Alignment Procedure

The three schematic flow-charts that follows intends to illustrate the experimental setup and alignment procedures for the processes of MF/SF coupling, SF alignment and Single MF step-wise scanning respectively.

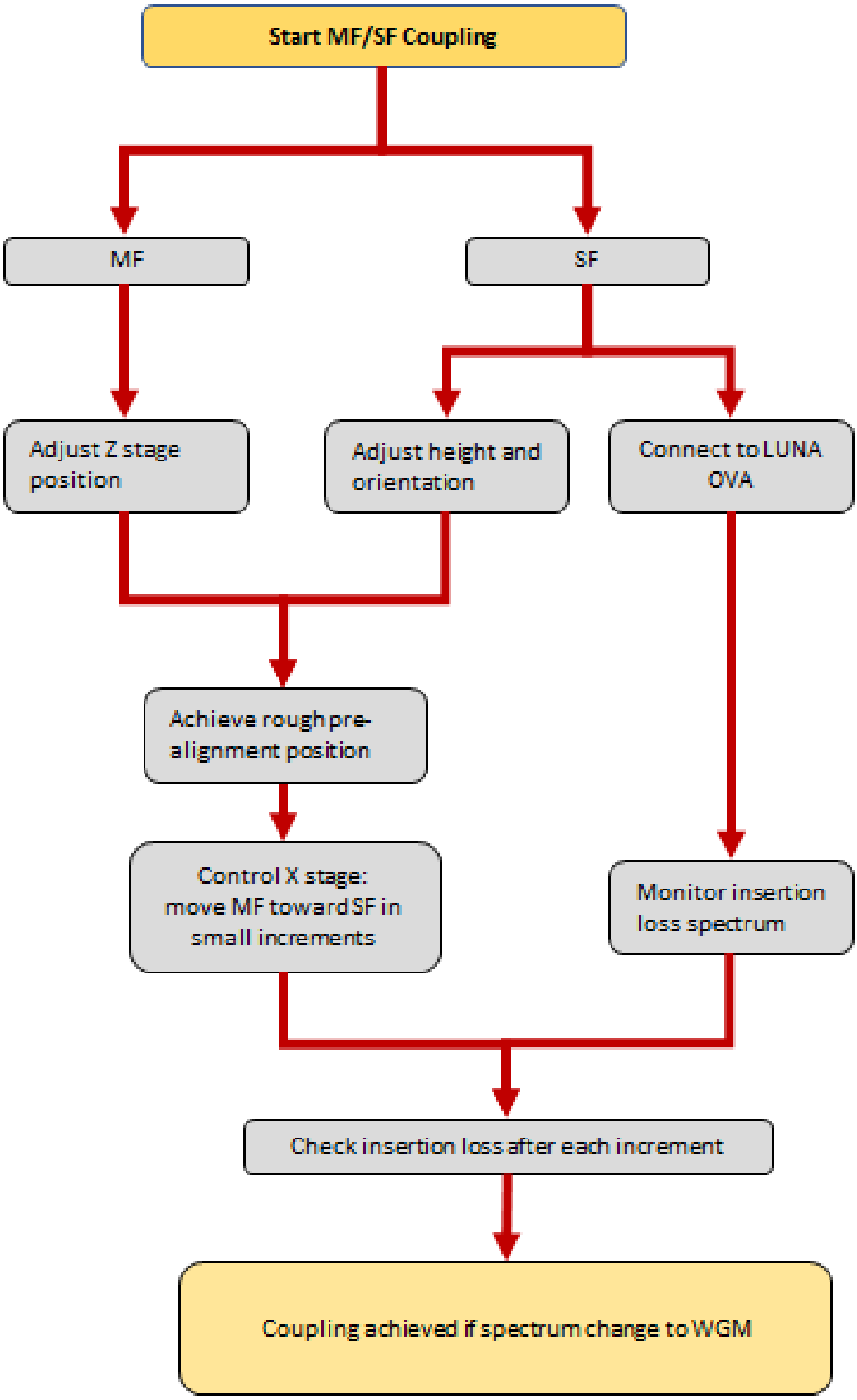

Figure 4.2: MF/SF Coupling

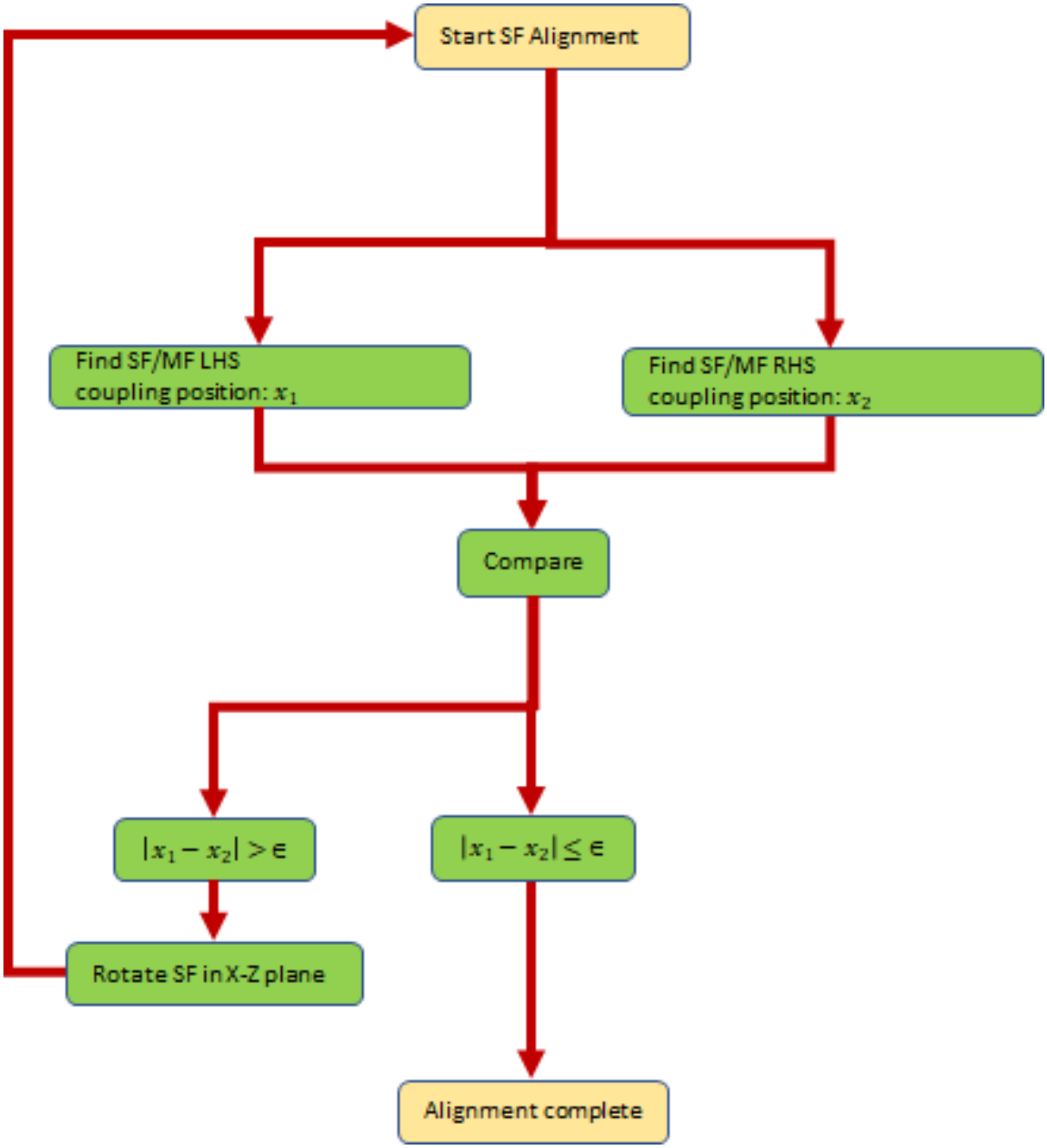

Figure 4.3: SF Alignment

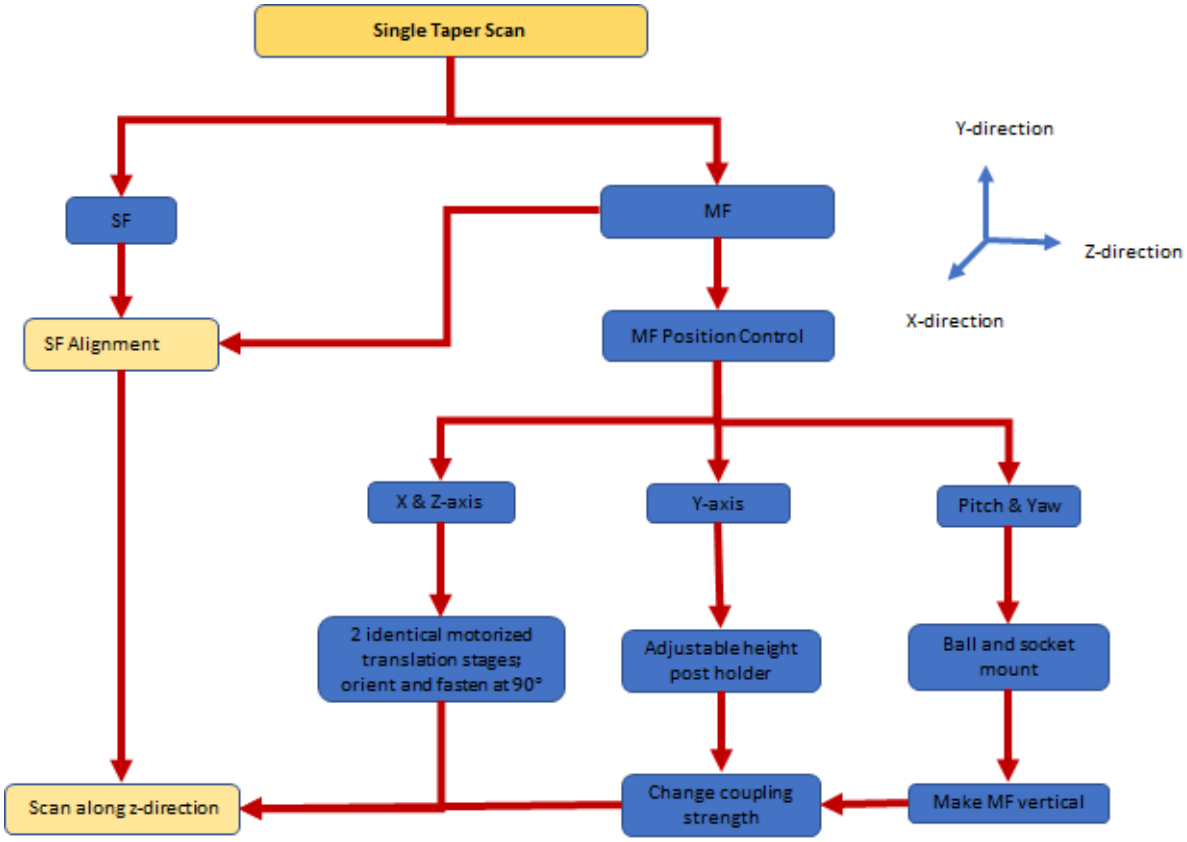

Figure 4.4: 1MFScan

4.3 Experimental Data Analysis for Single Microfiber Coupling

Based on the theory shown in section 2.3, the data obtained from single and double SNAP resonator experiments will be presented in this section. These results are compared with theoretical models based on the formulation of the bare Greens function construction method.

4.3.1 Single well SNAP resonator Data Analysis

As indicated by the solution of time-independent Schrödinger equation, the potential $V(z)$ represent shape of potential well. For one single SNAP cavity, the potential function in the experiment has a Gaussian profile shape, $V(z) = A * exp[-((z-z_0)/\zeta)^2]$, here the parameter A determines the height of the well, parameter ζ determines the width and z_0 the central axial position corresponds to maximum height. The Gaussian shape of the cavity profile is caused by the intensity distribution of the CO_2 laser beam focus by the off-axis parabolic mirror; the parabolic mirror focus light to a narrow elongated region with the strongest intensity at the centre of the beam focus. Provided there is enough frozen-in tension inside the SNAP fiber, without the effect of overheating, the effective radius variation is proportional to light intensity.

The data set is collected by the experimental procedure reported in Subsection 3.2. The number of data points correspond to the number of scans taken at regular interval steps along the SNAP fiber, thus more data points collected over a fix distance range will yield better data plots with higher 'resolution'. Fig. 4.5 below shows the surface plot for 50 measurements along a SNAP fiber.

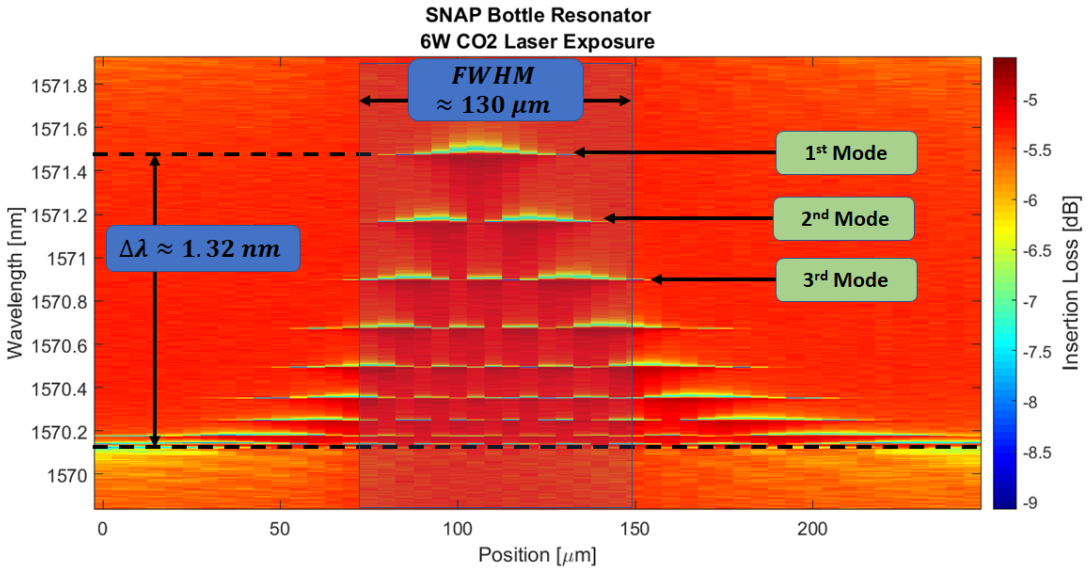

Figure 4.5: SNAP Resonator with 9 Axial Modes

The complete wavelength range for the scan is between $1568.3nm \longleftrightarrow 1573.7nm$. In this wavelength range The axial dimension of a SNAP bottle resonator $\approx 200\mu m$ which requires at least 50 measurements since the step size of the translation stage was set to $5\mu m$. The effective radius variation of the SNAP resonator shown the Fig. 4.5 has an effective radius variation deduced from the formula:

$$\Delta R = \frac{\Delta\lambda}{\lambda_0} \cdot R_0 \approx \frac{1.32nm}{1571.5nm} \cdot 40\mu m \approx 33.6nm \tag{4.26}$$

The transmission amplitude through a single microfiber in the case of lossy coupling is given in the SNAP theory section in terms of the Fano formula: Equation 4.10 . From this equation: $E \propto \lambda$, $\Gamma_n \propto |C_1|^2$, $\Delta_n \propto -Re(D_1)$ and $\Sigma_n \propto Im(D_1)$ The energy E is proportional to wavelength because of equation 2.5. Therefore without the loss of generality it is sufficient to just use:

- Wavelength λ to model the energy;
- Coupling strength C_1 to model the amount of light coupled in to SNAP cavity;
- Phase shift $Re(D_1)$ to change the positions of local resonance peaks;
- Coupling loss $Im(D_1)$ to model the transmission loss.

$$S_{11}(\lambda) \propto S_{11}^{(0)} - \frac{i|C_1|^2}{(\lambda - \lambda_{res} + Re(D_1)) + i(\Gamma_0 + (D_1))} \tag{4.27}$$

Next, the transmission amplitude at a given coupling position, $z = z'$ is modelled by the following 4 parameters, namely: **Fitting parameters for SNAP bottle resonator:** $|C_1|^2 = 0.073$ $Im(D_1) = 0.0602$ $Re(S_{11}^{(0)}) = 0.8856$ $Im(S_{11}^{(0)}) = -0.4021$

The fitting results are plotted the the Fig. 4.6 below:

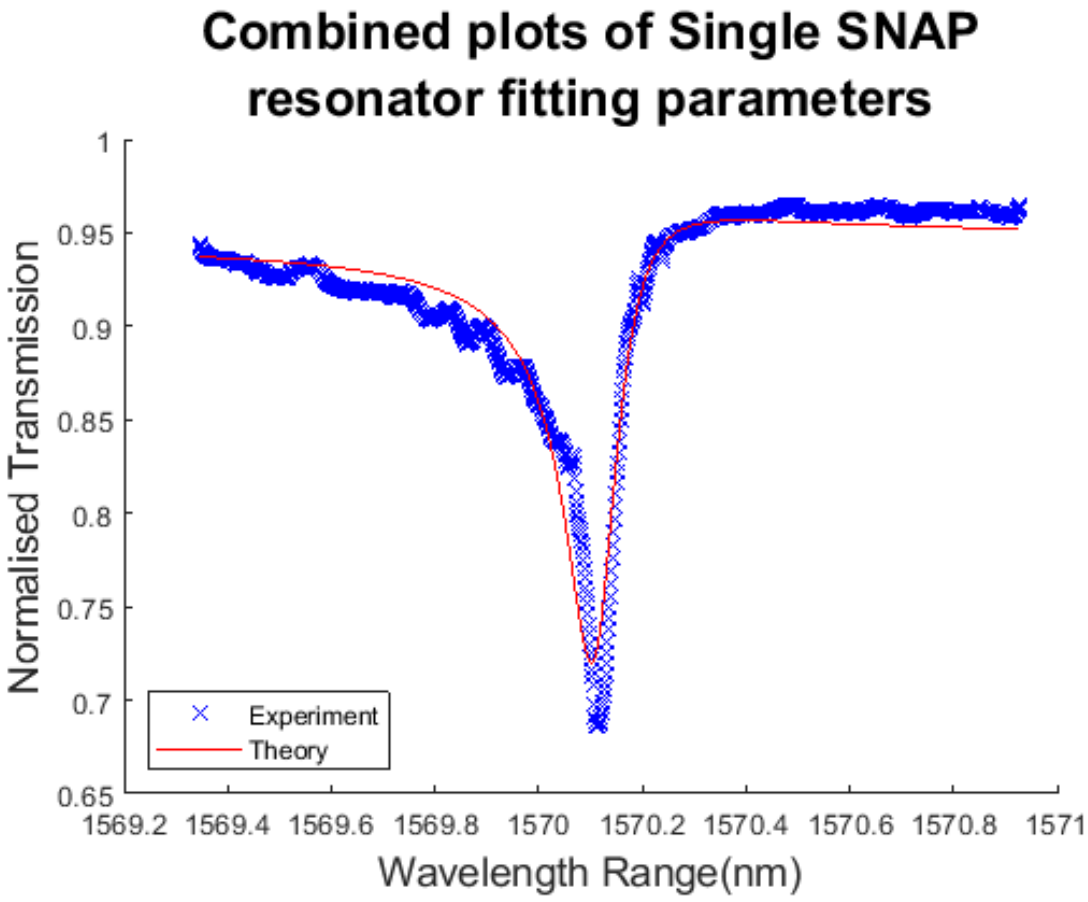

Figure 4.6: Parametric Fitting for SNAP Bottle Resonator

The surface plot obtained from experimental data for single microfiber scan along the axial direction of a SNAP fiber is shown in Fig. 4.7 below:

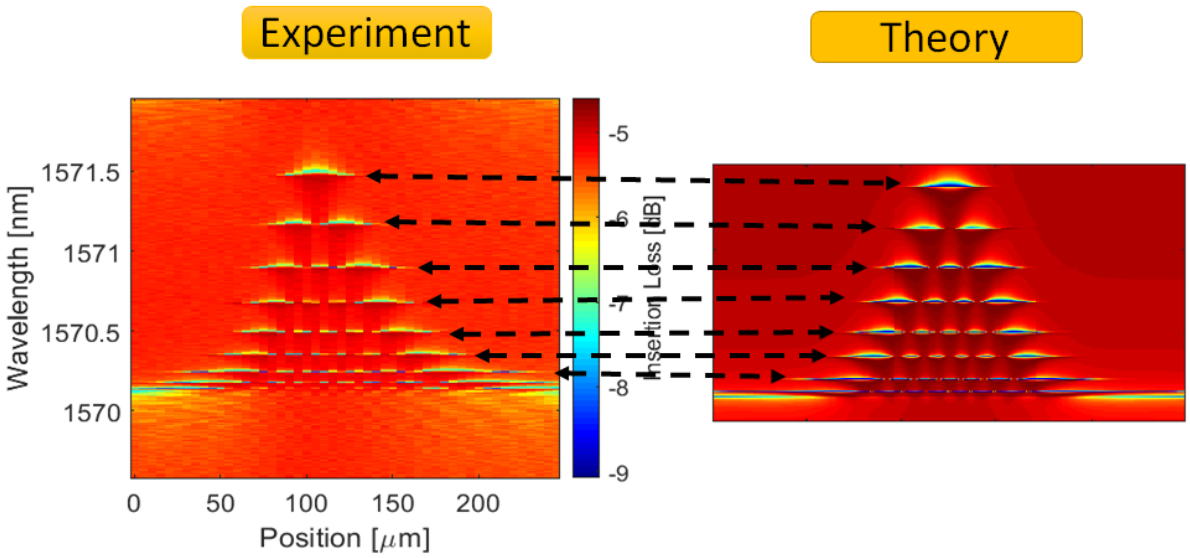

Figure 4.7: Comparison between experiment and theory for SNAP Bottle Resonator

The y-axis is the transmission amplitude $|S_{11}(\lambda)|$ for wavelength deviation. The x-axis is the distance along the fiber. Wavelength deviation for $\lambda_{res} = 1.5\mu m$, $\gamma_{res} = 0.1pm$, and $n_{f_0} = 1.5$. The axial

FWHM of the mode is $20\mu m$, which corresponds to z. It is seen that the resonance width becomes larger near the WGM maxima. For relatively small coupling, the surface plot has a single maximum. For larger coupling, the spatial behaviour of the transmission amplitude splits into two peaks indicating the condition of critical coupling.

4.3.2 Double well SNAP resonator Data Analysis

Fitting parameters for double well resonator: $|C_1|^2 = 0.0047$ $Im(D_1) = 0.0389$ $Re(S_{11}^{(0)}) = 0.8815$ $Im(S_{11}^{(0)}) = -0.3247$

The fitting results are plotted in Fig. 4.8 below:

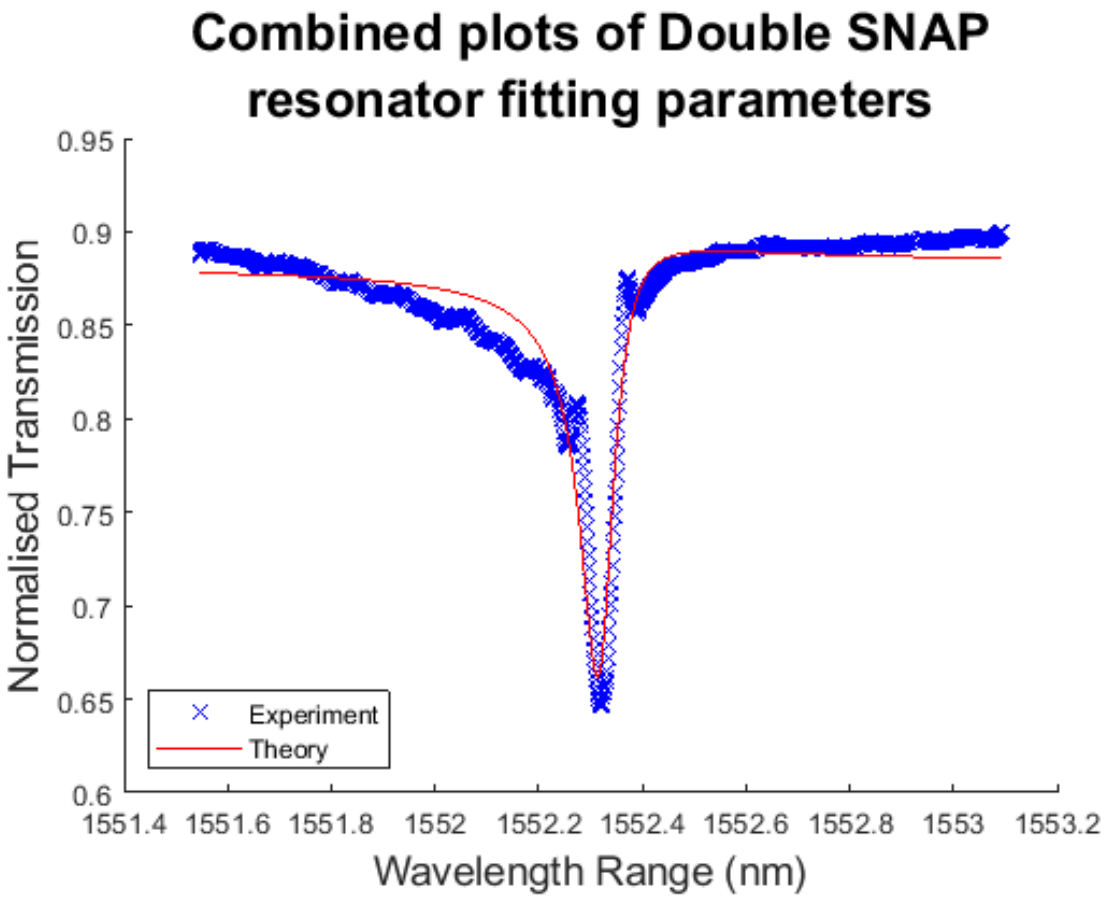

Figure 4.8: Parametric Fitting for Symmetric SNAP Double Well Resonator

The surface plot obtained from experimental data for single microfiber scan along the axial direction of a SNAP fiber is shown in Fig. 4.9 below:

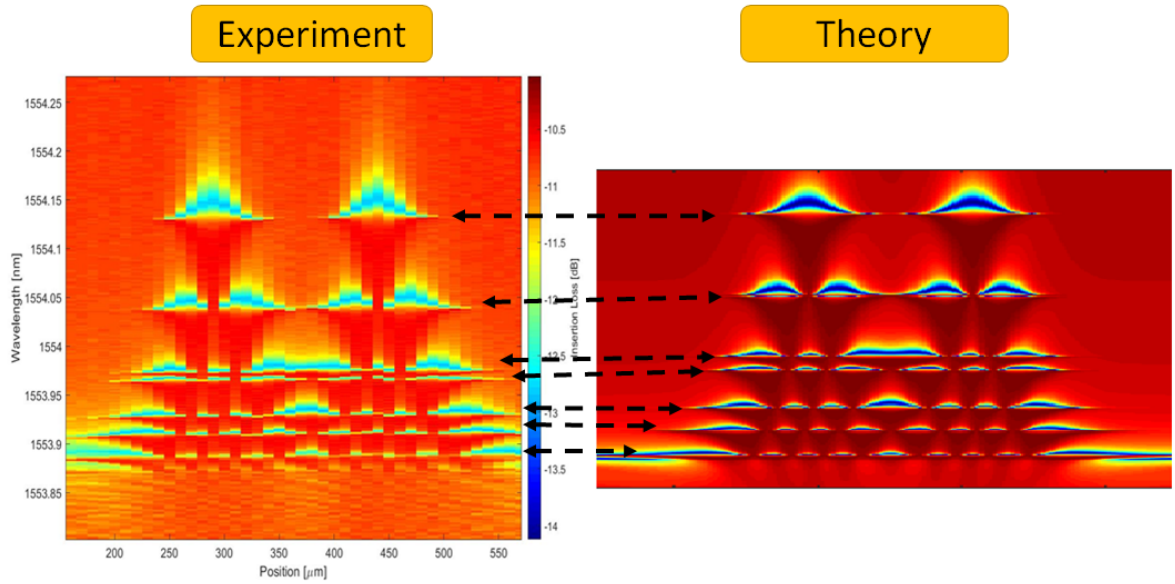

Figure 4.9: Comparison between experiment and theory for Symmetric SNAP Double Well Resonator

4.4 Summary and Perspective

The following viewpoints and remarks can be made from the analysis previous section's experimental results:

- Firstly, the 1-D Schrödinger equation indeed governs the slow propagation of WGM along SF with nano-scale radius variation, the development this theory which can be directly applied both to modelling of SNAP devices and evaluation of experimental data. The energy is proportional to the variation of radiation wavelength λ and the potential is proportional to the joint contribution of fibre radius variation and refractive index variation. Due to the rotational symmetry and ultra smooth surface of SF, the formulation of mode volume can be simply determined by the radius of WGM.
- Secondly, the theory of SNAP devices developed is applied to the analysis of transmission amplitudes: The transmission spectrum obtained from experiment can be fitted accurately with theoretical approximation of eigenmode positions and interval between distribution of axial SF modes, the error between the experimental and fitted calibration of resonant wavelength is due to the assumption of Gaussian shape in the least squares fitting procedure. The transmission amplitude of a SNAP device was expressed through the Green's function of the Schrödinger equation, which is renormalized to take into account the losses due to coupling to WG. The developed theory is applied to the investigation of transmission amplitudes through a localized state and also through a uniform SF coupled to one WG. In addition, theoretical results of lossless resonant coupling is useful when comparing experimental results in the case of weak or contactless coupling.
- And lastly, the relation between the transmission amplitudes through the WGs and the Green's function of the isolated cavity have been identified. The renormalized Green's function of the cavity was introduced. This function modifies the Green's function of the isolated cavity (i.e., the cavity uncoupled from the WGs) called the bare Green's function, and takes into account the losses due to coupling to the WGs. It was found that the transmission amplitudes through the WG can be expressed through the overlap integrals between the renormalized Green's function and the travelling waves propagating along the WG. Excellent agreement between the theory and the experiment is demonstrated.

Chapter 5

Transmission spectrum of SNAPs with two input/output configuration

This work offers a new experimental method for measuring transmission spectrum, which simultaneously uses two microfibers. The said new method, requires two essential optical devices, namely: microfiber and SNAP fiber. In the following pages, I will highlight the functions of microfiber and SNAP fiber only from the specific perspective of experimental system.

5.1 Theory for two input/output taper coupling

5.1.1 The 1D Schrödinger Equation for two coupling waveguides to SNAPs

According to SNAP device theory, if two microfibers, MF_1 and MF_2, are simultaneously coupled to a SNAP fiber. MF_1 is connected to a broad bandwidth light source, it is used as input/output waveguide; and the second microfiber is connected to a photodetector, it is used as sensor fiber; then near λ_{res}: In the instance of two microfibers, the transmission amplitude from the input microfiber MF_1 to output microfiber MF_2 is given by the equation:

$$S_{12}(\lambda) = S_{12}^{(0)} - iC_1C_2^*\overline{G}(\lambda, z, z') \tag{5.1}$$

Here C_1 and C_2 are the coupling parameters for input / output tapers respectively. $S_{12}^{(0)}$ is the non-resonant components of the transmission amplitudes S_{12}. In the vicinity of the resonance wavelengths λ_{res}, the above parameters can take constant values because they are slow functions of wavelength.

For two microfibers, if the Green's function, $G(\lambda, z, z')$, is the particular solution to the inhomogeneous time independent Schrödinger equation:

$$\frac{d^2G(z,z')}{dz^2} + \beta^2 G(z,z') = \delta(z-z') \tag{5.2}$$

Then the renormalised Green's function satisfies the equation:

$$\frac{d^2\overline{G}(z,z')}{dz^2} + \left[\beta^2(\lambda,z) + D_1\delta(z-z_1) + D_2\delta(z-z_2)\right]\overline{G}(z,z') = \delta(z-z') \tag{5.3}$$

Now the next step is to determine the relationship between the bare Green's function and renormalised Green's function.

5.1.2 Renormalisation of Green's functions for multi-microfiber coupling

From two linearly independent solutions of the time-independent Schrodinger Equation, $\Psi_1(\lambda,z)$ and $\Psi_2(\lambda,z)$, the renormalised Green's function can be written as the linear combination: $K_{1n}\Psi_1(\lambda,z)+K_{2n}\Psi_2(\lambda,z)$.

In the case of a SNAP device with two microfibers, MF_1 and MF_2, the renormalized Green's function can be written in the form:

$$\overline{G}(\lambda,z,z_1)=\begin{cases}[A_1\Psi_1(\lambda,z_1)+A_2\Psi(\lambda,z_1)]\Psi_1(\lambda,z)\Psi_2(\lambda,z_2), & z<z_1\\ [A_1\Psi_1(\lambda,z_1)+A_2\Psi(\lambda,z_1)]\Psi_1(\lambda,z_1)\Psi_2(\lambda,z_2), & z_1<z<z_2\\ [A_1\Psi_1(\lambda,z_1)+A_2\Psi(\lambda,z_1)]\Psi_1(\lambda,z)\Psi_2(\lambda,z_2), & z>z_2\end{cases} \tag{5.4}$$

Normalised Green's function at the coupling positions z_1 and z_2 satisfies the following 4 boundary conditions:

$$\overline{G}(\lambda,z,z_1)|_{z\nearrow z_1}-\overline{G}(\lambda,z,z_1)|_{z\searrow z_1}=0 \tag{5.5}$$

$$\overline{G}(\lambda,z,z_2)|_{z\nearrow z_2}-\overline{G}(\lambda,z,z_2)|_{z\searrow z_2}=0 \tag{5.6}$$

$$\left.\frac{\partial\overline{G}(\lambda,z,z_1)}{\partial z}\right|_{z\nearrow z_1}-\overline{G}(\lambda,z,z_1)|_{z\searrow z_1}=1+iD_1\overline{G}(\lambda,z,z_1) \tag{5.7}$$

$$\left.\frac{\partial\overline{G}(\lambda,z,z_2)}{\partial z}\right|_{z\nearrow z_2}-\overline{G}(\lambda,z,z_2)|_{z\searrow z_2}=iD_2\overline{G}(\lambda,z,z_1) \tag{5.8}$$

Where $z\nearrow z_n$ stands for the left hand side limit at $z=z_n$ and $z\searrow z_n$ the left hand side limit at $z=z_n$. Since MF_1 is the input microfiber, the left hand side of equation 5.7 contains an extra renormalised source amplitude 1 compared with equation5.8 with MF_2. Substitute Eqs. 5.4 into the above four boundary conditions, the two coefficients of A_1 and A_2 are reduced into two linear equations. The final result are:

$$\overline{G}(\lambda,z_1,z_1)=\frac{G(\lambda,z_1,z_1)+D_2\left[G(\lambda,z_1,z_1)G(\lambda,z_2,z_2)-G^2(\lambda,z_1,z_2)\right]}{(1+D_1G(\lambda,z_1,z_1))(1+D_1G(\lambda,z_2,z_2))-D_1D_2G^2(\lambda,z_1,z_2)} \tag{5.9}$$

$$\overline{G}(\lambda,z_1,z_2)=\frac{G(\lambda,z_1,z_2)}{(1+D_1G(\lambda,z_1,z_1))(1+D_1G(\lambda,z_2,z_2))-D_1D_2G^2(\lambda,z_1,z_2)} \tag{5.10}$$

In order to obtain the transmission from MF_1 to MF_2, just substitute the expression $\overline{G}(\lambda,z_1,z_2)$ to 5.1. Here the practical assumption is that the coupling positions for each microfiber: MF_1 and MF_2 are deliberately selected during experiment so the coupling conditions are identical which means that $|C_1|^2=|C_2|^2=|C|^2$ and $D_1=D_2=D$. In the meanwhile, without considering the case where two microfibres are very close to each other; far away from the resonance wavelength, the light from MF_1 cannot be transmitted into MF_2. Therefore, $S_{12}^{(0)}=0$. Under the above assumptions, the transmission is:

$$S_{12}(\lambda)=\frac{-i|C|^2G(\lambda,z_1,z_2)}{(1+DG(\lambda,z_1,z_1))(1+DG(\lambda,z_2,z_2))-D^2G^2(\lambda,z_1,z_2)} \tag{5.11}$$

5.2 Experimental Procedure

5.2.1 The experimental setup of two microfibers coupled with SNAPs

The experimental schematic setup involving one SNAP fiber and two microfibers is illustrated in Fig. 5.4. The whole experiment is carried under an automatic process controlled with AUTO HOTKEY script; where the movement is controlled by 3D stages.

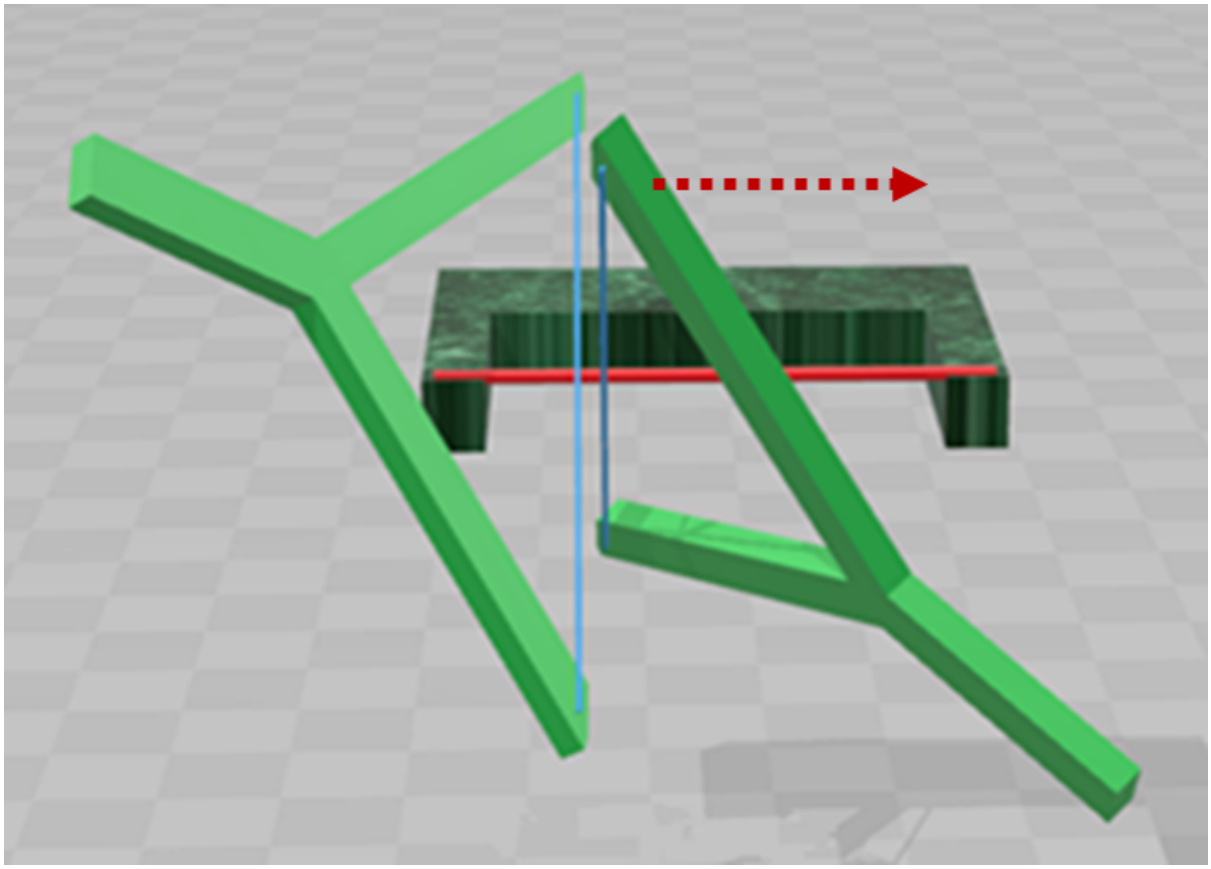

Figure 5.1: Two Microfibers Setup

The MF/MF angle is 90° and the MF/SF angle is 45°.

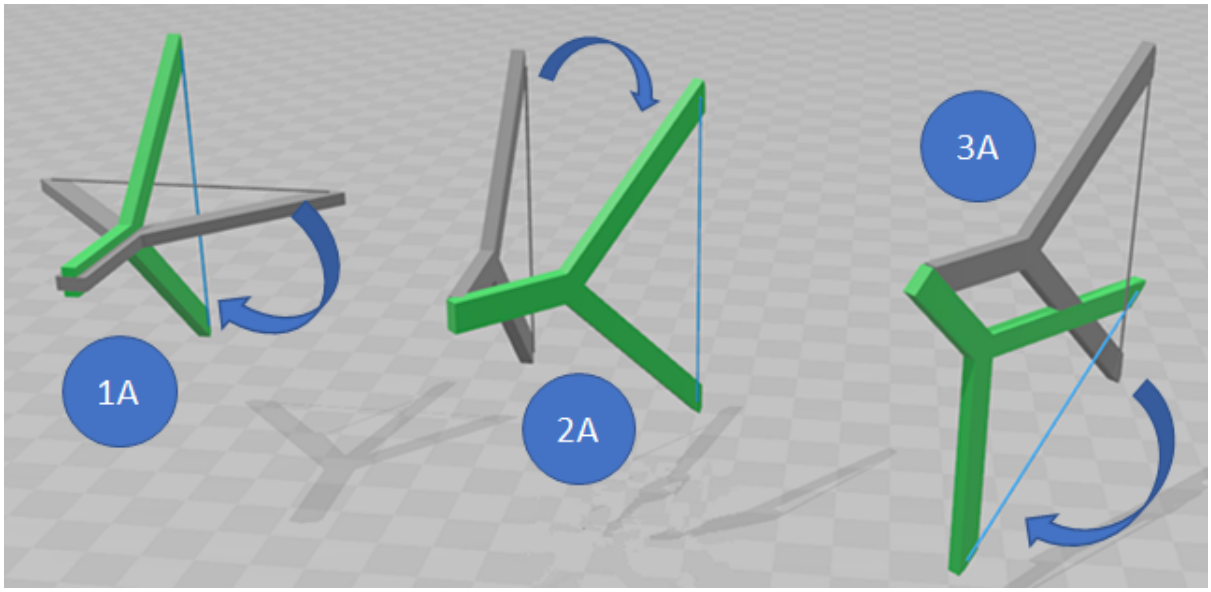

Figure 5.2: Left-hand-side microfiber orientation

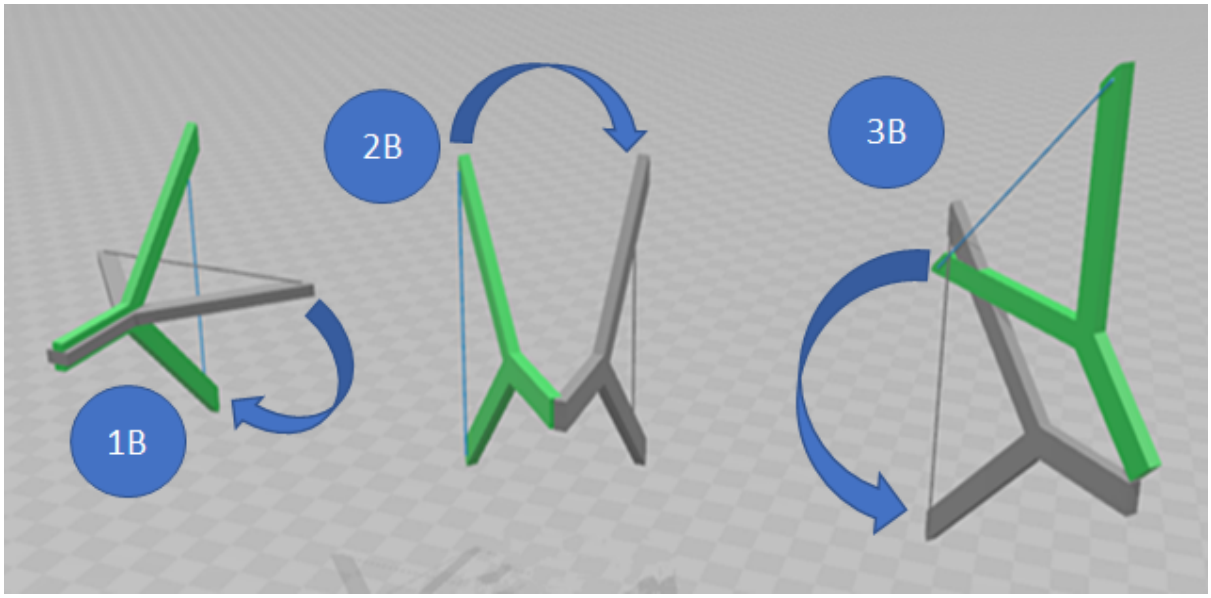

Figure 5.3: Right-hand-side microfiber orientation

Two Microfiber Measurement Procedure

The procedure for making measurement with two microfibers is show in Fig. 5.4.

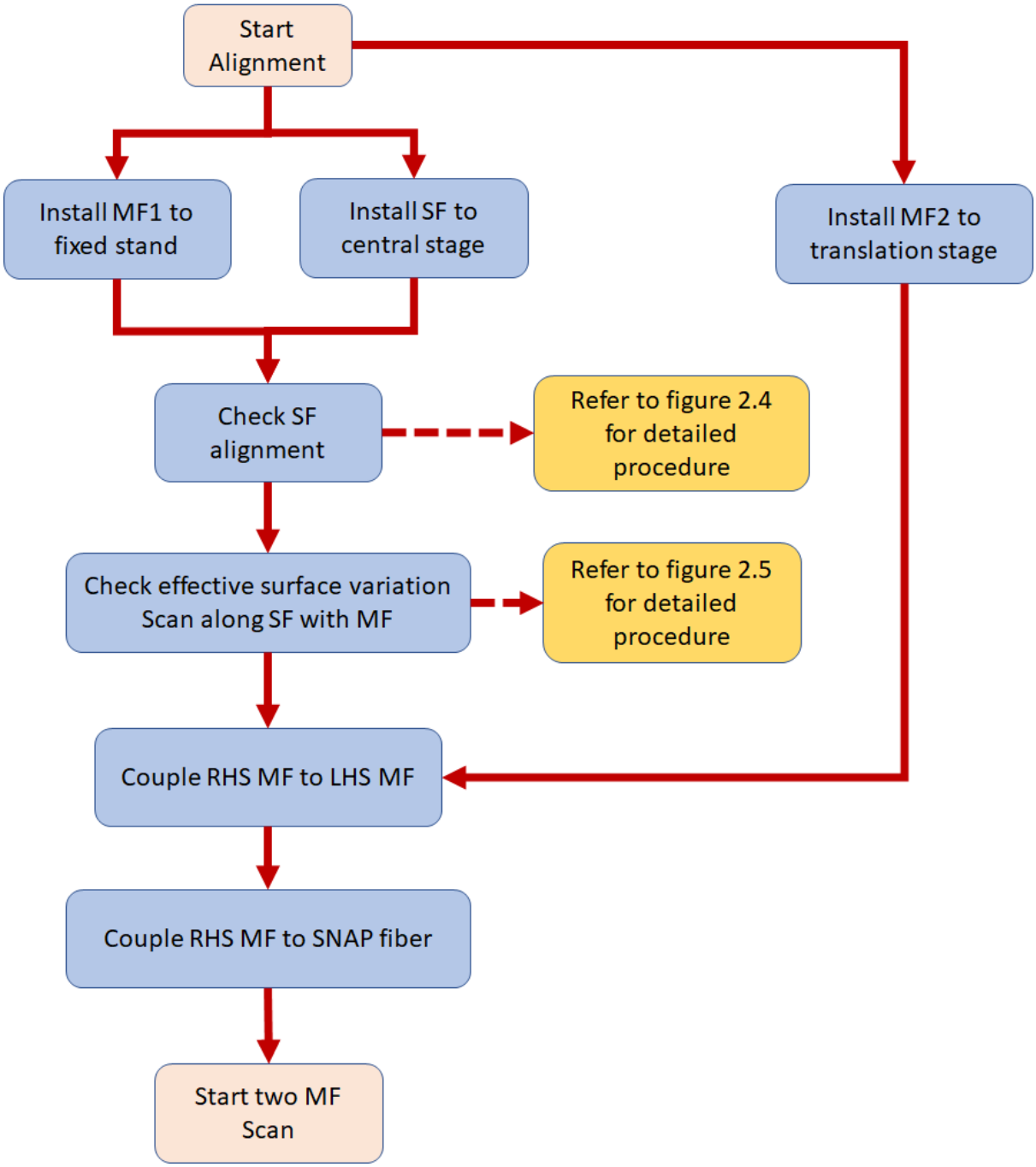

Figure 5.4: Measurement procedure for measurement with two microfibers

5.3 Data analysis for two input/output Microfibers

First, when collecting data from LUNA©OVA 5000, full amplitudes and phases of the four Jones Matrix elements were recorded for different position between two tapers. Then the insertion loss is calculated as $IL = 10 \cdot log_{10}((|a_i|^2 + |b_i|^2 + |c_i|^2 + |d_i|^2)/2)$, where i indicates the index location in the data array, and corresponds to wavelength. In practice, a Matlab script is written for automatically reading, calculating and plotting the S_{12} measurement in terms of IL.

In the following pages, the experimental results for single and double SNAP bottle resonators are compared with SNAP simulation using a modified Matlab code similar to Chapter 4.

5.3.1 SNAP Bottle Resonator measurements

Fig. 5.5 and 5.6 shows the surface plot of S_{12} measurements along a single SNAP bottle resonator at two different excitation positions A and B:

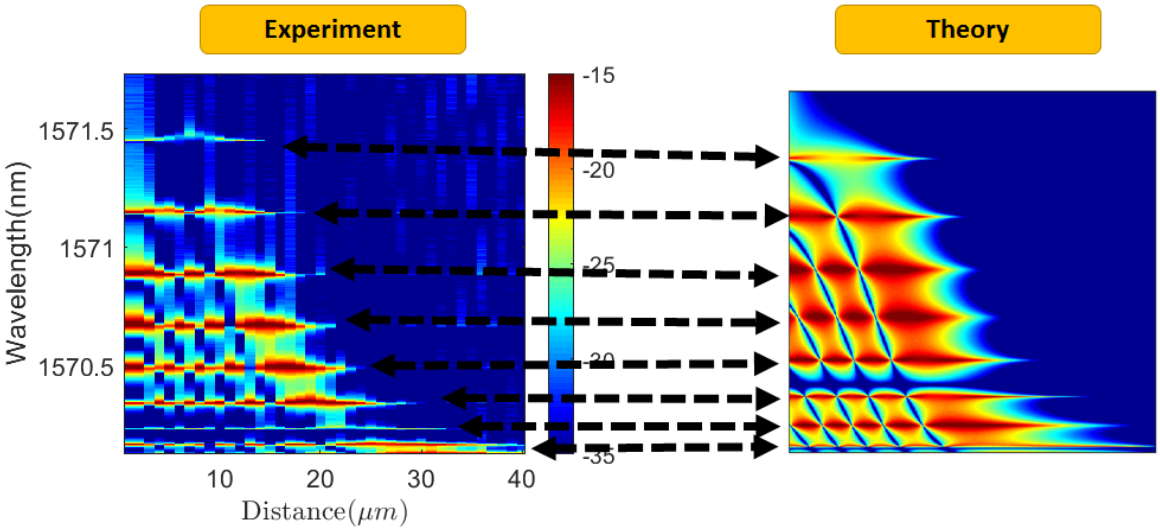

Figure 5.5: Comparison between experiment and theory: S_{12} for SNAP Bottle Resonator at coupling position A

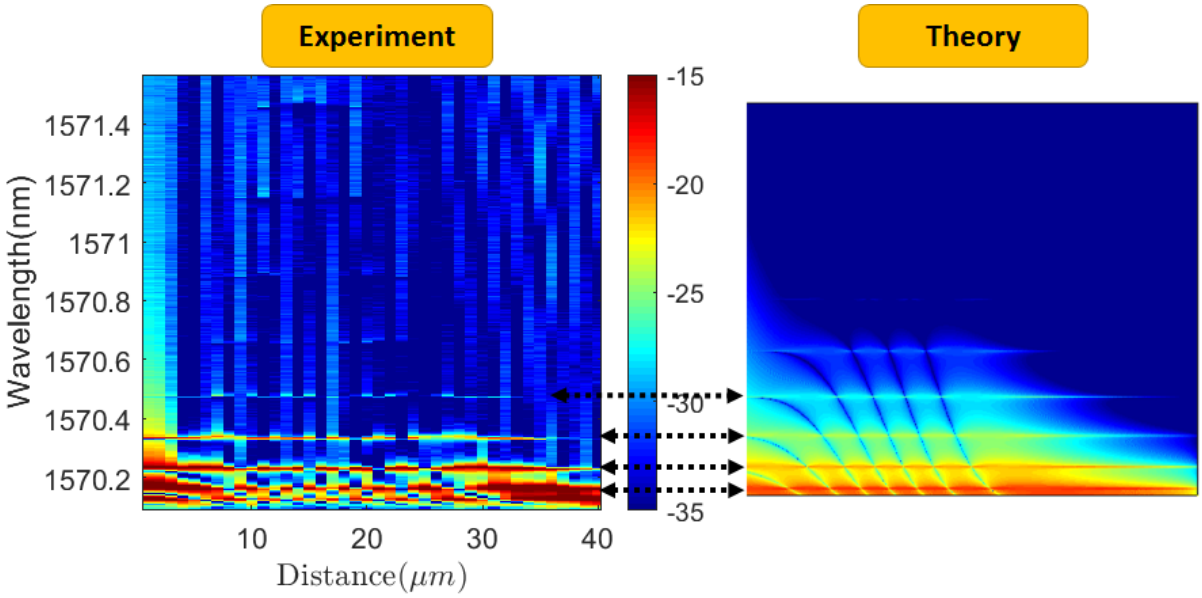

Figure 5.6: Comparison between experiment and theory: S_{12} for SNAP Bottle Resonator at coupling position B

5.3.2 Symmetric SNAP Double Well Resonator Measurements

Fig. 5.7 and 5.8 shows the surface plot of S_{12} measurements along symmetric SNAP double well resonator at two different excitation positions A and B:

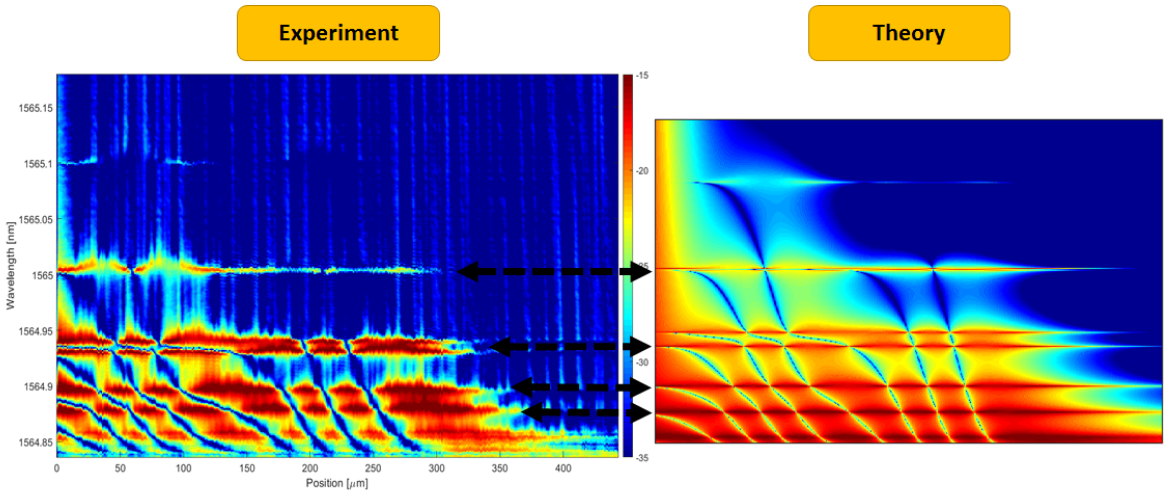

Figure 5.7: Comparison between experiment and theory: S_{12} for Symmetric SNAP Double Well Resonator at coupling position A

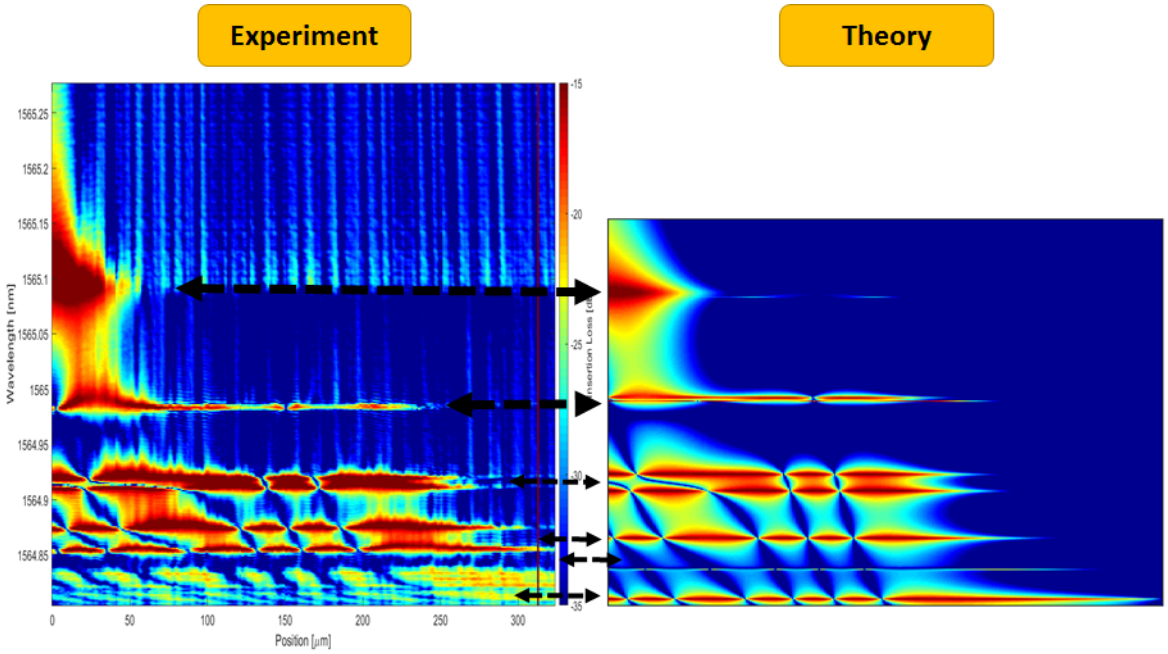

Figure 5.8: Comparison between experiment and theory: S_{12} for Symmetric SNAP Double Well Resonator at coupling position B

5.4 Discussion and Perspective

5.4.1 Attributes of two MF Measurements

The coupling from one tapered fiber to another via SNAP fiber depends on the Energy of the incident probing light. Especially when there are two spatially separated Gaussian-like SNAP cavities, the light with higher axial number couples better than the lower ones. There are some discrepancy between theory and experiment because the S_{12} measurements tends to have higher insertion loss than S_{11} measurements, The experimental data was obtained with two microfibers. The first microfiber, MF_1 is used as the input fiber and the second one, MF_2 as the output fiber. This means the light source from LUNA OVA is coupled into the SNAP cavity by MF_1 and the WGM light with wavelengths which satisfies the resonance boundary condition is coupled and confined between turning points at the boundary of SNAP resonator, give rise to the modes seen in the surface plots. Both MF_1 and MF_2 had the same axial initial position, $z_1 = 0\ \mu m$ and $z_2 = 0\ \mu m$ respectively. Subsequently, the position of MF_1 stay fixed while the position of MF_2 changes by $1\mu m$ steps, so that the separation distance increases after each step n, $d_n = |z_1 - z_2|_n = n\ \mu m$.

In addition, The effective radius variation for the SNAP bottle resonator is calculated as:

$$\Delta R = \frac{\Delta\lambda}{\lambda_0} \cdot R_0 \tag{5.12}$$

$$\approx \frac{1.3nm}{1570.2nm} \cdot 20\mu m \tag{5.13}$$

$$\approx 16.5nm \tag{5.14}$$

5.4.2 Cleanness SNAP Fiber

As shown in Fig. 5.9, dust particles are prone to attach onto the surface of SNAP fiber due to the Van Der Waals force.

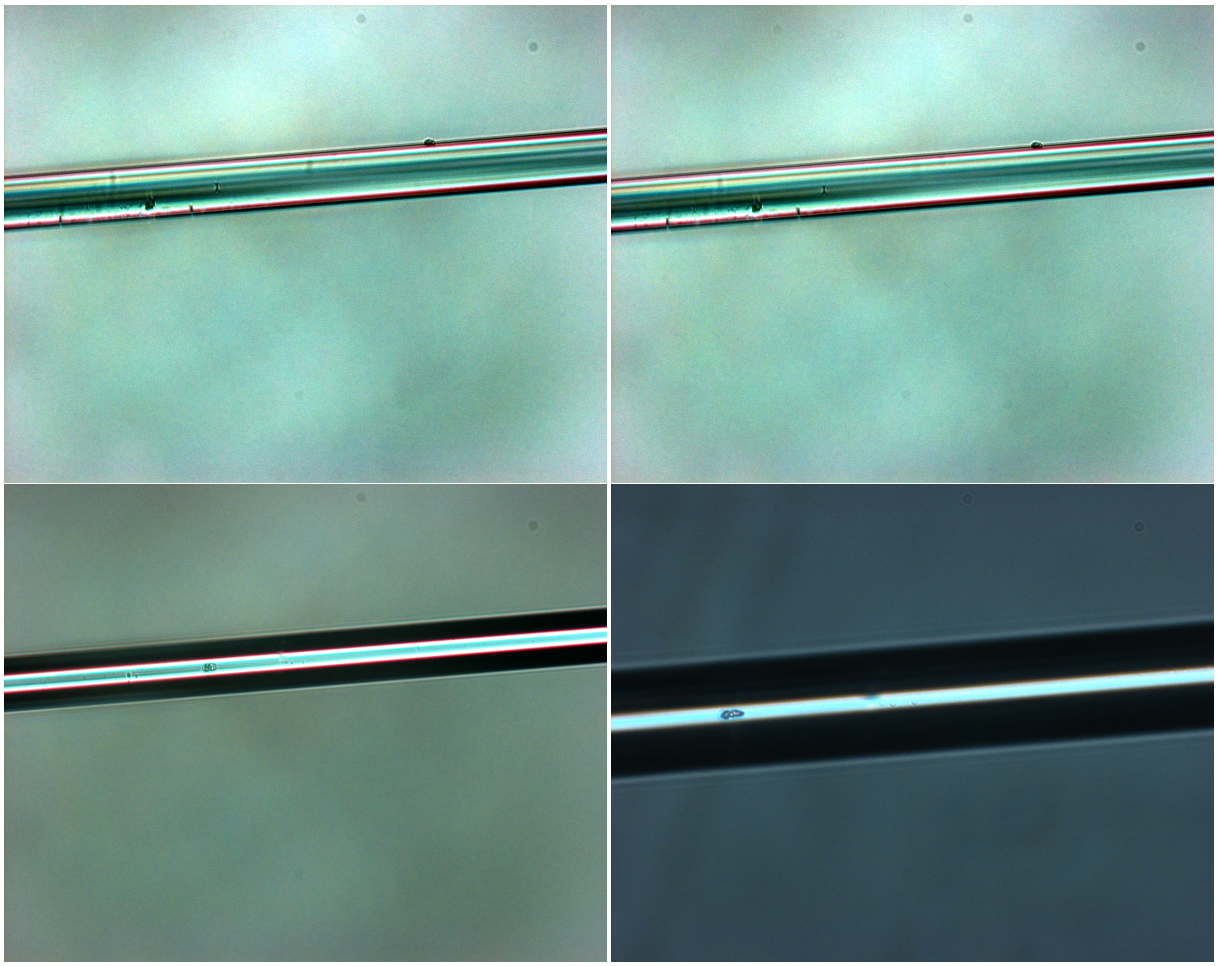

Figure 5.9: Magnified photos of SNAP fiber removed from storage containers for 3 hours

Therefore it is very important to carry out measurements in a dust free environment. For these fibers an additional post-processing step of CO_2 laser brushing is needed to burn-off the attached particles. The laser power and brushing speed used for the post-processing step is $2.5W\ (10\%)$ and $0.5mm/s$.

Chapter 6

Conclusions and Plans for Future Research

This study was undertaken to design and fabricate for the first time: a two microfibers, input (excitation) and output (detection) experimental system; The system is applied to demonstrate device characterizations for SNAP technology system. Chapters 1 through to Chapter 4 established the theoretical foundation and experimental techniques required in SNAP theory. Preliminary results of two microfiber transmission measurements S_{12} were reported in Chapter 5.

This Chapter is divided into 2 main sections, the first section starts by addressing the results reported in chapter 5; make conclusions regarding the feasibility and reliability of the experimental system; In the second section, I will present a theoretical framework by which SNAP tunneling time can be adequately defined and therefore the possible continuation suggestions regarding future work is put into perspective.

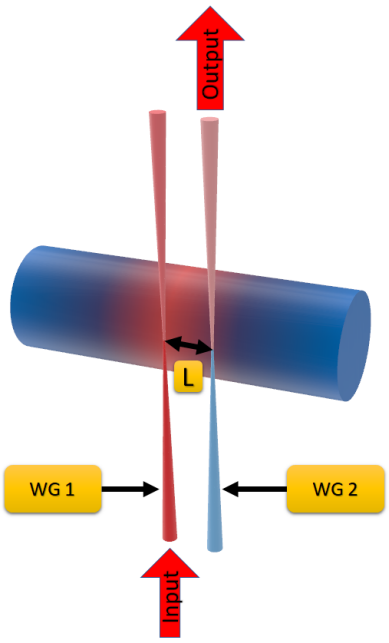

Figure 6.1: Two Microfiber Experimental System

6.1 Conclusions

This study has found that general tunneling phenomena were observed using the two microfiber system is shown in Fig. 6.1, for both cases of SNAP uniform and symmetric double well resonators. As seen previously, the visualization and analysis of experimental results were achieved from the conceptual framework of SNAP theory and plotted by 2D spectrograms. The amplitude of these spectrograms corresponds to S_{12} transmission derived from expressions of bare Green's function, which are dependent on numerical approximations of SNAP cavity boundary conditions. In particular, the bare Green's function for uniform SNAP fiber has been expressed as:

$$G(\lambda, z, z') = \frac{exp\left[i(E(\lambda) - E_0 + i\Gamma_0)^{1/2}|z - z'|\right]}{2i(E(\lambda) - E_0 + i\Gamma_0)^{1/2}} \quad (6.1)$$

The key SNAP tunneling results are summarised below:

Transmission for uniform SNAP fiber

In the experimental demonstration for uniform SNAP fiber, a large number of samples was fabricated because of the difficulty encountered in obtaining SNAP fiber with the required surface uniformity to manifest free propagation modes.

Attempts with an ad hoc low-power laser brushing process have proven to be effective in the elimination of mode vocalizations.

Fig. 6.2 shows the S_{12} transmission surface plot for a uniform SNAP fiber sample:

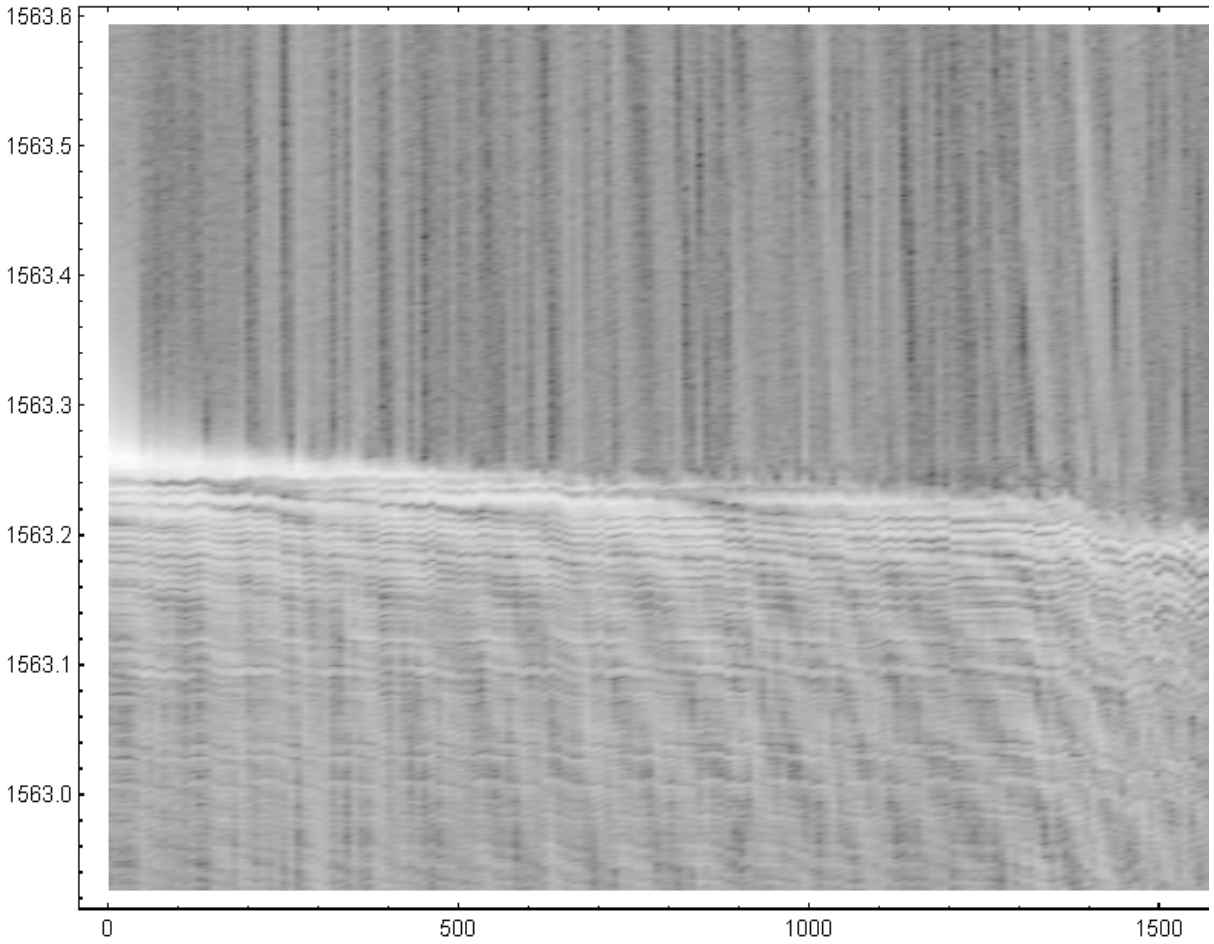

Figure 6.2: Surface Plot of S_{12} for Uniform SNAP fiber

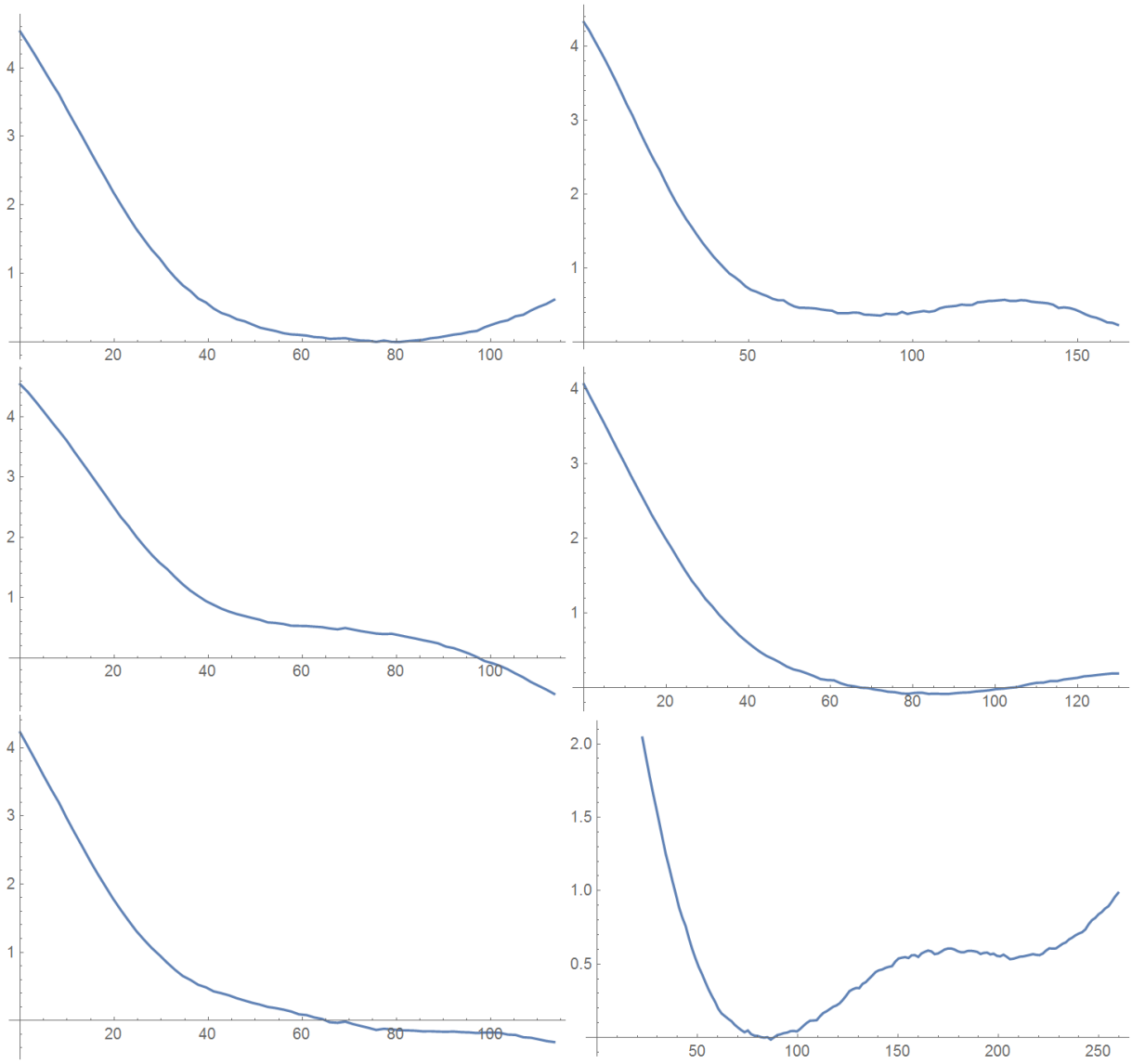

Figure 6.3: Exponential Decay Curves for different uniform SNAP samples

For 6 different USF samples, the S_{12} transmission amplitude along fixed frequencies just below cut-off frequency was taken from the surface plots and plotted in Fig. 6.3, the general trend of exponential decay in uniform SNAP fibers can be clearly seen:

The numerical optimization tailored for the exact determination of tunnelling time information from data is encountered experimental difficulty of deep cracks and background noise, however a promising solution have been found; the experimental realization is expected in the immediate future.

6.1.1 Symmetric SNAP Double Well Tunnelling

In the case of symmetric SNAP double Well resonator, the resonant tunneling behaviour was observed: i.e. using the two microfibers measurement technique, the WGM eigenmodes coupled inside first resonator can also be observed inside its adjacent closely separated resonator. As the resonators have very small difference in height, the quantum behaviour of energy level splitting was also observed. The horizontal axis shows the distance along SNAP fiber The vertical axis shows wavelengths One microfiber stays fixed, the other moves in small steps along SNAP fiber. Demonstrated the quantum mechanical phenomena. The bright features on the plots are resonant wavelength of the cavities.

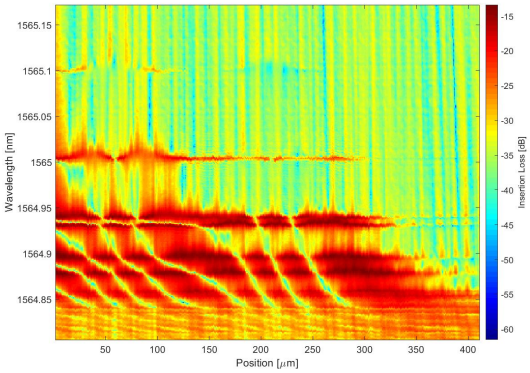

Figure 6.4: Energy Levels Splitting

Light with appropriate close to resonance wavelength producing these beautiful localization modes. There is an very interesting connection between SNAP system and quantum mechanics, i.e. the quantization of energy levels and the observed interesting phenomenon of energy level splitting, which also occurs in resonant tunneling. It is a topic ongoing research.

6.1.2 Deep cracks, discovery of large rectangular resonators

In order to ensure the accuracy and reliability of my results, Efforts have been made to carefully control some important factors of SNAP fiber and microfibers. Figure 6.5 on the right hand side is spectrogram surface plot of the wavelength spectrum for uniform SNAP fiber at 0.64nm resolution. Sharp discontinuities have been observed on the plot; these cracks appears to have random spacings, with the largest over 1500nm wide, they corresponds to dramatic decrease in effective radius. Light is reflected strongly at the cracks, therefore the WGMs is observed due to strong confinement of light between each crack and its adjacent ones. One possible cause of these cracks is natural fiber quality degradation due to prolonged ageing and moisture attack.

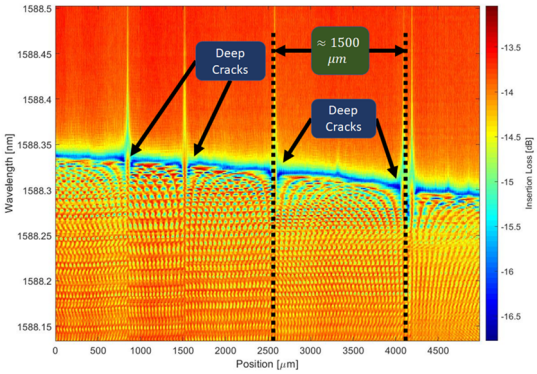

Figure 6.5: Deep Cracks

Another possible explanation is that particles are prone to stuck onto the surface of microfibers and SNAP fibers after taken outside storage container. Microfiber flame torch brushing and SNAP fiber low-power laser brushing are active control measures to counteract this effect. The passive control measure involves reducing the amount of time from once taken from storage container to the end of data collection.

6.2 Plans for Future Research

The purpose of this section is to establish a concise yet self-contained theoretical framework for a novel quantum tunneling experiment with 'a miniature dimension, ultra-low loss, sub-angstrom precision photonic platform'[88, 94, 96, 97], which can be applied in determine tunneling time in SNAP technological system. To this end, conscious effort was made towards constructing a bird's eye view on the rich and diverse field of tunneling time for comparing governing principles of time concepts and gaining credible basis for author's future research.

6.2.1 Elements of Tunneling Time Experiment for the application of Surface Nanoscale Axial Photonics Theory

Tunneling is considered a purely quantum phenomenon [108], the main challenge for measuring tunneling time is due to the inability to directly observe tunneling inside a potential barrier without collapsing its wave function due to quantum measurement problem [106]. Therefore, common strategy adopted by experimenters involves making indirect 'asymptotic' inferences based on measurements for reflected and transmitted particles at reasonable distances away from potential barrier [36, 113, 20][10] and much historical controversies and debates revolves around the interpretation of tunneling process inside 'classically forbidden' barrier region. [113, 106]. For example, by naively assuming the particle 'propagates' inside the barrier (in a straight path), experimental time delays measurements had been used as arguments for faster-than-light propagation speeds. [86, 85, 46, 5]

It had been demonstrated experimentally that SNAP devices exhibit quantum tunneling behaviour: [89, 94, 98] In practice, evanescent field surrounding the exterior of tapered microfiber (MF) used to excite whispering gallery mode (WGM) acts as the tunneling source in the experiment [8] and MF is fabricated by slowly stretching single mode optical fiber under CO2 laser point heat source [9], creating the following shaped profile:

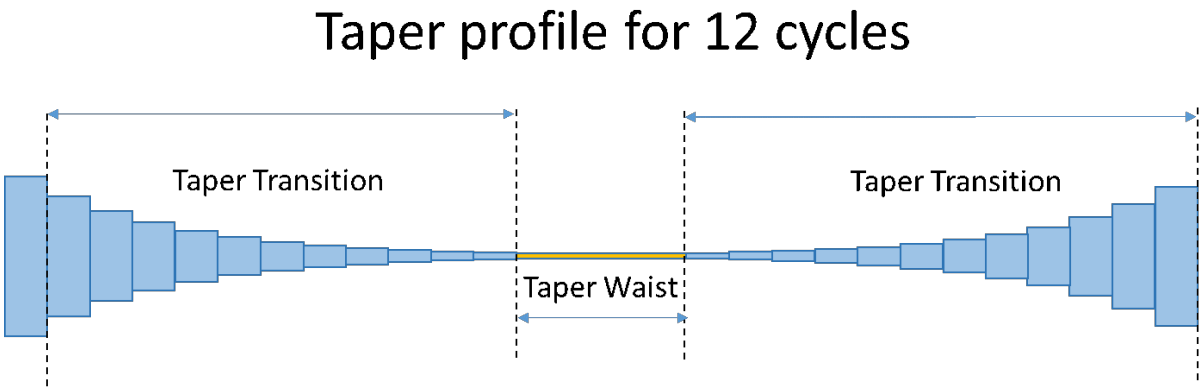

Figure 6.6: Biconical Microfiber

When the frequency of the monochromatic source going through MF is above its cut-off frequencies, WGM then acts as a pseudo-particle that slowly propagates along the axial direction of SNAP fiber (SF). At cut-off frequencies, WGM is halted, which means there is no axial propagation. When the frequency of a monochromatic source is below cut-off: WGM (pseudo-particle) undergoes tunneling with SF as a rectangular barrier. [92, 97, 88] A SF may contain a combination of barriers and wells potentials.[93, 96, 101]

Furthermore, previous quantum experiments performed using SNAP devices have shown excellent agreement with SNAP theory [90, 87, 91], which renders SNAP devices a promising candidate to study tunneling time.

6.2.2 Classic tunneling time experiments

The old and seemingly simple question of the time for a particle to pass through a barrier became a controversial subject The question was addressed by posing the rhetorical question: What does tunneling time mean? [54, 60, 32, 26, 113]

Between 1940s and 1990s, tunneling thought as an innate wave phenomenon was investigated experimentally for waves under a wide range of frequencies. The following table shows a brief summary of 20 classic tunneling time experiments performed in optical, electromagnetic, microwave, radiofrequency, terahertz and acoustic domains [26-28, 52, 66]; [1, 110, 107, 109, 71]

From classical point-of-view, there's little dispute in terms of tunneling time definitions; the main challenge, as Spielmann et al. [85] pointed out, is short tunneling delay and requirement for high precision time measurements, even more so in optical frequency range (OFR). [113, 36, 20, 60]

Indeed, the demanding requirement for measuring short tunneling delays is still proving to be a significant challenge in recent years, particularly in strong-field and attosecond experiments. [41, 43, 18] In comparison, the advantage of my experimental design is the utilisation of slow light based on WGM evanescent tunneling with tapered micro-fiber, for which the axial propagation speed is considerably slower than light speed, thus allows more accurate time measurements than most experiments performed at OFR.[94, 96]

Source / Range	Monochromatic Wave Signal						Polychromatic Pulsed Signal					
	Exp.	λ	V		Time Delay		Exp.	Width	V		Time Delay	
			Type	d	τ_0	τ_g			Type	d	τ_0	τ_g
Optical (100 nm — 1 mm) [41]	[24,25]	3.39 μm	FTIR	2.8 cm	97 ps	67 ps	[19-21]	20 fs	PBG	1.1 μm	3.6 fs	2.13 fs
							[22]	12 fs		0.4 μm	2.4 fs	1.1 fs
							[23]	380 ps		2 cm	97 ps	34 ps
Terahertz (100 μm — 1 mm) [42]	[26,27]	1.5 mm		1000 μm	8.6 ms	7.0 ms	[34-36]	1 ps		200 μm	2.70 ms	0.89 ms
Microwave (0.1 cm — 1m) [43]	[28,29]	1.3 cm		10 cm	333 ps	120 ps	[30,31]	9.1 ns		22.75 cm	384 ps	530 ps
Acoustic (17 mm — 17 m) [44]	-	-		-	-	-	[37,38]	20.5 cm		20 ms	3.01 ms	1.19 ms
Radio (1 mm — 100 km) [45]	-	-		-	-	-	[32,33]	4 μs		120 m	218 ns	150 ns

Table 6.1: Summary of 20 classic tunneling time experiments
[86, 85, 46, 5, 2, 75, 74, 24, 25, 23, 57, 59, 58, 34, 19, 56, 77, 116, 81]

6.2.3 Recent Research Directions and Developments

Before proceeding further, it is necessary for me to state two prerequisite positions by which this section is based: First, there exists an isomorphism between the following one-dimensional, second order differential equations: [60, 85, 113]

Helmholtz equation	Time-independent Schrodinger equation
$\frac{\partial^2\psi}{\partial x^2} + k^2\psi = 0$	$\frac{d^2\psi}{dx^2} + \frac{2m(V-E)}{h^2}\psi = 0$
Evanescent field tunneling [24,25]	Quantum particle tunneling [14,15]

Figure 6.7: Isomorphism between Helmholtz and Schrödinger Equation

Second, to avoid confusions about time in quantum mechanics, Dusch classified such times into three categories: [22, 8, 9, 41]

• External time: measured by external parameters that are not dynamically connected with the quantum-mechanical system; • Intrinsic or dynamical time: defined through some significant dynamical change within a quantum system; • The observable or event time: when measured time have a physical meaning.

Busch classification is adopted to show since had been known to dispel confusions on tunneling time. In the following table, it is used to reveal the relationship between Hauge and Bernardini's definitions: [22, 8, 9, 36]

Dusch / Hauge	External Time	Internal Time	Event time
Phase time	Main intrinsic change	Path contours inside barrier	Periodic oscillation
Dwell time	Time spent inside barrier	Imaginary path integrals	Time-dependent wave packets

Table 6.2: Classification of Tunneling Time

6.2.4 Experimental Progress

Direction and Motivation

Two insights expressed by Hauge and Stovneng are both true for my experiment: Hauge and Støvneng [36]

1. "The main driving motivation in gaining understanding about tunneling time: 'the emergence of techniques for the fabrication of new sensitive, high-speed devices in the nanometre range"; [92, 91]

2. "The best strategy forward: 'turn to tunneling experiments now in progress with the aim of thoroughly understanding the temporal aspects of the individual experiments".[102, 35]

The research directions pursued repeatedly in tunneling time experimental design takes two general themes:

- Classical studies mostly investigate tunneling delay in relation to the potential barrier and keeping the tunneling source unchanged.
  In this category the effective variabilities include: the thickness Steinberg et al. [86], Spielmann et al. [85], Longhi et al. [46], Balcou and Dutriaux [5], shape [19, 40, 48], opaqueness [77, 17, 49], or oscillatory motion Ho [37], Goldberg and Pollack [30], Pereira et al. [70] of barrier potential. These papers have all reported dependence of barrier with tunneling speed.
- On the other hand, there's also experimental evidence of relationship between tunneling delay and properties pertain to the tunneling source, including: initial turn-on time [42, 86, 43] and position [39, 33], incidence angle [78, 83], amplitude [68, 33, 77], spin [47, 47, 118, 45], dual-directional wave-particle and pulse width [113].

Dissipative tunneling

The effect of tunneling dissipation wasn't explicitly mentioned in most tunneling time experiments to date or at best assumed an ideally elastic scattering situation without justification. One exception is a 2017 study which defined tunneling dissipation as energy loss of incident source via velocity dependent frictional force when undergoing tunneling through aluminium oxide barrier.[39] Two general findings were reported in this work: [39]

- More dissipation leads to less dwell time and phase time;
- The percentage of energy loss is higher for smaller energies.

Tunneling dissipation is negligible in our experiment because WGM in optical fiber have high Q-factor.[94, 89]

6.2.5 Current Debates and Challenges

Tunneling interference, Hartman effect and faster-than-light propagation

Although Hartman effect observed in most classic tunneling experiments, in recent years rectangular barrier tunneling delay have shown perplexing dependence for large barrier width under certain situations, a number theories attempted to explain the cause of Hartman effects, for instance:

- Salecker-Wigner-Peres quantum clock; [49, 48]
- Identical Gaussian wave packets incident opposite sides of a square barrier at the same time; [72, 70]
- Absorption or inelastic channels (modelled by complex barrier potential). [69, 40]

Experimental Evidence: The following are used as evidence that Harman effect originate from barrier interference, not exponential decay (evanescent waves in optics): [113, 49, 82]

- The non-zero time of transmitted electron contested the existence of response time and negative tunneling delay in operator theory (sustained momentum space);

- Electron tunneling through atom ionization induced time varying laser field argued that tunneling delay is the response time for wave function distribution to reach asymptotically stable state after initial 'switch-on'.

Despite the mechanism of self-interference was not yet well-understood, the following can be deduced:

- If superluminality is attributed to 'some interference effect', quantum measurement theory would be the best tool available to research such effects; [113, 36]
- The 'beam splitter' barrier model requires source linearity.
  This obviously holds true for dissipative and inelastic barrier potentials. Since tunneling for potentials in practice are mostly elastic scattering, the initial tunneling source would inevitably suffer deformations due to self-interference effect, affecting tunneling delay by producing dependences such as the initial source bandwidth [113].
- In context of graphene potential electron tunneling, dwell time is well-established for electron-spin precession in magnetic field. Factors mentioned to affect tunneling delay: [17, 82, 45]
  1. Interference diminished through oscillatory mode or Klein topological construction: tunneling delay increases linearly with barrier width;
  2. At normal incident angle tunneling delay is independent of barrier height, spin state and Fermi energy. In contrast, at oblique incident angles delay is influenced by spin state. Harman effect is exhibited in evanescent mode and at oblique angles but disappears at normal incident angles.

Time evolution under barrier potential

According to historical and comparative studies on this subject, there exists a twofold dilemma: [20, 84, 41, 113]

1. Progress made for minimizing observers effect, for instance the methods of weak measurements by measuring non-positional properties, such as spin or polarization. However, position-momentum uncertainty relation inevitably imputes an intrinsic precision limit.
2. Generalised time operator has not yet been found, time-energy uncertainty relation is used more reservedly.

From current controversies concerning the interpretations of tunneling mechanisms, 4 competing positions have arisen:[111, 113, 112];

- Temporary storage
- Interference and distortion;
- Effective time-dependent shutter which only selectively allows the frontal part of the tunneling source to be transmitted;
- Or effective beam splitter with linear relation between incident and transmitted source amplitudes.

Theories assuming barrier potential as disruptive medium have the common ground that re-emitted source can no longer be identified with original. This 'workaround' cleverly evades the thorny problem of inside barrier 'tunneling trajectories' by discrediting the existence of transit time; however it treats barrier potential as a black box and relies on extrapolated measurements. In contrast, the approach of complex path integrals are more compatible with external transversal time and relativistic operators (e.g. Klein Tunneling), however since 2013 to date no experimental continuations were proposed, perhaps because experimental impracticalities. [60, 45]

Consequently, the question whether complex tunneling time definitions are meaningful and their consistency with the well-established observables remains under current debate.

6.2.6 Final Remarks

My current view on this subject is:

- The properties of SNAP tunneling process can be identified as:
  - Having negligible non-linear tunneling effects;
  - Negligible tunneling dissipation (due to high Q-factor inner-surface);
  - Ideally elastic scattering.
- According to classic classification SNAP tunneling is a phenomenon for monochromatic continuous waves with WGM as its tunneling source while according to modern theory, it is considered as a pseudo-particle with orthogonal polarisations. The choice of barrier potential (SF) must exhibit sufficiently large cut-off frequency bandwidth to ensure single or multi-frequency source signal.
- The intended SNAP experiment should focus on answer the following questions:
  - Is Harman effect and superluminality a result of the mentioned interference effect?
  - Does SNAP tunneling have an associated external traversal time?
  - Could the modern theories, such as complex paths and operator theory be adapted to describe SNAP tunneling?
- Tunneling delay is a collective phenomenon influenced by both the source and barrier. However, there's currently a literature gap for isolating the degree of influence of the associative effects. In any case these known effects must be controlled carefully in experiments and it's important to distinguish an effect as source-induced or barrier-induced.
- SNAP platform addresses the main challenge in many tunneling time experiment, viz. measuring short tunneling delay by talking advantage of slow light that stems from WGM, for which the axial propagation speed is considerably slower than light-speed thus allowing more precision for measuring tunneling time.

Bibliography

[1] The optical radiation wavelength range - Gigahertz Optik.

[2] Jorge L. Agudín. Time Delay of Scattering Processes. *Physical Review*, 171(5):1385–1387, 7 1968. ISSN 0031-899X. doi: 10.1103/PhysRev.171.1385. URL https://link.aps.org/doi/10.1103/PhysRev.171.1385.

[3] A. Ashkin and J. M. Dziedzic. Observation of resonances in the radiation pressure on dielectric spheres. *Physical Review Letters*, 1977. ISSN 00319007. doi: 10.1103/PhysRevLett.38.1351.

[4] Toshihiko Baba. Slow light in photonic crystals, 2008. ISSN 17494885.

[5] Ph Balcou and L. Dutriaux. Dual Optical Tunneling Times in Frustrated Total Internal Reflection. *Physical Review Letters*, 1997. ISSN 10797114. doi: 10.1103/PhysRevLett.78.851.

[6] Fabien Bayle and Jean-Pierre Meunier. Efficient fabrication of fused-fiber biconical taper structures by a scanned CO2 laser beam technique. *Applied optics*, 2005. ISSN 0003-6935. doi: 10.1364/AO.44.006402.

[7] R. E. Benner, P. W. Barber, J. F. Owen, and R. K. Chang. Observation of structure resonances in the fluorescence spectra from microspheres. *Physical Review Letters*, 1980. ISSN 00319007. doi: 10.1103/PhysRevLett.44.475.

[8] A. E. Bernardini. Limitations on the principle of stationary phase when it is applied to tunneling analysis. *Physical Review A - Atomic, Molecular, and Optical Physics*, 2006. ISSN 10502947. doi: 10.1103/PhysRevA.74.062111.

[9] A. E. Bernardini. Stationary phase method and delay times for relativistic and non-relativistic tunneling particles. *Annals of Physics*, 2009. ISSN 00034916. doi: 10.1016/j.aop.2009.02.002.

[10] T.A. Birks, J.C. Knight, and T.E. Dimmick. High-resolution measurement of the fiber diameter variations using whispering gallery modes and no optical alignment. *IEEE Photonics Technology Letters*, 12(2):182–183, 2 2000. ISSN 1041-1135. doi: 10.1109/68.823510.

[11] Timothy A Birks and Youwei W Li. The Shape of Fiber Tapers. *Journal of Lightwave Technology*, 10(4):432–438, 1992. ISSN 15582213. doi: 10.1109/50.134196.

[12] Abhijit Biswas, Ilker S. Bayer, Alexandru S. Biris, Tao Wang, Enkeleda Dervishi, and Franz Faupel. Advances in top–down and bottom–up surface nanofabrication: Techniques, applications & future prospects. *Advances in Colloid and Interface Science*, 170(1-2):2–27, 1 2012. ISSN 0001-8686. doi: 10.1016/J.CIS.2011.11.001. URL https://www.sciencedirect.com/science/article/pii/S0001868611001904#s0010.

[13] C. V. Boys. On the production, properties, and some suggested uses of the finest threads. *Proceedings of the Physical Society of London*, 1887. ISSN 14787814. doi: 10.1088/1478-7814/9/1/303.

[14] Brandon Bozeat, Jonathan Stump, Advisor : Professor, and Yuxiang Liu. Microfurnace Design for Fabrication of Tapered Optical Fiber Conveyor Belts A Major Qualifying Project Report. Technical report, 2017.

[15] V. B. Braginsky, M. L. Gorodetsky, and V. S. Ilchenko. Quality-factor and nonlinear properties of optical whispering-gallery modes. *Physics Letters A*, 1989. ISSN 03759601. doi: 10.1016/0375-9601(89)90912-2.

[16] Gilberto Brambilla, Fei Xu, Peter Horak, Yongmin Jung, Fumihito Koizumi, Neil P. Sessions, Elena Koukharenko, Xian Feng, Ganapathy S. Murugan, James S. Wilkinson, and David J. Richardson. Optical fiber nanowires and microwires: fabrication and applications. *Advances in Optics and Photonics*, 1(1):107, 1 2009. ISSN 1943-8206. doi: 10.1364/AOP.1.000107. URL https://www.osapublishing.org/abstract.cfm?URI=aop-1-1-107.

[17] M. Büttiker. Larmor precession and the traversal time for tunneling. *Physical Review B*, 1983. ISSN 01631829. doi: 10.1103/PhysRevB.27.6178.

[18] Nicolas Camus, Enderalp Yakaboylu, Lutz Fechner, Michael Klaiber, Martin Laux, Yonghao Mi, Karen Z. Hatsagortsyan, Thomas Pfeifer, Christoph H. Keitel, and Robert Moshammer. Experimental Evidence for Quantum Tunneling Time. *Physical Review Letters*, 2017. ISSN 10797114. doi: 10.1103/PhysRevLett.119.023201.

[19] John J. Carey, Justyna Zawadzka, Dino A. Jaroszynski, and Klaas Wynne. Noncausal Time Response in Frustrated Total Internal Reflection? *Physical Review Letters*, 84(7):1431–1434, 2 2000. ISSN 0031-9007. doi: 10.1103/PhysRevLett.84.1431. URL http://www.ncbi.nlm.nih.gov/pubmed/11017535https://link.aps.org/doi/10.1103/PhysRevLett.84.1431.

[20] P. C. W. Davies. Quantum tunneling time. *Am. J. Phys.*, 2005. ISSN 00029505. doi: 10.1119/1.1810153.

[21] Timothy E. Dimmick, George Kakarantzas, Timothy A. Birks, and Philip St. J. Russell. Carbon dioxide laser fabrication of fused-fiber couplers and tapers. *Applied Optics*, 38(33):6845, 11 1999. ISSN 0003-6935. doi: 10.1364/AO.38.006845.

[22] Heather. Dyke and Adrian. Bardon. *A companion to the philosophy of time*. J. Wiley, 2013. ISBN 1118522052. URL https://books.google.co.uk/books/about/A_Companion_to_the_Philosophy_of_Time.html?id=H1AiUQ4EKJYC&redir_esc=y.

[23] a. Enders and G. Nimtz. On superluminal barrier traversal. *Journal de Physique I*, 1992. ISSN 1155-4304. doi: 10.1051/jp1:1992236.

[24] A. Enders and G. Nimtz. Evanescent-mode propagation and quantum tunneling. *Physical Review E*, 1993. ISSN 1063651X. doi: 10.1103/PhysRevE.48.632.

[25] A. Enders and G. Nimtz. Zero-time tunneling of evanescent mode packets. *Journal de Physique I*, 1993. ISSN 1155-4304. doi: 10.1051/jp1:1993257.

[26] Daniel A. Fleisch and Laura Kinnaman. *A student's guide to waves*. ISBN 1107054869.

[27] Liting Gai, Jin Li, and Yong Zhao. Preparation and application of microfiber resonant ring sensors: A review. *Optics & Laser Technology*, 89:126–136, 3 2017. ISSN 0030-3992. doi: 10.1016/J.OPTLASTEC.2016.10.002.

[28] C. G.B. Garrett, W. Kaiser, and W. L. Bond. Stimulated emission into optical whispering modes of spheres. *Physical Review*, 1961. ISSN 0031899X. doi: 10.1103/PhysRev.124.1807.

[29] Ginu Rajan. *Optical Fiber Sensors, Advanced Techniques and Applications*. 2015. ISBN 9781482228298.

[30] N. Goldberg and S. R. Pollack. Oscillatory tunneling current through thin-film insulating barriers in a magnetic field. *Journal of Applied Physics*, 1963. ISSN 00218979. doi: 10.1063/1.1729257.

[31] Matjaž Gomilšek. Whispering gallery modes. Technical report, 2011.

[32] David J. (David Jeffery) Griffiths. *Introduction to quantum mechanics*. ISBN 1107179866.

[33] Ph Grossel. The phase delay and its complex time: From stationary states up to wave packets. *Annals of Physics*, 2013. ISSN 00034916. doi: 10.1016/j.aop.2012.11.006.

[34] Alain Haché and Louis Poirier. Long-range superluminal pulse propagation in a coaxial photonic crystal. *Applied Physics Letters*, 2002. ISSN 00036951. doi: 10.1063/1.1432760.

[35] T. Hamidfar, A. Dmitriev, B. Magdan, P. Bianucci, and M. Sumetsky. Surface nanoscale axial photonics at a capillary fiber. *Optics Letters*, 42(16):3060, 8 2017. ISSN 0146-9592. doi: 10.1364/OL.42.003060.

[36] E. H. Hauge and J. A. Støvneng. Tunneling times: a critical review. *Reviews of Modern Physics*, 61(4):917–936, 10 1989. ISSN 0034-6861. doi: 10.1103/RevModPhys.61.917.

[37] Tin-Lun Ho. Oscillatory tunneling between quantum Hall systems. *Phys. Rev. B*, 1994. ISSN 0163-1829. doi: 10.1103/PhysRevB.50.4524.

[38] K Y Huang, K Y Hsu, D Y Jheng, W J Zhuo, P Y Chen, P S Yeh, and S L Huang. Low-loss propagation in Crˆ4+:YAG double-clad crystal fiber fabricated by sapphire tube assisted CDLHPG technique. *Optics Express*, 16(16):12264, 8 2008. ISSN 1094-4087. doi: 10.1364/OE.16.012264.

[39] N.G. Kelkar, D. Lozano Gómez, and Edgar J. Patiño. Time in dissipative tunneling: Subtleties and applications. *Annals of Physics*, 382:11–21, 7 2017. ISSN 0003-4916. doi: 10.1016/J.AOP.2017.04.010. URL https://www.sciencedirect.com/science/article/pii/S0003491617301227.

[40] S. Lj S Kočinac and V. Milanović. Tunneling times in complex potentials. *Physics Letters, Section A: General, Atomic and Solid State Physics*, 2008. ISSN 03759601. doi: 10.1016/j.physleta.2007.07.021.

[41] Ossama Kullie. Tunneling time in attosecond experiments, intrinsic-type of time. Keldysh, and Mandelstam-Tamm time. *Journal of Physics B: Atomic, Molecular and Optical Physics*, 2016. ISSN 13616455. doi: 10.1088/0953-4075/49/9/095601.

[42] R. Landauer and Th Martin. Barrier interaction time in tunneling. *Reviews of Modern Physics*, 1994. ISSN 00346861. doi: 10.1103/RevModPhys.66.217.

[43] Alexandra S. Landsman, Matthias Weger, Jochen Maurer, Robert Boge, André Ludwig, Sebastian Heuser, Claudio Cirelli, Lukas Gallmann, and Ursula Keller. Ultrafast resolution of tunneling delay time. *Optica*, 2014. ISSN 2334-2536. doi: 10.1364/OPTICA.1.000343.

[44] Ming Li, Fufei Pang, Hairun Guo, Yunqi Liu, Na Chen, Zhenyi Chen, and Tingyun Wang. Tapered optical fiber fabricated by high-frequency pulsed carbon dioxide laser. volume 7853, page 78533E. International Society for Optics and Photonics, 11 2010. doi: 10.1117/12.870619.

[45] Zhi Jian Li, Haiyan Zhao, Yi Hang Nie, and J. Q. Liang. Barrier tunneling time of an electron in graphene. *Journal of Applied Physics*, 2013. ISSN 00218979. doi: 10.1063/1.4789636.

[46] S Longhi, M Marano, P Laporta, and M Belmonte. Superluminal optical pulse propagation at 1.5 microm in periodic fiber Bragg gratings. *Phys Rev E Stat Nonlin Soft Matter Phys*, 2001. ISSN 1063-651X. doi: 10.1103/PhysRevE.64.055602.

[47] V F Los and M V Los. An exact solution of the time-dependent schrödinger equation with a rectangular potential for real and imaginary times. *Ukrainian Journal of Physics*, 2016. ISSN 20710194. doi: 10.15407/ujpe61.04.0331.

[48] J. T. Lunardi, L. A. Manzoni, A. T. Nystrom, and B. M. Perreault. Average transmission times for the tunneling of wave packets. *Journal of Russian Laser Research*, 2011. ISSN 10712836. doi: 10.1007/s10946-011-9232-0.

[49] José T. Lunardi, Luiz A. Manzoni, and Andrew T. Nystrom. Salecker-Wigner-Peres clock and average tunneling times. *Physics Letters, Section A: General, Atomic and Solid State Physics*, 2011. ISSN 03759601. doi: 10.1016/j.physleta.2010.11.055.

[50] Amos Martinez, Mohammed Al Araimi, Artemiy Dmitriev, Petro Lutsyk, Shen Li, Chengbo Mou, Alexey Rozhin, Misha Sumetsky, and Sergei Turitsyn. Low-loss saturable absorbers based on tapered fibers embedded in carbon nanotube/polymer composites. *APL Photonics*, 2(12):126103, 2017. doi: 10.1063/1.4996918.

[51] M.J. Matthewson, C.R. Kurkjian, and J.R. Hamblin. Acid stripping of fused silica optical fibers without strength degradation. *Journal of Lightwave Technology*, 15(3):490–497, 3 1997. ISSN 07338724. doi: 10.1109/50.557565.

[52] C McAtamney, A Cronin, R Sherlock, G M O'Connor, and T J Glynn. Reproducible Method for Fabricating Fused Biconical Tapered Couplers Using a CO2 Laser Based Process. *Proceedings of the Third International WLT-Conference on Lasers in Manufacturing 2005, Munich, June 2005.*, 2005.

[53] S. L. McCall, A. F J Levi, R. E. Slusher, S. J. Pearton, and R. A. Logan. Whispering-gallery mode microdisk lasers. *Applied Physics Letters*, 1992. ISSN 00036951. doi: 10.1063/1.106688.

[54] C. R. McDonald, G. Orlando, G. Vampa, and T. Brabec. Tunneling time, what is its meaning? In *Journal of Physics: Conference Series*, 2015. doi: 10.1088/1742-6596/594/1/012019.

[55] Gustav Mie. Beiträge zur Optik trüber Medien, speziell kolloidaler Metallösungen. *Annalen der Physik*, 330(3):377–445, 1 1908. ISSN 00033804. doi: 10.1002/andp.19083300302. URL http://doi.wiley.com/10.1002/andp.19083300302.

[56] W. Luis Mochán and Vera L. Brudny. Comment on "noncausal time response in frustrated total internal reflection?". *Physical Review Letters*, 2001. ISSN 10797114. doi: 10.1103/PhysRevLett.87.119101.

[57] M. Mojahedi, K. J. Malloy, G. V. Eleftheriades, J. Woodley, and R. Y. Chiao. Abnormal wave propagation in passive media. *IEEE Journal on Selected Topics in Quantum Electronics*, 2003. ISSN 1077260X. doi: 10.1109/JSTQE.2002.807971.

[58] Mohammad Mojahedi, Edl Schamiloglu, Kamil Agi, and Kevin J. Malloy. Frequency-domain detection of superluminal group velocity in a distributed Bragg reflector. *IEEE Journal of Quantum Electronics*, 2000. ISSN 00189197. doi: 10.1109/3.831016.

[59] Mohammad Mojahedi, Edl Schamiloglu, Frank Hegeler, and Kevin J. Malloy. Time-domain detection of superluminal group velocity for single microwave pulses. *Physical Review E - Statistical Physics, Plasmas, Fluids, and Related Interdisciplinary Topics*, 2000. ISSN 1063651X. doi: 10.1103/PhysRevE.62.5758.

[60] J. G. Muga, R. Sala Mayato, and I. L. Egusquiza. *Time in quantum mechanics*. Springer-Verlag, 2008. ISBN 3540734724.

[61] K Mullaney. *The fabrication of micro-tapered optical fibres for sensing applications Optical fibre sensors View project Improved solar cell coverglasses and thermal control mirrors View project*. PhD thesis, Cranfield University, 2016.

[62] Masaya Notomi. Manipulating light with strongly modulated photonic crystals. *Reports on Progress in Physics*, 2010. ISSN 00344885. doi: 10.1088/0034-4885/73/9/096501.

[63] Masaya Notomi, Eiichi Kuramochi, and Takasumi Tanabe. Large-scale arrays of ultrahigh-Q coupled nanocavities. *Nature Photonics*, 2008. ISSN 17494885. doi: 10.1038/nphoton.2008.226.

[64] R C Oehrle. Galvanometer beam-scanning system for laser fiber drawing. *Applied optics*, 1979. ISSN 0003-6935. doi: 10.1364/AO.18.000496.

[65] S. T. Oh, W. T. Han, U. C. Paek, and Y. Chung. Azimuthally symmetric long-period fiber gratings fabricated with CO2 laser. *Microwave and Optical Technology Letters*, 41(3):188–190, 5 2004. ISSN 0895-2477. doi: 10.1002/mop.20088. URL http://doi.wiley.com/10.1002/mop.20088.

[66] U. C. Paek. Laser Drawing of Optical Fibers. *Applied Optics*, 13(6):1383, 6 1974. ISSN 0003-6935. doi: 10.1364/AO.13.001383.

[67] Parama Pal and Wayne H Knox. Low loss fusion splicing of micron scale silica fibers. *Optics Express*, 16(15):11568, 7 2008. ISSN 1094-4087. doi: 10.1364/OE.16.011568.

[68] D J Papoular, P Cladé, S V Polyakov, C F McCormick, a L Migdall, and P D Lett. Measuring optical tunneling times using a Hong-Ou-Mandel interferometer. *Optics express*, 2008. ISSN 1094-4087. doi: 10.1364/OE.16.016005.

[69] A. Paul, A. Saha, S. Bandopadhyay, and B. Dutta-Roy. Tunneling times through a barrier with inelasticity. *European Physical Journal D*, 2007. ISSN 14346060. doi: 10.1140/epjd/e2007-00050-8.

[70] J. Milton Pereira, P. Vasilopoulos, and F. M. Peeters. Graphene-based resonant-tunneling structures. *Applied Physics Letters*, 2007. ISSN 00036951. doi: 10.1063/1.2717092.

[71] Boundless Physics. Radio Waves, 2017.

[72] Zenan Qi, D. A. Bahamon, Vitor M. Pereira, Harold S. Park, D. K. Campbell, and A. H Castro Neto. Resonant tunneling in graphene pseudomagnetic quantum dots. *Nano Letters*, 2013. ISSN 15306984. doi: 10.1021/nl400872q.

[73] Shi-Xiong Qian, Judith B. Snow, Huey-Ming Tzeng, and Richard K. Chang. Lasing Droplets: Highlighting the Liquid-Air Interface by Laser Emission. URL https://www.jstor.org/stable/pdf/1696712.pdf.

[74] A. Ranfagni, D. Mugnai, P. Fabeni, and G. P. Pazzi. Delay-time measurements in narrowed waveguides as a test of tunneling. *Applied Physics Letters*, 1991. ISSN 00036951. doi: 10.1063/1.104544.

[75] A. Ranfagni, D. Mugnai, P. Fabeni, G.P. Pazzi, G. Naletto, and C. Sozzi. Optical-tunneling time measures: a microwave model. *Physica B: Condensed Matter*, 175(1-3):283–286, 12 1991. ISSN 0921-4526. doi: 10.1016/0921-4526(91)90727-V. URL https://www.sciencedirect.com/science/article/pii/092145269190727V.

[76] Lord Rayleigh. The problem of the whispering gallery. *Philosophical Magazine Series 6*, 1910. ISSN 1941-5982. doi: 10.1080/14786441008636993.

[77] M. T. Reiten, D. Grischkowsky, and R. A. Cheville. Optical tunneling of single-cycle terahertz bandwidth pulses. *Physical Review E - Statistical Physics, Plasmas, Fluids, and Related Interdisciplinary Topics*, 2001. ISSN 1063651X. doi: 10.1103/PhysRevE.64.036604.

[78] M T Reiten, K McClatchey, D Grischkowsky, and R a Cheville. Incidence-angle selection and spatial reshaping of terahertz pulses in optical tunneling. *Optics Letters*, 2001. ISSN 0146-9592. doi: 10.1364/OL.26.001900.

[79] R. D. Richtmyer. Dielectric resonators. *Journal of Applied Physics*, 1939. ISSN 00218979. doi: 10.1063/1.1707320.

[80] G C Righini, Y Dumeige, P Feron, M Ferrari, G N Conti, D Ristic, and S Soria. Whispering gallery mode microresonators: Fundamentals and applications. *Rivista Del Nuovo Cimento*, 2011. ISSN 0393697X. doi: 10.1393/ncr/i2011-10067-2.

[81] W. M. Robertson, J. Ash, and J. M. McGaugh. Breaking the sound barrier: Tunneling of acoustic waves through the forbidden transmission region of a one-dimensional acoustic band gap array. *American Journal of Physics*, 2002. ISSN 0002-9505. doi: 10.1119/1.1477430.

[82] Farhad Sattari and Edris Faizabadi. Tunneling time and Hartman effect in a ferromagnetic graphene superlattice. *AIP Advances*, 2012. ISSN 21583226. doi: 10.1063/1.3681190.

[83] Silvio Savoia, Giuseppe Castaldi, Vincenzo Galdi, Andrea Alù, and Nader Engheta. Tunneling of obliquely incident waves through PT -symmetric epsilon-near-zero bilayers. *Physical Review B - Condensed Matter and Materials Physics*, 2014. ISSN 10980121. doi: 10.1103/PhysRevB.89.085105.

[84] D. Sokolovski and E. Akhmatskaya. 'Superluminal paradox' in wave packet propagation and its quantum mechanical resolution. *Annals of Physics*, 2013. ISSN 00034916. doi: 10.1016/j.aop.2013.09.003.

[85] C Spielmann, R Szipöcs, a Stingl, and F Krausz. Tunneling of optical pulses through photonic band gaps. *Physical review letters*, 1994. ISSN 1079-7114. doi: 10.1103/PhysRevLett.73.2308.

[86] A. M. Steinberg, P. G. Kwiat, and R. Y. Chiao. Measurement of the single-photon tunneling time. *Physical Review Letters*, 1993. ISSN 00319007. doi: 10.1103/PhysRevLett.71.708.

[87] M. Sumetsky. Mode localization and the Q-factor of a cylindrical microresonator. *Optics Letters*, 2010. ISSN 0146-9592. doi: 10.1364/OL.35.002385.

[88] M. Sumetsky. Localization of light in an optical fiber with nanoscale radius variation. In *2011 Conference on Lasers and Electro-Optics Europe and 12th European Quantum Electronics Conference, CLEO EUROPE/EQEC 2011*, 2011. ISBN 9781457705335. doi: 10.1109/CLEOE.2011.5943708.

[89] M. Sumetsky. Theory of SNAP devices: basic equations and comparison with the experiment. *Optics Express*, 20(20):22537, 9 2012. ISSN 1094-4087. doi: 10.1364/OE.20.022537.

[90] M Sumetsky. Nanophotonics of optical fibers. *Nanophotonics*, 2(5-6):393–406, 1 2013. ISSN 2192-8614. doi: 10.1515/nanoph-2013-0041.

[91] M. Sumetsky. Delay of light in an optical bottle resonator with nanoscale radius variation: Dispersionless, broadband, and low loss. *Physical Review Letters*, 2013. ISSN 00319007. doi: 10.1103/PhysRevLett.111.163901.

[92] M. Sumetsky. Nanophotonics of optical fibres. In *2014 Third Mediterranean Photonics Conference*, pages 1–3. IEEE, 5 2014. ISBN 978-1-4799-4818-5. doi: 10.1109/MePhoCo.2014.6866482.

[93] M. Sumetsky and Y. Dulashko. SNAP: Fabrication of long coupled microresonator chains with sub-angstrom precision. *Optics Express*, 20(25):27896, 12 2012. ISSN 1094-4087. doi: 10.1364/OE.20.027896.

[94] M. Sumetsky and J. M. Fini. Surface nanoscale axial photonics. *Optics Express*, 19(27):26470, 12 2011. ISSN 1094-4087. doi: 10.1364/OE.19.026470.

[95] M Sumetsky, Y Dulashko, and A Hale. Fabrication and study of bent and coiled free silica nanowires: Self-coupling microloop optical interferometer. *Optics Express*, 2004. ISSN 1094-4087. doi: 10.1364/OPEX.12.003521.

[96] M. Sumetsky, D. J. DiGiovanni, Y. Dulashko, J. M. Fini, X. Liu, E. M. Monberg, and T. F. Taunay. Surface nanoscale axial photonics: robust fabrication of high-quality-factor microresonators. *Optics Letters*, 36(24):4824, 12 2011. ISSN 0146-9592. doi: 10.1364/OL.36.004824.

[97] M. Sumetsky, K. Abedin, D. J. DiGiovanni, Y. Dulashko, J. M. Fini, and E. Monberg. Coupled high Q-factor surface nanoscale axial photonics (SNAP) microresonators. *Optics Letters*, 37(6): 990, 3 2012. ISSN 0146-9592. doi: 10.1364/OL.37.000990.

[98] Misha Sumetsky, D. J. DiGiovanni, Y. Dulashko, X. Liu, E. M. Monberg, and T. F. Taunay. Photo-induced SNAP: fabrication, trimming, and tuning of microresonator chains. *Optics Express*, 2012. ISSN 1094-4087. doi: 10.1364/OE.20.010684.

[99] Naoya Takizawa, Lunlun Xian, Peng Wang, and Hongpu Li. Helical Long-Period Fiber Grating Formed in a Optical Micro/Nano Wire by Using a CO2 Laser. In *2014 IEEE Photonics Society Summer Topical Meeting Series*, pages 202–203. IEEE, 7 2014. ISBN 978-1-4799-2767-8. doi: 10.1109/SUM.2014.110.

[100] Limin Tong and Michael Sumetsky. Fabrication of MNFs. In *Subwavelength and Nanometer Diameter Optical Fibers*, chapter 3, pages 73–97. Springer Science & Business Media, 2010. doi: 10.1007/978-3-642-03362-9{_}3.

[101] N. A. Toropov and M. Sumetsky. Permanent matching of coupled optical bottle resonators with better than 016 GHz precision. *Optics Letters*, 41(10):2278, 5 2016. ISSN 0146-9592. doi: 10.1364/OL.41.002278.

[102] Dashiell L. P. Vitullo, Sajid Zaki, Gabriella Gardosi, Brian J. Mangan, Robert S. Windeler, Michael Brodsky, and Misha Sumetsky. Differential Tuning of Coupled SNAP Microresonators on a Capillary Surface. In *Conference on Lasers and Electro-Optics*, page SW4A.6, Washington, D.C., 5 2018. OSA. ISBN 978-1-943580-42-2. doi: 10.1364/CLEO{_}SI.2018.SW4A.6.

[103] Yurii Vlasov, William M J Green, and Fengnian Xia. High-throughput silicon nanophotonic wavelength-insensitive switch for on-chip optical networks. *Nature Photonics*, 2008. ISSN 17494885. doi: 10.1038/nphoton.2008.31.

[104] Jonathan M Ward, Danny G O'Shea, Brian J Shortt, Michael J Morrissey, Kieran Deasy, and Síle G.Nic Chormaic. Heat-and-pull rig for fiber taper fabrication. *Review of Scientific Instruments*, 2006. ISSN 00346748. doi: 10.1063/1.2239033.

[105] Torsten Wieduwilt, Konstantin Kirsch, Jan Dellith, Reinhardt Willsch, and Hartmut Bartelt. Optical Fiber Micro-Taper with Circular Symmetric Gold Coating for Sensor Applications Based on Surface Plasmon Resonance. *Plasmonics*, 2013. ISSN 15571955. doi: 10.1007/s11468-012-9432-7.

[106] Wikipedia contributors. Measurement Problem, 2018.

[107] Wikipedia contributors. Microwave, 2018.

[108] Wikipedia contributors. Quantum tunnelling, 2018.

[109] Wikipedia contributors. Sound, 2018.

[110] Wikipedia contributors. Terahertz Radiation, 2018.

[111] Herbert Winful. Energy storage in superluminal barrier tunneling: Origin of the Hartman effect. *Optics Express*, 2002. ISSN 1094-4087. doi: 10.1364/OE.10.001491.

[112] Herbert G. Winful. Nature of "Superluminal" Barrier Tunneling. *Physical Review Letters*, 2003. ISSN 10797114. doi: 10.1103/PhysRevLett.90.023901.

[113] Herbert G. Winful. Tunneling time, the Hartman effect, and superluminality: A proposed resolution of an old paradox, 2006. ISSN 03701573.

[114] Fengnian Xia, Lidija Sekaric, and Yurii Vlasov. Ultracompact optical buffers on a silicon chip. *Nature Photonics*, 2007. ISSN 17494885. doi: 10.1038/nphoton.2006.42.

[115] Fei Xu. *Optical Fibre Nanowire Devices*. PhD thesis, University of Southampton, 2008.

[116] Suxia Yang, J. H. Page, Zhengyou Liu, M. L. Cowan, C. T. Chan, and Ping Sheng. Ultrasound Tunneling through 3D Phononic Crystals. *Physical Review Letters*, 2002. ISSN 10797114. doi: 10.1103/PhysRevLett.88.104301.

[117] Hirohisa Yokota, Eiichi Sugai, and Yutaka Sasaki. Optical irradiation method for fiber coupler fabrications. *Optical Review*, 4(1):A104–A107, 1 1997. ISSN 1340-6000. doi: 10.1007/BF02936004.

[118] Xiu Rong Zhang and Wei Dong Li. Nonlinear tunneling through a strong rectangular barrier. *Chinese Physics B*, 2015. ISSN 20583834. doi: 10.1088/1674-1056/24/7/070311.

Appendix

The Matlab Script for plotting IL from 2 input/output SNAPs:

```
%%Import the S12 measurement data and plot on OVA 5000
%% Yong Yang. 23/08/2018
clear
close all

%% global settings and descriptions
delimiter='\t';
headerlinesIn = 8;% The data line start from
z_step=1;  %% one step is one lum in our case
DataPath='D:\Exp_UniformSF\New S12 Scan 1';
%% Where the data folder is Del=1;
%% delete the two maxima at the beginner
and ending of the scanning

global X Lambda;
Lambda=1e-8; %% a penalty factor for finding
the constrained optimization value


if ~isdir(DataPath)
  errorMessage = sprintf ('Error: The following folder
  does not exist:\n%s', myFolder);
  uiwait(warndlg(errorMessage));
  return;
end
FilePattern=fullfile(DataPath,'a*.txt');
files_z_step=dir(FilePattern);
z=linspace(1,z_step*length(files_z_step));

%%% A big for loop for different z positions.
for step_z=1:length(files_z_step)
File_name=fullfile(DataPath,files_z_step(step_z).name);
Data_struct=importdata(File_name,delimiter,headerlinesIn);
Data_z=Data_struct.data;
[rownum,colnum]=size(Data_z);
Data_z=Data_z(1+Del:rownum-Del,:);
wavelength=Data_z(:,1);
J_z(:,step_z,1,1)=Data_z(:,3).*exp(1i*Data_z(:,7));
```

```
% complex of Jones Matrix
J_z(:,step_z,1,2)=Data_z(:,4).*exp(1i*Data_z(:,8));
J_z(:,step_z,2,1)=Data_z(:,5).*exp(1i*Data_z(:,9));
J_z(:,step_z,2,2)=Data_z(:,6).*exp(1i*Data_z(:,10));
% InsersionLoss(:,step_z)=sgolayfilt(NormalizeData
((abs(J_z(:,step_z,1,1)).^2+abs(J_z(:,step_z,1,2))
.^2+abs(J_z(:,step_z,2,1)).^2+abs(J_z(:,step_z,2,2)).^2)/2),5,101);
InsersionLoss(:,step_z)=(abs(J_z(:,step_z,1,1)).
^2+abs(J_z(:,step_z,1,2)).^2+abs(J_z(:,step_z,2,1))
.^2+abs(J_z(:,step_z,2,2)).^2)/2;

end



%% Plot the Insersion Loss
% figure(1)
% plot(wavelength,InsersionLoss(13,:));
% figure(2)
%subplot(2,2,1)
imagesc(z,wavelength,InsersionLoss);
axis xy
colormap jet;
c=colorbar;
% c.Label.String='Insertion Loss [A.U.]';
% c.Label.FontSize=10;
xlabel('Distance($\mu m$)','Interpreter','Latex')
ylabel('Wavelength(nm)')
set(gca,'fontsize',16)
title({'S12 Measurement'})

% figure (5)
% plot(wavelength,InsersionLoss(:,25),wavelength,
InsersionLossTM(:,25),wavelength,InsersionLossTE(:,25));
```